Università degli Studi di Cagliari

DOTTORATO DI RICERCA

in Ingegneria Elettronica e Informatica

Ciclo XXVII

TITOLO TESI

DESIGN OF MICROWAVE SUBSYSTEMS FOR RADIO ASTRONOMICAL RECEIVERS

Settore/i scientifico disciplinari di afferenza

ING-INF/02 Campi Elettromagnetici

Presentata da: Ladu Adelaide

Coordinatore Dottorato Prof. Fabio Roli

Tutor Prof. Giuseppe Mazzarella

Esame finale anno accademico 2014 – 2015

To my husband Riccardo,
my parents Daniele e Antonietta
and my family Francesco, Gianna e Cristina

Acknowledgments

I do my apologies about the Italian language used in this section but I prefer writing my acknowledgements in my mother tongue.

Questa tesi riassume un lavoro di ricerca durato quattro anni, che ancora non si è concluso e che spero si concluderà presto con la realizzazione di ciò che ho progettato. Durante questo periodo ho conosciuto persone straordinarie senza le quali non sarebbe stato possibile portare a termine l'obiettivo che mi ero prefissata.

Il mio primo ringraziamento va a mia madre senza la quale non avrei mai intrapreso questo cammino. Il suo incoraggiamento mi ha accompagnato in tutta mia vita universitaria e non solo spingendomi a dare sempre il massimo. Un grosso grazie va a tutta la mia famiglia, babbo e mamma, Francesco, Gianna e Cristina presenti sempre e comunque, che mi hanno sostenuto e appoggiato in qualunque decisione prendessi.

Un sentito ringraziamento va al mio tutor, nonché relatore di tesi, il prof. Giuseppe Mazzarella, colui che mi ha fatto conoscere quanto sia stimolante il mondo delle microonde soprattutto se applicato all'esigente mondo della radioastronomia.

Un ringraziamento va all'Osservatorio Astronomico di Cagliari che mi ha supportato finanziariamente e soprattutto a tutto lo staff del gruppo ricevitori senza la quale non sarebbe stato possibile portare avanti il lavoro. In particolare, un ringraziamento va a dott. Tonino Pisanu che ha creduto in me dopo il mio rientro dall'Inghilterra, a Giuseppe sempre al mio fianco a darmi consigli e suggerimenti durante il periodo delle innumerevoli simulazioni, nonché a stimolarmi con idee e progetti ambiziosi e qualche volta quasi impossibili.

Inoltre, un ringraziamento va ad Andrea per i tanti caffè e per le lunghe chiacchierate su…*chi ce l'ha fatto fare*….

Un ringraziamento va anche alla Regione Sardegna che finanziando il nostro progetto con i fondi della Legge Regionale 7 ha permesso a un gruppo di dieci giovani ricercatori precari di portare avanti un'idea ambiziosa sia a livello scientifico che a livello tecnologico.

Infine, ma non per ultimo, ringrazio mio marito Riccardo per essere sempre al mio fianco.

Abstract

The radio astronomical receivers are devices that they measure the radio emissions coming from celestial sources. Therefore, the aim of these devices is to convert the weak electromagnetic energy from space into a measurable electrical signal. The nature of the signal emitted by celestial sources imposes that such receivers must be broadband, very sensitive and designed to measure noise. In fact, the electromagnetic signal that the receivers must capture and measure, in addition to being very weak, is a random signal with components uncorrelated with each other, with different frequencies and with zero mean value (i.e. it is like the thermal noise produced by a resistor subject to a temperature). Therefore, the weakness and the peculiarity of these signals make the radio astronomy receivers other than those used in the telecommunications.

It is in this context that the work of my PhD thesis has been developed. Three different projects, that regard to the microwave subsystems of the radio astronomical receiver, have been treated.

The first project is focus on the development of a new configuration of broadband polarizer with very flat phase response in microtrip technology.

The second project is a feasibility study on the optics of a 3mm SIS receiver in order to install it in the Gregorian focus of the Sardinia Radio Telescope.

The third project is fully dedicated on the development of a high performance wideband feed-horn for a state-of-the-art multi-beam S-band (2.3 - 4.3 GHz) receiver to install in the primary focus of the Sardinia Radio Telescope

Contents

Introduction

The radio astronomical receivers are devices that they measure the radio emissions coming from celestial sources. Therefore, the aim of these devices is to convert the weak electromagnetic energy from space into a measurable electrical signal. The nature of the signal emitted by celestial sources imposes that such receivers must be broadband, very sensitive and designed to measure noise. In fact, the electromagnetic signal that the receivers must capture and measure, in addition to being very weak, is a random signal with components uncorrelated with each other, with different frequencies and with zero mean value (i.e. it is like the thermal noise produced by a resistor subject to a temperature). Therefore, the weakness and the peculiarity of these signals make the radio astronomy receivers other than those used in the telecommunications.

The radio astronomical receiver is like super-heterodyne receiver and it can be divide in three blocks: a feed-horn antenna, a front-end and a mixer. The feed-horn antenna is positioned on the focus of the radio telescope. It is used to adapt the antenna beam and to collect the energy that is accumulated by the mirror of the radio telescope and concentrated on its focus. The dewar is a container, usually cylindrical, and it contains all those devices that are involved in the amplification of the signal (Low Noise Amplifiers, bandpass filters), in the separation of the two linear polarizations (Ortho Mode Transducers) or circular polarizations (polarizers) and in the calibration (directional couplers, power dividers). All devices compose the front-end and work at cryogenic temperatures (20°K -70°K). The very low temperatures allow us to minimize the noise produced mainly by the amplifier. This device is fundamental to amplify the weak signal. In addition, since the signal coming from the sky is unknown, it is need to calibrate the receiver injecting a signal of known power (noise generator) by using the directional couplers. The mixer allows shifting the frequency of the received signal to a lower frequency, said intermediate frequency. This is necessary because often the useful signals are at a frequency too high. With the mixer, there are also the band-pass filters, the low noise amplifiers and the insulators. These devices work at room temperature (300 ° K).

It is in this context that the work of my PhD thesis has been developed. Three different projects, that regard to the microwave subsystems of the radio astronomical receiver, have been treated.

In the first chapter, a brief description of the radio astronomy, the radio telescopes, and in particular of the Sardinia Radio Telescope, and the radio astronomical receivers is given.

The second chapter is dedicated to describe the first of three project: the development of a new broadband polarizer with very flat phase response in microstrip technology. In collaboration with the University of Manchester, School of Physics and Astronomy, I studied, manufactured and tested a new broadband microstrip quadrature hybrid with very flat phase response. The novel design is based on the transposition in microstrip technology of a combination of waveguide components used to build particular broadband polarizers.

The third chapter is focus on the study of the optics of a 3mm SIS receiver to install in the Gregorian focus of the Sardinia Radio Telescope (SRT). The receiver, made by IRAM (Institute de Radio Astronomie Millimétrique) for the Plateau de Bure interferometer (PdBI), has been purchased from the Astronomical Observatory of Cagliari to test the performance of the SRT at the millimeter frequencies (84 – 116 GHz). Since the IRAM receiver was originally designed for the PdBI antenna, a new optical and mechanical configuration had to be studied to adapt the instruments to the SRT optics and to its cabin mechanical structure.

The four chapter is fully dedicated to the development of a new high performance wideband feed-horn for a new multi-beam S-band (2.3 - 4.3 GHz) receiver to install in the primary focus of the Sardinia Radio Telescope. The novel design is based on quad-ridged, properly modified and optimized, put inside in a circular waveguide. The new configuration of the feed takes into account of all requirements to work in multibeam receiver. The feasibility study of the multibeam receiver with three, five and seven feed with the particular attention to the study of the phenomena of coupling between the feeds has been made. Unexpected presence of pulsed emissions very strong coming from radar systems, we obligated to change the specifications of the feed design. A new S-band feed has been designed with a frequency range of only 40% percent bandwidth (3-4.5 GHz). The new configuration of a quad-ridge horn antenna shows performances in accordance with the project specification.

Chapter 1: Radio telescopes

1.1.Radio astronomy [1]

Radio astronomy is a branch of astronomy that studies celestial sources at the radio wavelengths contrary to optical astronomy that studies celestial sources at the visible frequencies. Radio astronomy originated in 1932 when Karl Jansky discovered the radio emission from the Milky Way. Karl Jansky worked as engineer with Bell Telephone Laboratories and, in the 1932, was given a charge to study the origin of atmospheric interferences that interfered with transatlantic voice transmissions. Therefore, he built a large directional antenna to detect these interferences. Although most of these could be attributed to thunderstorms, aircraft, or power lines, Jansky also noticed the presence of a weak background signal that seemed to come from outer space. The receiver system, composed by a square loop antennas array and a receiver at 20.5 MHz with a bandwidth of 1 KHz (Fig. 1.1), had a good sensibility and a good stability. Besides, this receiver system could be rotated in azimuth to determine with certainty the direction of the interferences.

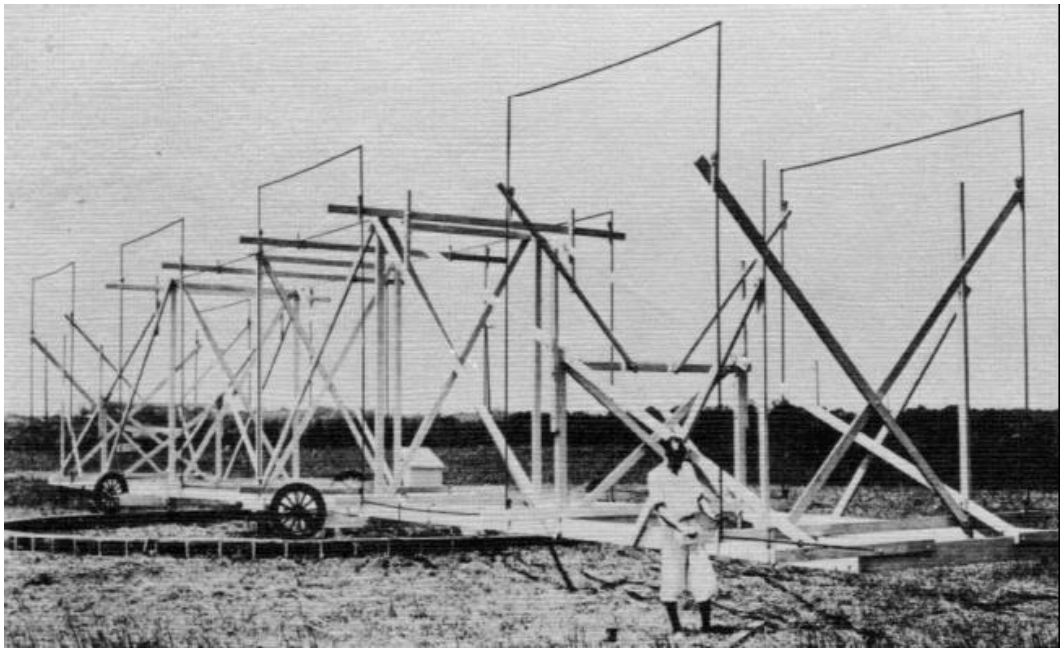

Fig.1.1: Jansky's antenna that first detected extra-terrestrial RF radiation.

These characteristics of the receiving system allowed him to isolate the cosmic radiation. Since the signal peaked about every 24 hours, Jansky originally suspected the source of the interference was the Sun crossing the view of his directional antenna. However, by comparing his observations with optical

astronomical maps, Jansky concluded that the radiation source peaked when his antenna was aimed at the densest part of the Milky Way, in the constellation of Sagittarius. Furthermore, he stated that the strange radio interference may be generated by interstellar gas and dust in the galaxy.

The accidental discovery of Jansky, who began the radio astronomy, was not taken into account at first. Only in 1937, a radio amateur, Grote Reber, decided to continue observations of Karl Jansky. He built, in his backyard, the first prototype of the modern radio telescope (Fig. 1.2). It was a parabolic radio telescope of 9.5 m in diameter, built on a solid wood frame, with a receiver at 160 MHz with a good sensibility.

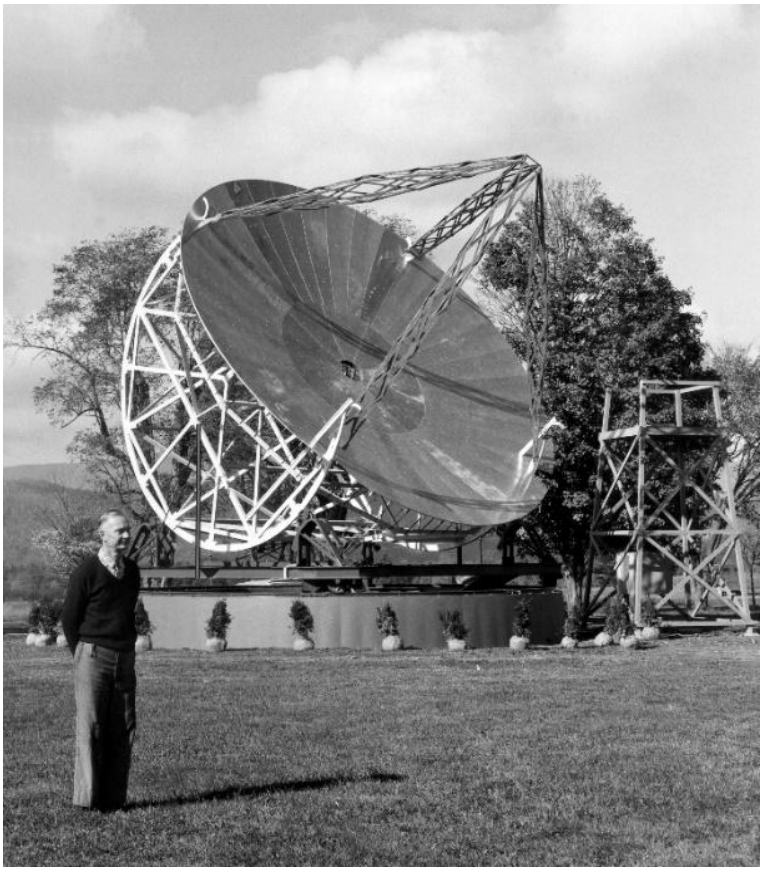

Fig. 1.2: Reber's radio telescope.

The radio telescope could scan different areas of the celestial sphere by varying the inclination of the antenna and taking advantage of the Earth's rotation. He began by repeating Jansky's observations and he conducted the first sky survey in the radio frequencies. In this way, he was able to prove the validity of the discovery of Karl Jansky because he revealed the strong emissions along the plane of the Milky Way. After collecting enough data, in 1944 he published the first radio frequency sky map (Fig. 1. 3).

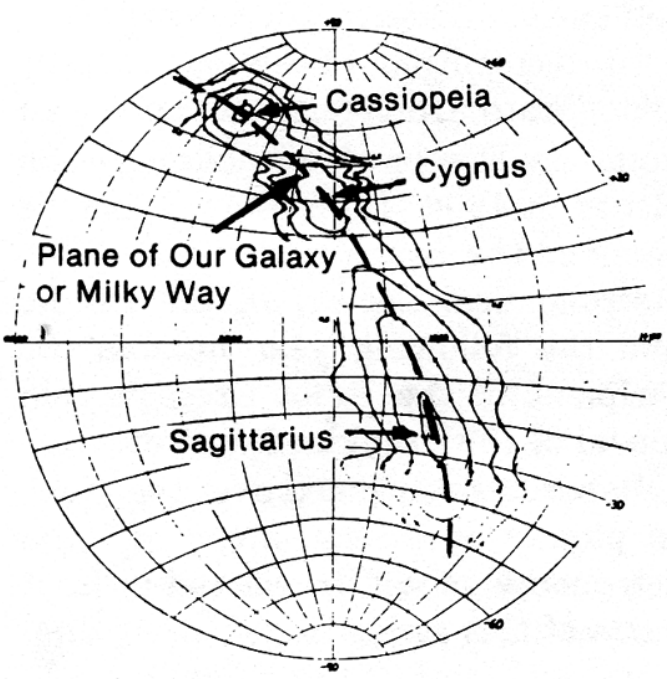

Fig. 1. 3: Copy of first radio frequency sky map by Reber.

After the World War II, radio astronomy developed rapidly, and has become of vital importance in the observation and study of the universe. In 1963, Schmidt discovered the first QUASAR (Quasi-stellar Radio Sources). QUASAR is the most energetic and distant members of extra-galactic objects. Quasars are smaller than normal galaxies, but extremely luminous and identified as being high redshift sources of electromagnetic energy (Fig. 1.4).

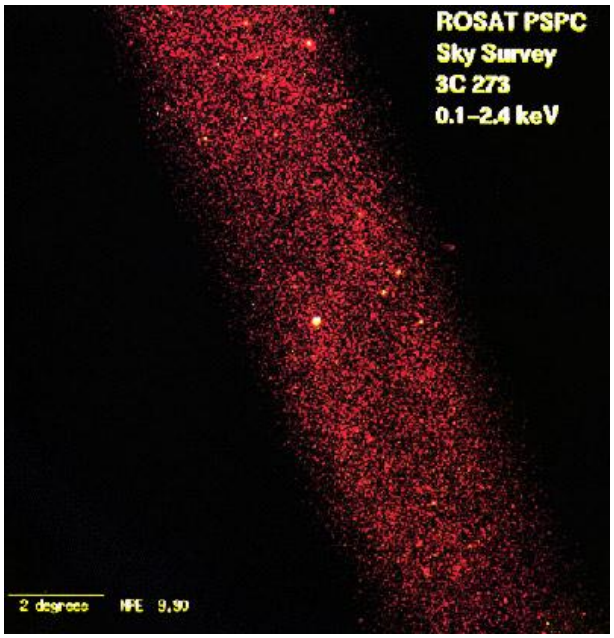

Fig. 1.4: First quasar discovered 3C 273.

In 1965, Penzias and Wilson discovered the cosmic microwave background radiation at 2.726K, during their studies of noise sources of the first satellite broadcasting by means of a microwave radiometer invented by Dicke in the 40s. This cosmic background radiation is an isotropic radiation present in the universe that is independent of the direction of antenna pointing and time of observation (Fig. 1.5)

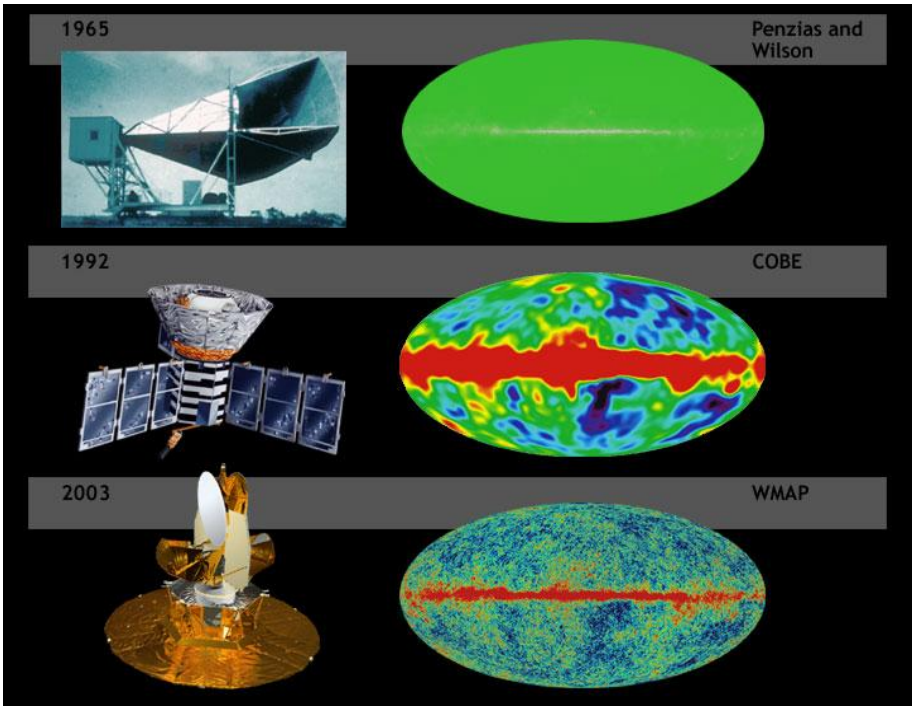

Fig. 1.5: Cosmic microwave background; the horizontal band at the centre of each image is due to the emission of our galaxy, which is added in remarks to background radiation.

This discover is one of the greatest proofs of the Big Bang. This radiation seems to be the fossil residue caused by the subsequent expansion of the radiation that permeated the universe in its first moments of life.

In 1967, Hewish and Bell discovered the first PULSAR (Pulsating Radiosource: PSR). Even in this case, the discovery occurred randomly: two scientists studied compact radio sources quasar by analysing the phenomenon of scintillation of these sources. The recordings, however, showed substantial and regular signal fluctuations. Optimizing the time constant of the receiver, they highlighted a series of pulses characterized by a regular repeat period and theoretically, generated by objects in the final stages of their evolution. These were pulsars or neutron stars (Fig. 1.6).

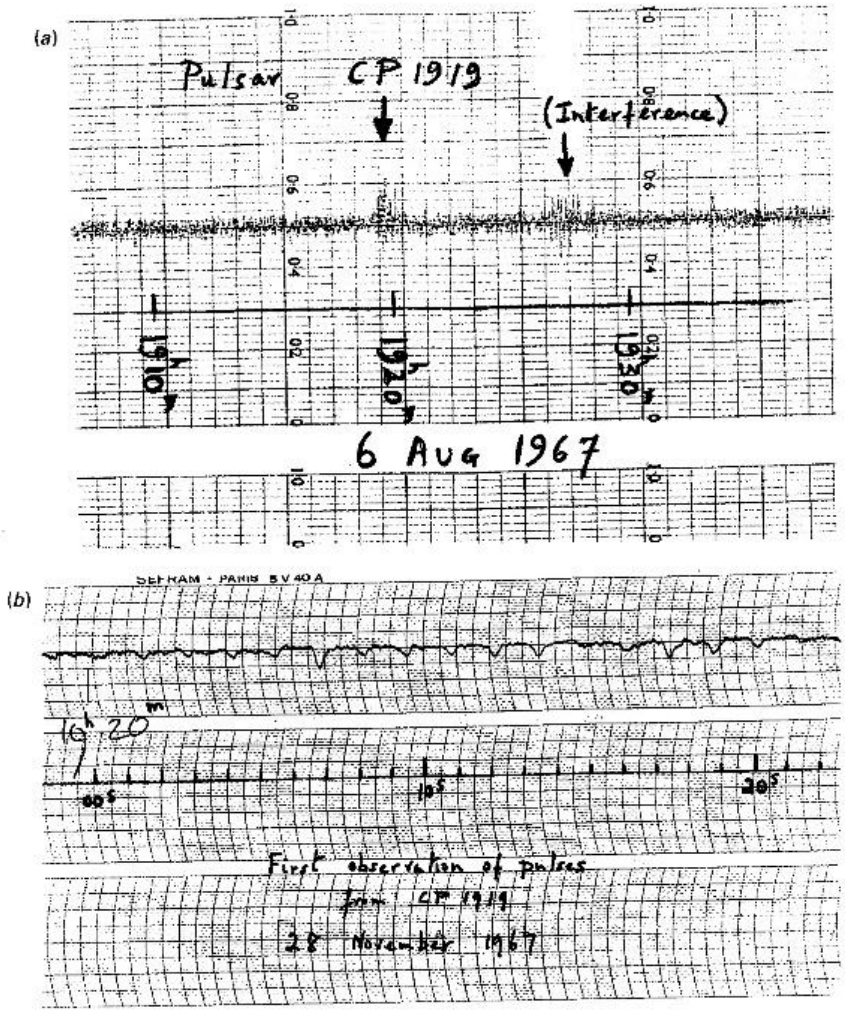

Fig. 1.6: Copy of the chart recorder output on which are the first recorded signals from a pulsar (PSR B1919+21).

From the second half of the 60s to the present day, radio astronomy research and technology are increasingly side-by-side. In fact, today the radio astronomy is not just a collection of the results, but also a science concerned with the instruments used to gather data. Technology has improved the radio interferometric techniques by using state-of-art hardware and software that allowed us to develop "radio images" of the observed objects increasingly defined and reliable, by means of the processing of data in a timely manner.

In conclusion, radio astronomy research in Italy began in 1942 at the Arcetri Astrophysical Observatory (Florence) with studies of solar radio emission.

1.2.Radio telescopes [2-3]

Radio astronomy is conducted using large radio antennas referred to as radio telescopes, that are either used singularly, or with multiple linked telescopes utilizing the techniques of radio interferometry and aperture synthesis. Radio telescopes are reflector antennas that collect the radio power from the distance celestial sources. Reflector antennas, used in radio astronomy (Fig 1.7), consist of one or more mirror(s), where the primary mirror is very large in terms of wavelength because astronomical signals are extremely weak.

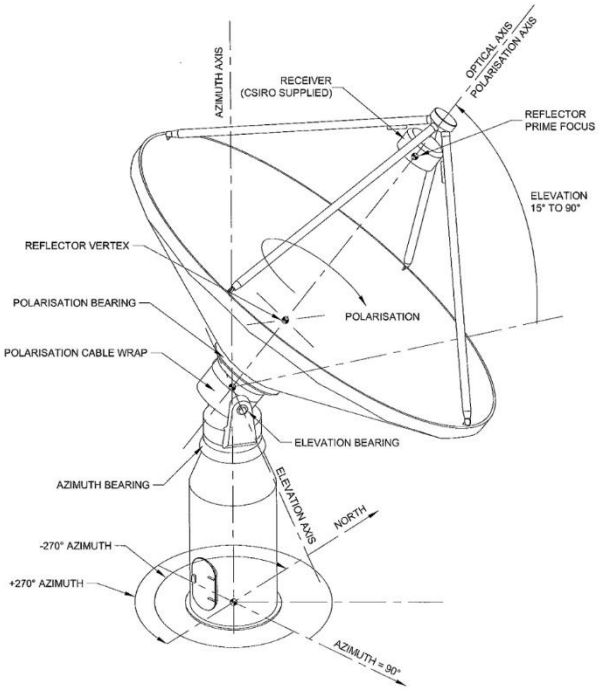

Fig. 1.7: Radio telescope.

There are different configurations of reflector antennas, depending on mirror type, number of mirrors, optical geometry, etc. The most common mirror types are paraboloid, hyperboloid and ellipsoid. The reflectors can be symmetric or offset, shaped or unshaped. They can have one, two or more mirrors, which may be arranged in Gregorian, Cassegrain, beam-waveguide configurations. In all of these configurations, the primary mirror is a paraboloid and focuses plane waves from distant sources onto a single focal point F (Fig. 1.8).

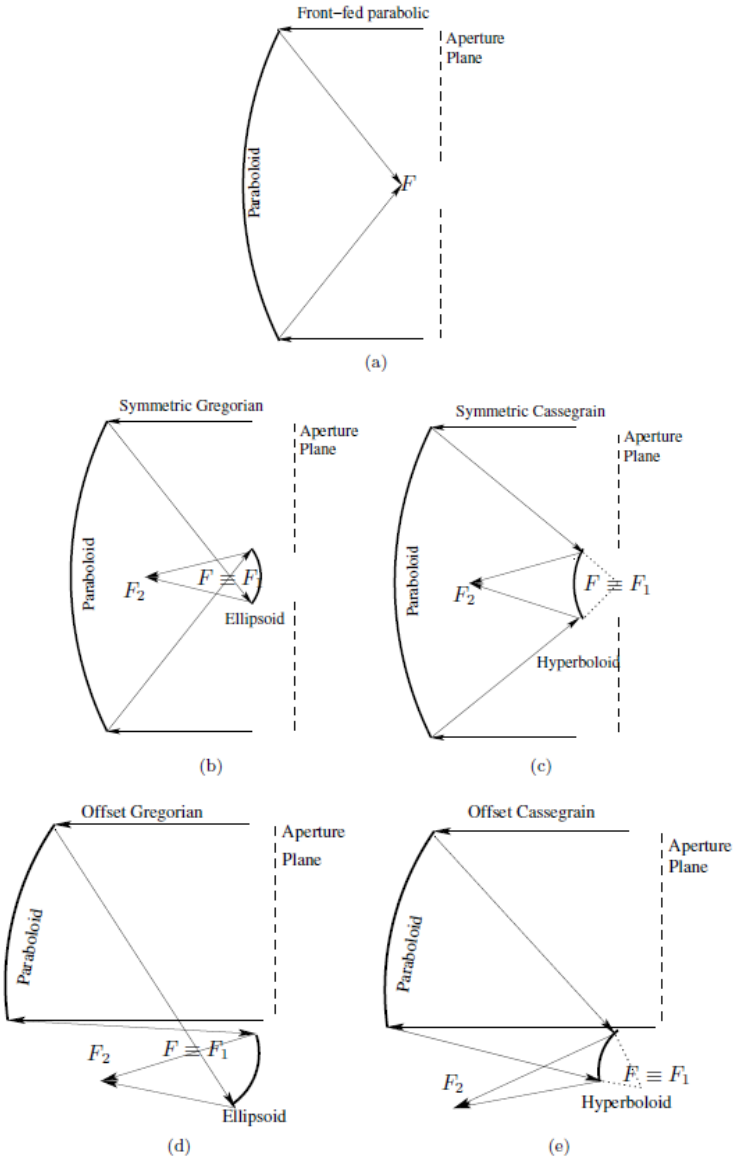

Fig. 1.8: Reflector antenna optical configurations used in radio astronomy [3].

The Gregorian configuration comprises an ellipsoidal secondary mirror in addition to the parabolic primary. The focal point of the parabola, F, and one of the foci of the ellipsoid, F1, coincide; the feed antenna is located or at the focal point of the parabola, F (primary focus), or at the other focal point of the ellipsoid, F2 (secondary focus). The Cassegrain configuration comprises a hyperboloidal secondary mirror in addition to the parabolic primary. The focal point of the primary coincides with the hyperboloid's focal point behind the secondary mirror F1; the feed antenna is located or at the focal point of the parabola, F (primary focus), or at the other focal point of the hyperbole, F2 (secondary focus). The difference between the symmetric configurations and the offset configurations is the aperture blockage due to the secondary mirror, which reduces the aperture efficiency of the antenna.

Some example of parabolic-reflector radio telescopes are:

- Arecibo (Puerto Rico), is the largest curved focusing dish on Earth; the main collecting dish is 305 m in diameter, constructed inside the depression and oriented toward the zenith (Fig.1.9a);
- Effelsberg (Germany) is the biggest radio telescope single dish in Europe; the main dish is 100m in diameter (Fig. 1.9b);
- SRT (Sardinia Radio Telescope), in Italy, is the biggest radio telescope single dish in Italy; the main dish is 64m in diameter.

Fig. 1.9: Arecibo radio telescope in the left and Effelsbeg radio telescope in the right.

To solve the problem of low resolving power and thus avoiding the realization of antennas with diameters larger and larger, Michelson developed a system known as interferometry principle, that is, exploit the work simultaneous and synchronized of more antennas away from each other but which increase virtually the receiving surface system receiver.

Two different configurations use this principle. In the first case, the astronomical interferometry consists of more antennas, with a very small diameter, distributed on a particular system rail or fixed and equivalent to a big collecting area. Some examples:

- VLA (Very Large Array) in New Mexico, consists of 27 antennas, each 25m in diameter, distributed on a system of rails shaped like a "Y" of 36 km length with resolving power like an antenna single dish with 130m of diameter;
- Plateau de Bure Interferometer (France) consists of six antennas, each 15 m in diameter, distributed on two rails that enable the antennas to be moved up to a maximum separation of 760 meters;
- SKA (Square Kilometer Array) is currently the biggest radio telescope project and it will consist of roughly 3000 dishes and possibly many more dipole elements, which, in aggregate, will amount to a square kilometer collecting area.

In the second case, the astronomical interferometry is called VLBI (Very Long Baseline Interferometry). It consists of multiple radio telescopes distributed on

Earth that observe the same celestial source in the same moment. This allows us to emulate a telescope with a size equal to the maximum separation between the telescopes. The distance between the radio telescopes is calculated using the time difference between the arrivals of the radio signal at different telescopes. Both the American network and the European network performs the VLBI observations. Italy contributes with SRT and two stations, constructed for the purpose, one located in Medicina, Bologna, and the other in Noto, Sicily (fig. 1.10). Each station is a single dish antenna with a diameter of 32 m, fully adjustable in azimuth and zenith, operating on the frequency bands between 327 MHz and 24 GHz.

Fig. 1.10: I-VLBI

1.3.Sardinia Radio Telescope

The Sardinia Radio Telescope (SRT) [4] is a new Italian radio telescope located on the Sardinia Island, Italy (Fig. 1.11). It is fully steerable 64-m diameter radio telescope capable of operating with high efficiency from 300 MHz up to 115 GHz.

Fig.1.11: Sardinia Radio Telescope (SRT).

The antenna is based on the shaped Gregorian optical configuration (fig. 1.12), obtained with the primary mirror “nearly” parabolic and the secondary mirror “nearly” elliptical. The shaped design improves the antenna performance, conserving at the same time the desirable characteristics of a pure classical Gregorian configuration.

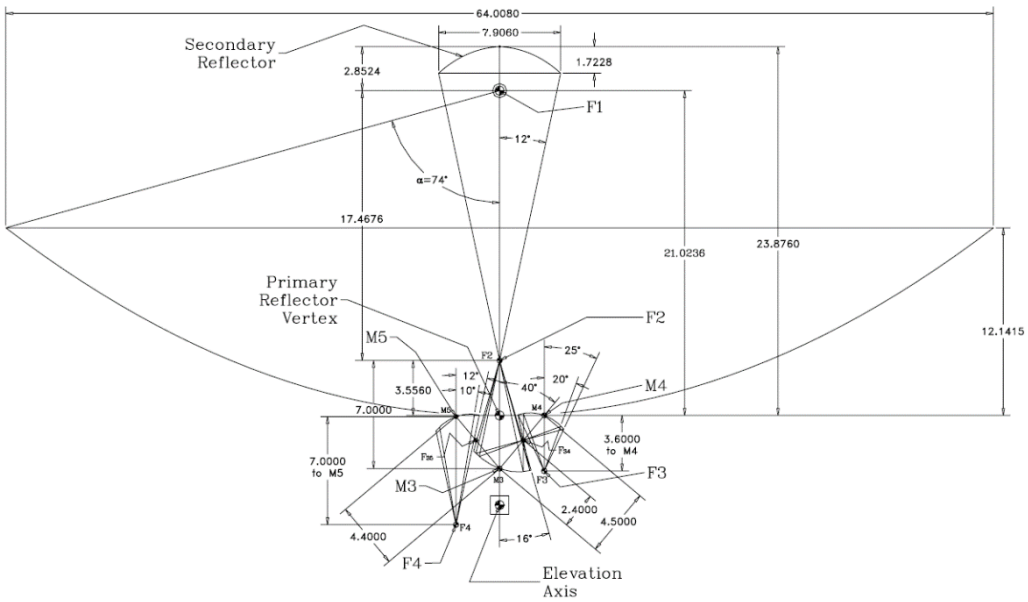

Fig. 1.12: SRT optical configuration.

In fact, the primary mirror is made-up of 1008 individual aluminium reflecting panels and 1116 mechanical actuators. In this way, it is possible modify the shape of the primary surface by means on individual panels, and correct the deformation of the surface induced by the gravitational and thermal deformations. It is also

possible convert the shaped primary reflector into a parabolic one to allow primary focus operations at relatively high frequencies. The secondary mirror is made-up of 49 individual aluminium panels.

This optical configuration, that reduces the spillover and the standing wave bouncing between the two reflectors and improves the antenna efficiency, allowed us to design SRT with six different focal positions that operate in different frequency ranges. This is a peculiar characteristic of SRT and makes the antenna a highly flexible instrument. The focal positions are:

- Primary (F1) with F/D ratio of 0.33 and frequency range between 300MHz÷20GHz;
- Gregorian (F2) with F/D ratio of 2.35 and frequency range between 7.5GHz÷115GHz;
- Beam-Wave Guide (F3, F4, F5, F6) with F/D ratio of 1.37 & 2.84 and frequency range between 1.4GHz÷35GHz.

The primary focus has a feed edge illumination of 74°with 12-15dB of edge taper, while for the Gregorian focus the half angle is 12° with 9-12 dB of edge taper [5].

Basically, the tasks SRT must carry out are four:

- Working as single dish antenna: it is able to explore vast regions of the sky both with continuum observations and with spectral line observations;
- Create the first completely Italian VLBI network (I-VLBI) and bring a large contribution to the European VLBI (EVN), making it competitive compared to the US network (VLBA);
- Bring benefits to European Geodynamics Network because its geographical position favours the study of the morphology of the Mediterranean area and the convergence of the Eurasian and African plates;
- Track interplanetary probes NASA-ESA missions and perform experiments to space science since it is able to operate in transmission mode in the X-band (8.8 GHz) and Ka (32-35 GHz).

At the moment three receivers have been already installed and working: a dual-frequency L-P Band from F1 operating simultaneously in the frequency ranges between 0.305-0.410 GHz (P band) and 1.3-1.8 GHz (L band)[6]; a mono-feed C-Band working at 5.7-7.7 GHz from F3 and a seven-feed K-band able to observe the sky from F2 between 18-26 GHz[7].

1.4.Radio astronomical receivers [2-8]

The radio astronomical receivers are devices that measure the radio emissions coming from celestial sources [2]. Namely, these devices convert the weak electromagnetic energy from space into a measurable electrical signal. Such receivers must be broadband, very sensitive and designed to measure noise because of the nature of the signal emitted by celestial sources. In fact, the electromagnetic signal that the receivers must capture and measure, in addition to being very weak, it is a random signal with components uncorrelated with each other, with different frequencies and with zero mean value; i.e. it is like the thermal noise produced by a resistor subject to a temperature. Therefore, the weakness and the peculiarity of these signals make the radio astronomy receivers other than those used in the telecommunications.

The radio astronomical receiver (Fig. 1.13) is like super-heterodyne receiver and it can be divide in four blocks: a feed-horn antenna, a front-end, a mixer, and a backend.

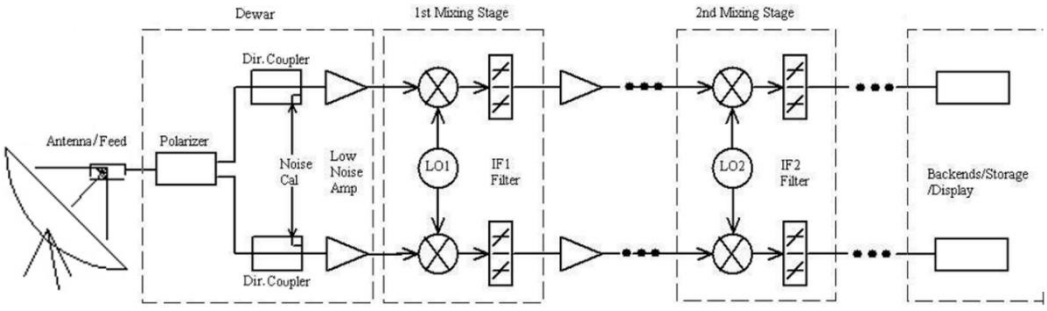

Fig. 1.13: Block diagram of a radio astronomical receiver.

The feed-horn antenna is positioned on the focus of the radio telescope. It is used to adapt the antenna beam and to collect all the energy collected by the mirror of the radio telescope and concentrated on his focus.

The dewar is a container, usually cylindrical, and it contains all those devices that are involved in the amplification of the signal (Low Noise Amplifier, bandpass filters), in the separation of the two linear polarizations (Ortho Mode Transducer) or circular polarizations (polarizer) and in the calibration (directional couplers, power divider). All devices compose the front-end of receiver and work at cryogenic temperatures (20°K -70°K). The very low temperatures allow minimizing the noise produced mainly by the amplifier, which it is required to amplify the weak signal. In addition, since the signal coming from the sky is unknown, it is necessary to calibrate the receiver by injecting, using the directional couplers, a signal of known power (noise generator).

The mixer allows shifting the frequency of the received signal to a lower frequency, said intermediate frequency. This is necessary because often the useful signals are at a frequency too high. With the mixer, there are also the band-pass filters, the low noise amplifiers and the insulators. These devices work at room temperature (300 ° K).

The Backend is last block of the receiver chain. It analyse the polarization, time structure or spectral properties of broadband radiation. In particular, this block measure Stokes parameters as a function of time, frequency, polarization status. For this reason, there are different backends depending on the nature of the observations: total power, polarimetry, spectroscopy, interferometry, pulsar (search and timing). It can also record the instantaneous field E(t) for further processing like VLBI/ Remote interferometry or it can combine of the above (e.g. spectropolarimetric interferometry). It consists of A/D converter, FPGA based boards, and GPU based nodes.

All of the elements aforementioned limit the sensitivity of the receiver because cause the thermal noise. Since the receiver must measure weak signals, this noise merges with the signal of interest and, then, it is indistinguishable. Therefore, to characterize the quality of the receiver we define the noise temperature of the system Tsys. If Tsys is the noise temperature of system, B is the bandwidth of the receiver, N is the number of records, and τ0 is the time constant of the integrator; the minimum detectable signal ΔT is:

$$\Delta T \geq \frac{T_{sys}}{\sqrt{B*N*\tau_0}} \qquad [^{\circ}K] \qquad [1.1]$$

Equality is valid if the receiver is ideal, that is perfectly stable.

Chapter 2: Quadrature hybrid with very flat phase response

Quadrature hybrids are 3dB directional couplers with 90° phase difference in the outputs and these devices are four-port network [22]. Quadrature branch-line hybrids are passive components widely used at microwave frequencies to design transmitting and receiving systems. In particular, the quadrature hybrid is an element largely used in the radio astronomical receivers. It is installed between a corrugated horn that collects the radiation from the telescope and an ortho-mode transducer that separates the orthogonal polarizations and it is used to modulate the tiny input signal from the sky, so as to accurately recover the polarization state in the presence of noise. These devices can be realized by using either waveguide or planar technology. In the latter case, branch-line hybrids can be very small compared to their waveguide equivalents. In general, good performance and the required 90° phase response are normally achieved only within narrow bandwidths, 10-20% around the central operational frequency, because of the quarter-wave length requirements.

When the previous components are used in radio astronomy, broadband performances and very flat phase-response are required [13]. In fact, the polarizer with very flat phase response is fundamental in polarimetric observation where the main issue is the calibration between left and right polarizations. Left and right polarizations have to be phased correctly so as to get cross-correlations and, finally, calculates the Stokes parameter. A spurious phase shift between left and right circular polarization causes a rotation of the observed polarization angle by an amount that increases linearly with the frequency. This effect is more noticeable as the deviation from flat phase-response increases.

In this chapter, we will propose a new quadrature hybrid that overcomes the above limits. The design is based on the transposition in microstrip technology of a combination of waveguide components used to build broadband polarizers [9-12].

2.1. Concept

Rectangular waveguide phase-shifters can be realized using dual polarized circular waveguides and a combination of 90° and 180° differential phase sections [9], i.e. using Quarter-Wave Sections (QWSs) and Half-Wave Sections (HWSs) respectively [10]-[11]. In these designs, a rectangular-to-circular waveguide transition transforms a TE10 mode into a circular waveguide TE11 mode. A 45º oriented QWS converts it into an RHCP mode. An HWS, arbitrarily rotated by an angle ϑ, introduces a phase-shift equal to 2ϑ. A second QWS, parallel to the first one, brings back to the TE11 mode. A final circular-to-rectangular waveguide transition restores the TE10 mode. As proved in [11], this configuration provides a frequency-flat phase-shift response equal to twice the mechanical rotation angle, i.e. $\Delta\phi=2\vartheta$.

It is possible to modify the above design removing the input and output transitions. This dual polarised device, QWS45 × HWSϑ × QWS45 introduces opposite phase-shifts on the two orthogonal x and y polarisations: $\Delta\phi=\pm2\vartheta$. It is clear that a device of this type, with the internal HWS rotated by $\vartheta=22.5°$, would introduce phase-shifts of $\Delta\phi=\pm45°$ with an overall 90º phase-difference between the two orthogonal polarizations. This QWS45 × HWS22.5 × QWS45 configuration behaves like a waveguide polarizer with phase response very flat across the band. This polarizer can be rotated by 45° and be used to convert x/y polarizations to RH/LH circular polarizations very efficiently. A very broadband waveguide polarizer based on this idea has been develop [12].

The key idea of this work is that the matrix of a quadrature hybrid is equivalent to the matrix of a waveguide polarizer rotated by 45º, having set a correspondence between the polarizer x and y directions and the Ports 1 and 4 of the hybrid (Fig. 2.1). In particular, a new planar quadrature hybrid, proposed here, is the microstrip transposition of the broadband waveguide polarizer discussed above.

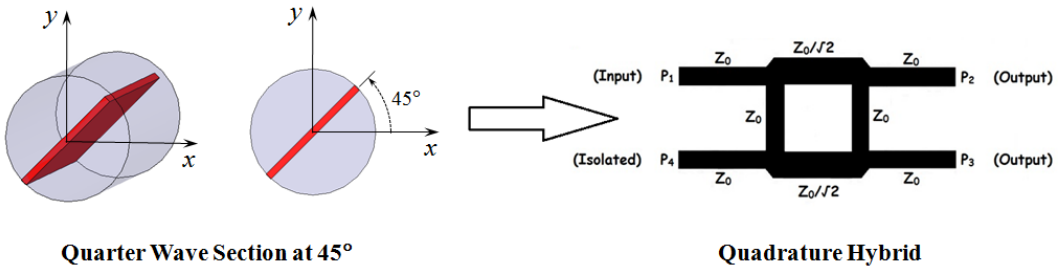

Fig. 2.1: A planar quadrature hybrid is equivalent to a waveguide polarizer rotated by 45° setting a correspondence between the x and y polarized modes and port 1 and 4 of the hybrid.

2.2.Design

In the design of optical systems, lossless dual polarized devices can be modelled using the 2x2 Jones matrix formalism [14]. In a generic optical system, if the electric field vectors of the incoming and outgoing signals are defined respectively as $\vec{E} = \begin{pmatrix} E_x \\ E_y \end{pmatrix}$ and $\vec{E}' = \begin{pmatrix} E'_x \\ E'_y \end{pmatrix}$, the Jones matrix $J = \begin{pmatrix} a & b \\ c & d \end{pmatrix}$ of the optical system relates them according to following equation:

$$\vec{E}' = J\vec{E} \rightarrow \begin{pmatrix} E'_x \\ E'_y \end{pmatrix} = \begin{pmatrix} a & b \\ c & d \end{pmatrix} \begin{pmatrix} E_x \\ E_y \end{pmatrix} \quad [2.1]$$

An ideal QWS with the fast axis parallel to the x axis has a matrix: $QWS_{0^\circ} = \frac{1}{2}\begin{pmatrix} 1 & 0 \\ 0 & i \end{pmatrix}$, whereas the matrix of a QWS rotated by ϑ=45º will be: $QWS_{45^\circ} = \frac{1}{\sqrt{2}}\begin{pmatrix} 1 & -i \\ i & 1 \end{pmatrix}$. This latter 4-port device splits both the x and y components of the incident field into two 3dB output signals with ±90° phase-shifts. In strict analogy, a quadrature hybrid also is a four-port device that splits two input signals (on Port 1 and 4) into two 3dB output signals (Port 2 and 3) with ±90° phase-shifts. In the first case the device has two dual polarized circular waveguides; in the second case there are four single mode waveguides or planar transmission lines (Fig. 2.1).

The broadband waveguide polarizer has its fast axis aligned with the x axis, i.e. at 0°:

POL0 = QWS45 × HWS22.5 × QWS45. [2.2]

In order to use the analogy with the quadrature hybrid, we need to rotate it by 45°:

POL45 = QWS90 × HWS67.5 × QWS90. [2.3]

In addition, the HWS can be made cascading two QWSs:

HWS67.5 = QWS67.5 × QWS67.5. [2.4]

and so the final Jones matrix of our device will be:

POL45 = QWS90 × QWS67.5 × QWS67.5 × QWS90. [2.5]

In conclusion, in order to design a broadband microstrip hybrid we need to design two circuits with their scattering matrices equivalent to a QWS rotated by 90° and 67.5° and then cascade them following the configuration in equation [2.5].

In microwave engineering, N-port networks are described using the scattering matrix S. This relates the voltage wave vector incident on port n, $[V_n^-]$, to the voltage wave vector reflected from port n, $[V_n^+]$, according to the following equation:

$$[V_n^-] = [S][V_n^+] \rightarrow \begin{bmatrix} V_1^- \\ V_2^- \\ \cdots \\ V_n^- \end{bmatrix} = \begin{bmatrix} S_{11} & S_{12} & \cdots & S_{1n} \\ S_{21} & S_{22} & \cdots & S_{2n} \\ \cdots & \cdots & \cdots & S_{3n} \\ S_{n1} & S_{n2} & \cdots & S_{nn} \end{bmatrix} \begin{bmatrix} V_1^+ \\ V_2^+ \\ \cdots \\ V_n^+ \end{bmatrix} \quad [2.6]$$

where the elements Sij (i ≠ j) represent the relation between the voltage wave incoming on port j and the voltage wave outgoing on port i; the elements Sii represent the relation between the voltage wave incoming and outgoing on the same port i. Considering the definition of Sij, it is possible to find a correspondence between some of its elements (those related to the transmissions) and the Jones matrix elements. Referring to the Jones and scattering matrix four-port networks shown in Fig. 2.2, it is possible to write the following relationships:

$$a = \frac{E_x'}{E_x} \quad \leftrightarrow \quad \frac{V_2^-}{V_1^+} = S_{21} = S_{12} \quad [2.7a]$$

$$b = \frac{E_x'}{E_y} \quad \leftrightarrow \quad \frac{V_2^-}{V_4^+} = S_{24} = S_{42} \quad [2.7b]$$

$$c = \frac{E_y'}{E_x} \quad \leftrightarrow \quad \frac{V_3^-}{V_1^+} = S_{31} = S_{13} \quad [2.7c]$$

$$d = \frac{E_y'}{E_y} \quad \leftrightarrow \quad \frac{V_3^-}{V_4^+} = S_{34} = S_{43} \quad [2.7d]$$

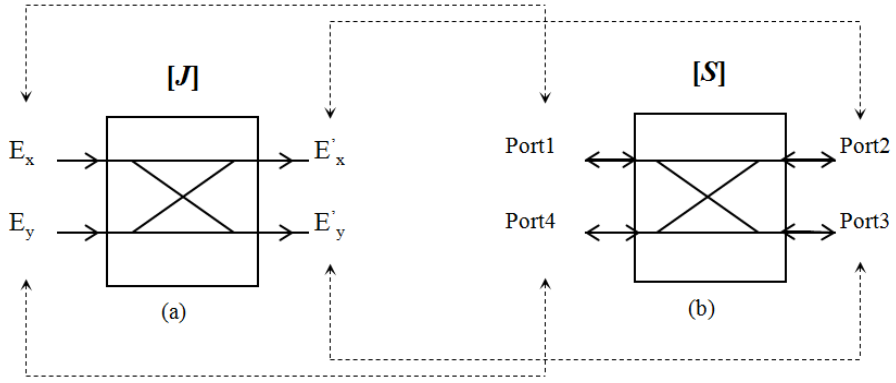

Fig. 2.2: Four-port network associated to an optical device using the Jones formalism (a) and that associated to a microwave device using the scattering matrix formalism (b).

The relations [2.7] allow to find the scattering matrices representing the two rotated QWSs required to design the quadrature hybrid. Knowing that the Jones matrix of a QWS rotated by an arbitrary angle ϑ has the following elements:

$$a = cos^2\vartheta + jsin^2\vartheta \quad [2.8a]$$

$$b = (1-j)cos\vartheta sin\vartheta \quad [2.8b]$$

$$c = (1-j)cos\vartheta sin\vartheta \quad [2.8c]$$

$$d = sin^2\vartheta + jcos^2\vartheta \quad [2.8d]$$

it is possible to find the scattering matrix of the equivalent four-port device:

$$[S] = \begin{bmatrix} 0 & a & c & 0 \\ a & 0 & 0 & c \\ b & 0 & 0 & d \\ 0 & b & d & 0 \end{bmatrix} \quad [2.9]$$

The form of this matrix is the same as that of a branch-line coupler with arbitrary power division. There are many different designs available in the literature for this kind of devices [15]-[19]. In this work we have adopted two of these devices and designed the quadrature hybrid cascading two pairs of these branch-line couplers.

The circuit schematics of the two branch-line couplers having the same scattering matrices of the QWSs of interest are shown in Fig. 2.3. These devices, described in [15] and [16], identify respectively the QWS67.5° and the QWS90°.

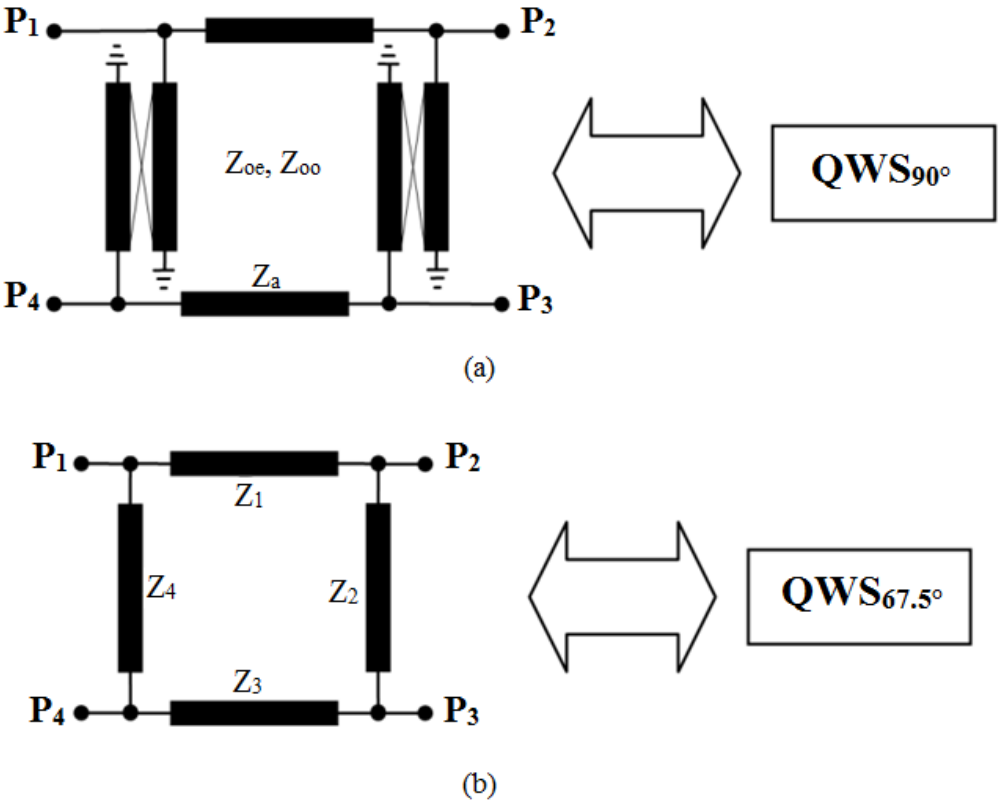

Fig.2.3: Correspondence between the branch-line couplers with arbitrary power division and the two QWSs of interest: QWS67.5° and QWS90°.

In [15], the arbitrary power division is obtained controlling the characteristic impedances of the line of device by using the following equations:

$$Z_1 = Z_3 = \sqrt{\frac{d_1^2}{d_1^2 + d_2^2}} \quad [2.10a]$$

$$Z_2 = Z_4 = \frac{d_1}{d_2} \quad [2.10b]$$

where d_1 and d_2 are respectively |S21| and |S31|. In [16], the large power division is obtained replacing the vertical lines of the branch-line with the shorted parallel coupled-line sections according with the following equations:

$$\frac{Z_a}{Z_0} = \frac{d}{\sqrt{1+d^2}} \quad [2.11a]$$

$$\frac{2}{Z_0(Y_{oo}-Y_{oe})} = d \quad [2.11b]$$

where $d = 10^{\Delta/20}$, $\Delta(dB) = |S_{21}| - |S_{31}|$ and Z_0 is the port impedance.

All the transmission lines extend for a quarter of wavelength, whereas their impedances are different as reported in Table 2.1.

$QWS_{67.5°}$	**Z_1** = 42.9 **Ω**	**Z_2** = 83.5 **Ω**	**Z_3** = 42.9 **Ω**	**Z_4** =83.5 **Ω**
$QWS_{90°}$	**Z_a** = 49.75 **Ω**	**Z_{oe}** 55.24 **Ω**	**Z_{oo}** 45.45 **Ω**	

Tab. 2.1: Branch-line couplers line impedances.

A Rogers-RT Duroid 5880 substrate with a dielectric constant of 2.22 and a thickness of 0.25mm has been used for the final microstrip device. Fig. 2.4 shows the final layout of the proposed branch-line coupler where the four devices have been connected together by using six lines of 50 Ω impedance and a quarter wavelength in length. The device is designed to have its central operational frequency of 9.3 GHz.

The modelling was carried out using the finite-element analysis commercial software Ansoft HFSS [20]. The expected performances of device within a 33% band are: RL = -20 dB, IL = -3dB ÷ -4dB and phase difference = 90°±2°.

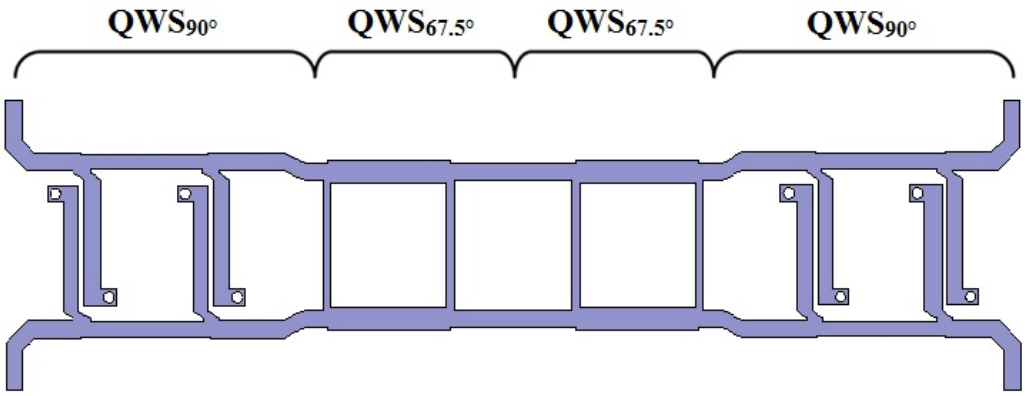

Fig. 2.4: Branch-line coupler proposed.

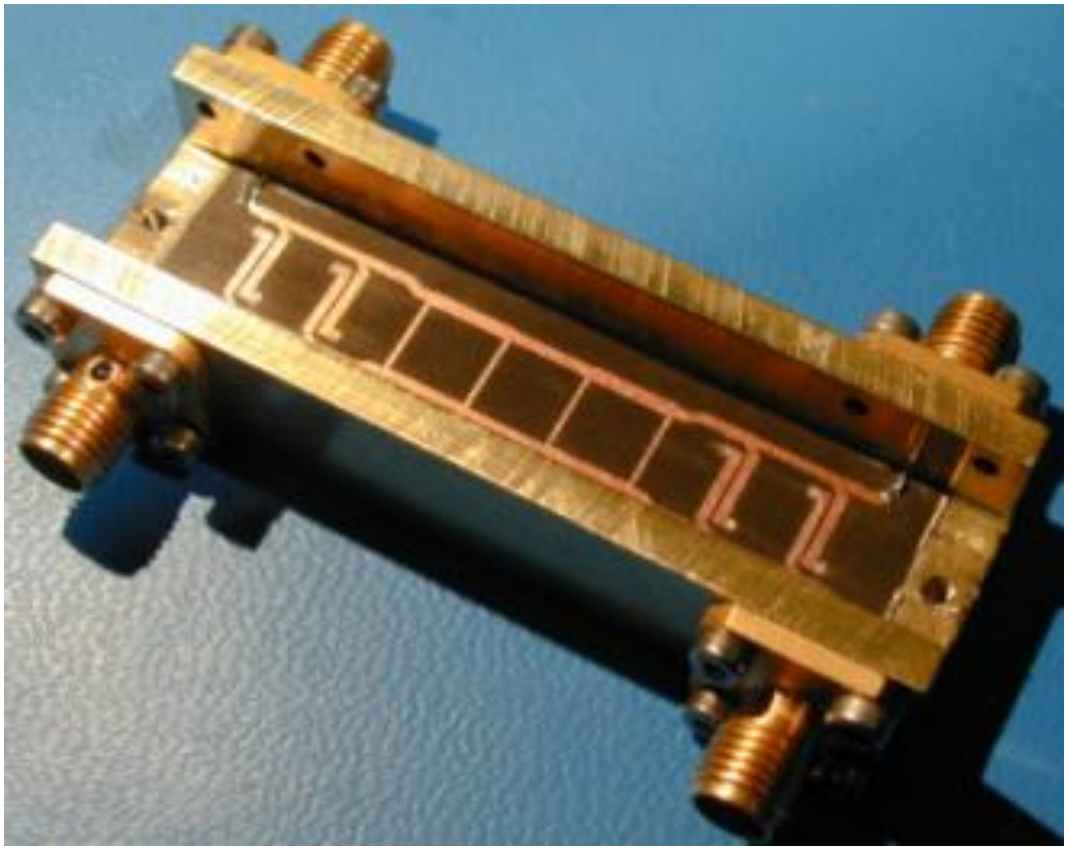

Fig.2.5: Branch-line coupler prototype.

The branch-line coupler was manufactured by the Trackwise Company [21]. A prototype, with dimensions 53.3 x 13 mm2, is showed in Fig. 2.5. The measurements were carried out using a Rohde & Schwarz ZVA40 Vector Network Analyzer (VNA). The results of the measurements and their comparison with the models are reported in Figs. 2.6, 2.7, and 2.8. Across a 32% bandwidth the Return Loss resulted below -15dB whereas the Insertion Loss between -3 dB and -4 dB. Part of these losses is due to the quarter wavelength microstrip lines used to connect the four branch-line couplers. Across the same bandwidth, the phase-difference resulted to be very flat: 90°±1.5°. These results show good performances in terms of phase difference and transmission.

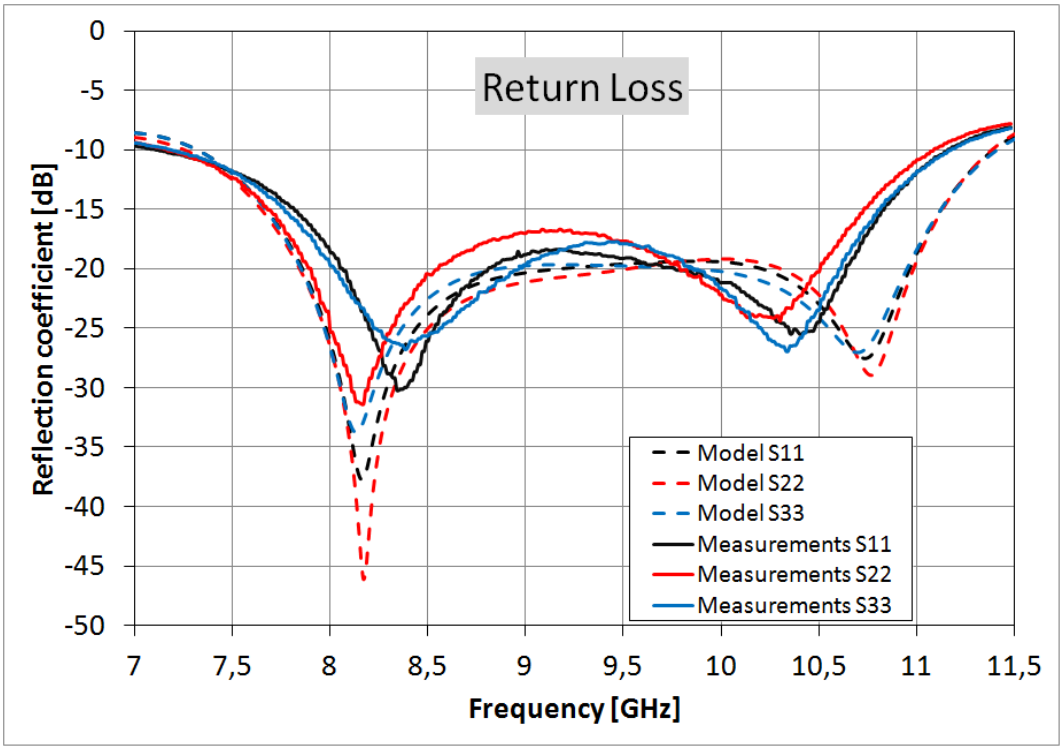

Fig. 2.6: Measured and simulated return loss.

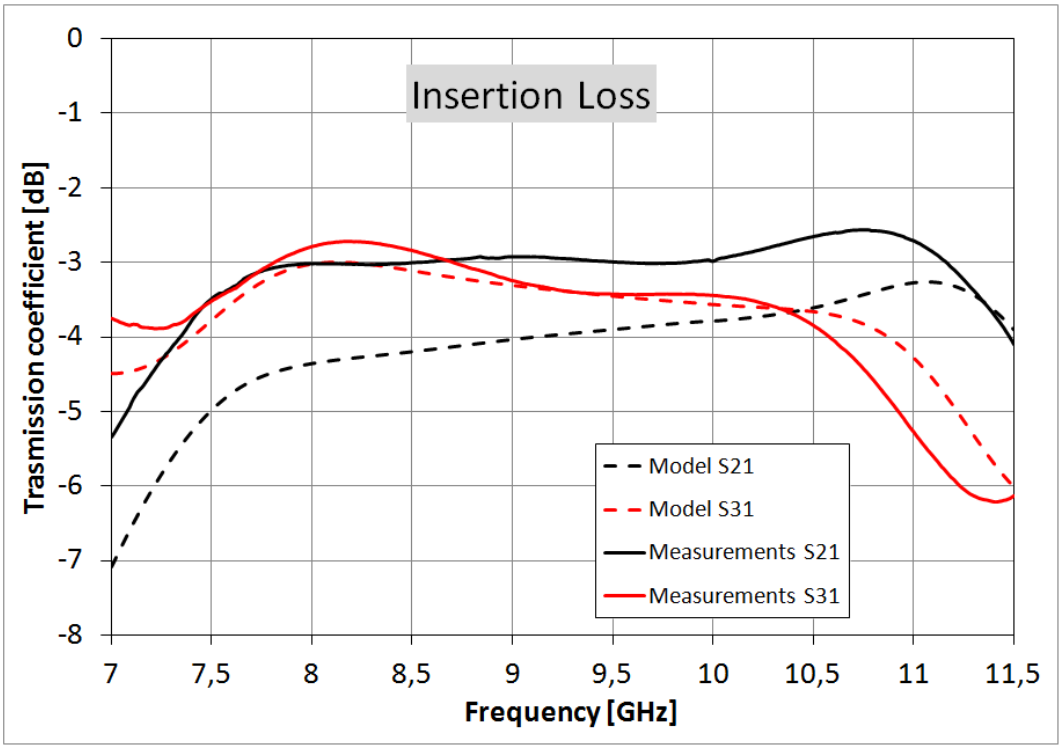

Fig. 2.7: Measured and simulated transmission.

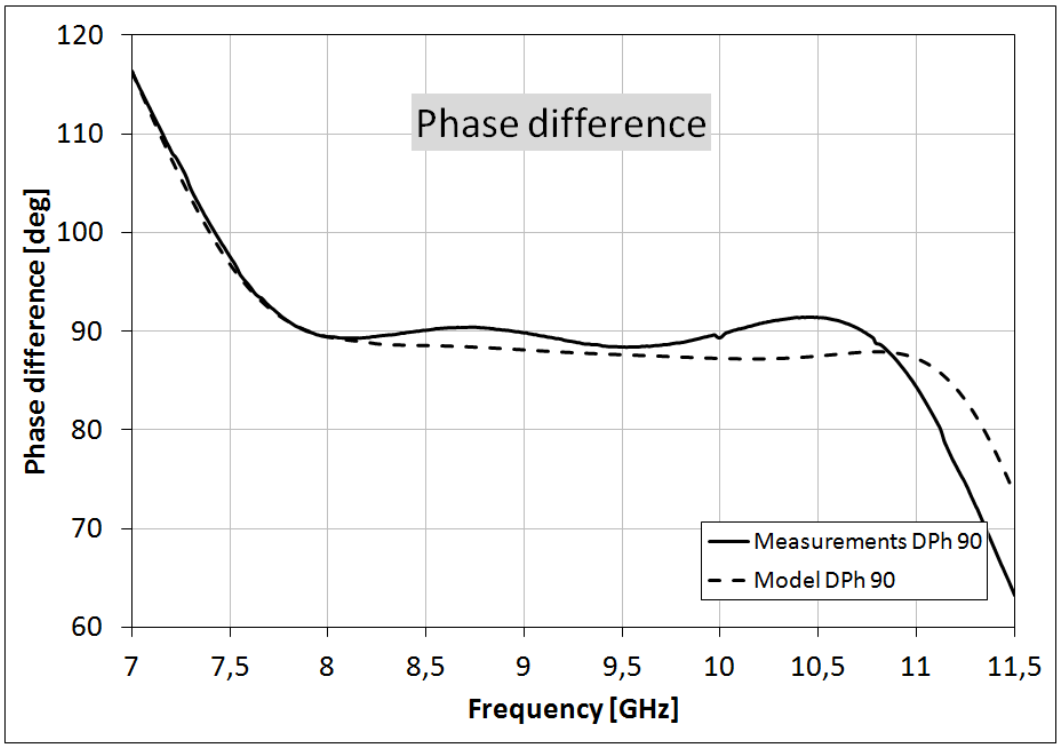

Fig.2.8: Measured and simulated differential phase-shift.

Chapter 3: A 3mm SIS receiver for the Sardinia Radio Telescope

The scientific and technical validations (commissioning phase) of the Sardinia Radio Telescope at the different frequencies has started in 2014 and is foreseen to continue for approximately two years. During the commissioning phase, all the devices foreseen for the telescope early activities and the acquisition systems for typical scientific observations must be successfully tested. In this contest, it is inserted the 3mm SIS receiver. Observations at ~3 mm wavelengths with SRT will enable to study a wide range of phenomena in the radio astronomy, for example, the astrochemistry of the interstellar cold gas clouds in which stars are being formed, besides to test the active surface and to perform VLBI-mm.

In this chapter, a 3 mm SIS receiver for the Gregorian focus of the Sardinia Radio Telescope is presented and the configuration chosen for the antenna installation.

3.1. 3mm SIS receiver

The 3mm SIS receiver (Fig 3.1) is developed at IRAM (Institute de Radio Astronomie Millimétrique) for the Plateau de Bure interferometer (PdBI) in the 90's. It was installed on one of the PdBI antennas until 2006, after which it was replaced by a receiver of newer generation.

The receiver covers two frequency bands simultaneously: the ~3 mm band (84 – 116 GHz) and ~1.3mm band (210 – 248 GHz) [23]. However, only the 3 mm band will be observed in SRT, while the 1.3 mm channel will remain unused because the atmospheric conditions at the site will not allow observations beyond ~116 GHz. The two channels are similar, both from the point of view of the optical path and from the point of view of the receiver chain, as is shown in Fig. 3.2.

Fig. 3.1: 3mm SIS receiver

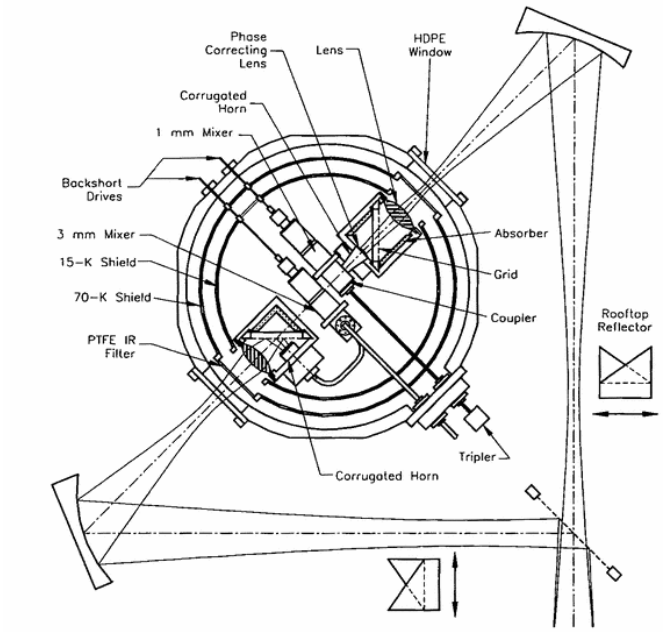

Fig. 3.2: Schematic with cryostat inner details.

The 3mm channel is located on the bottom left side of the drawing. Thanks to a broadband polarization grid, placed at the input of the ex-PdBI receiver, the RF signal is splitted in two orthogonal linearly polarized signals across ~84-248 GHz. Each of these signals is then directed in the two different optical paths, one for each path. Each receiver chain is composed of: a waveguide horn, a SIS mixer, a LNA and an isolator. The LNAs and isolators are not shown in the schematic because are mounted on the 15-K stage screen above the optics cubes. The SIS mixers operate at the physical temperature of 4K with very good performances in terms of noise figure. For this reason, the dewar is designed to have three different temperature stages: 70K, 15K and 4K. The Intermediate Frequency (IF) signal, generated by the mixer, has an instantaneous bandwidth of 500 MHz on both receiver channels. In the end, the calibration of this receiver is made through an ambient and cryogenic calibration loads, available for the 3mm and for the 1.3mm receiver channel, fitted externally as is shown in Fig 0 and Fig 1. The hot load, at the room temperature, moves into the beam before the polarization grid. To measure the cold load a rooftop mirror is put into the beam, after the external elliptical mirror, with a normal angle of reflection, that reflects the beam but with the polarization in opposite respect to the RF signal expected to that channel.

The Astronomical Observatory of Cagliari purchased this receiver from the IRAM to test the performances of the antenna at the millimeter frequencies (84 – 116 GHz), namely to test the active surface and to perform VLBI-mm and single-dish observations.

3.2. 3mm SIS receiver and SRT

Since the IRAM receiver was originally designed for the PdBI antenna, a new optical and mechanical configuration had to be studied to adapt the instruments to the SRT optics and to its cabin mechanical structure. The chosen optical configuration matches the beam waist radius of the receiver (without changing the existing feed-horn and inner optics) to the beam waist radius of the SRT antenna's Gregorian focus, following the Gaussian beam theory [24]. The mechanical configuration takes into account the available space in the Gregorian room and the rotating turret where the receiver will be installed.

3.2.1. Optical configuration

[23-24] describe the optics of the receiver in detail. In reference to the 3mm channel, the horn, designed to produce Gaussian beams, has a flare angle of 7.42° and the aperture diameter of 12.4 mm; the beam waist is close to the feed-horn aperture and the phase error is about 0.11λ-0.16λ. An HDPE (high-density polyethylene) lens with the focal length of 30mm is placed at 41.5mm of distance from the feed in order to refocus the beam. An external elliptical mirror with focal length 131.6mm is placed at 240mm of distance from the lens. The HDPE lens and the external mirror form together an achromatic doublet [25], which generates a beam waist of 3.85λ at 353mm of distance from the mirror. This beam waist value was required at the Cassegrain focus of the PdBI antenna to illuminate the dish with the desired edge taper level (Te), of order 12 dB (Fig. 3.3).

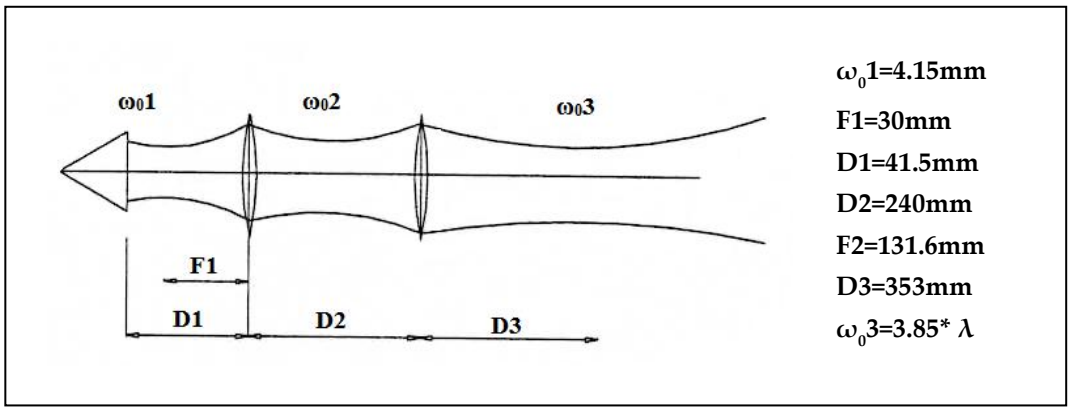

Fig. 3.3: Schematics of 3mm channel optics [24].

A new optical configuration was designed to ensure the compatibility of "receiver-antenna" within SRT. Since the optics of this receiver is based on the Gaussian beam theory [26], we used the Gaussian procedure to easily study our compatibility problem.

The standard set of equations governing the fundamental Gaussian beam propagation are used:

$$R = z + \frac{z_c^2}{z} \qquad [3.1]$$

$$\omega = \omega_0 * \sqrt{1 + \left(\frac{z}{z_c}\right)^2} \qquad [3.2]$$

$$\phi_0 = \tan^{-1}\frac{z}{z_c} \qquad [3.3]$$

where ω0 is the beam waist radius, ω the beam radius, zc the confocal distance, R the radius of curvature and ϕ0 the Gaussian beam phase shift, (Fig. 3.4).

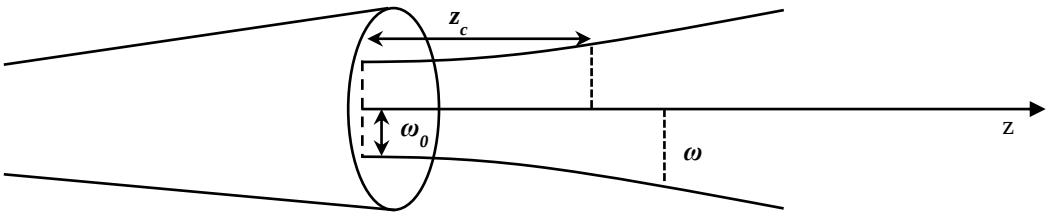

Fig. 3.4: Gaussian beam propagation from feed horn.

The beam waist radius is the minimal value of the beam radius; the beam radius is the value at which the field falls to *1/e* relative to its on-axis value. At the beam waist, the radius of curvature is infinite, characteristic of a plane wave front, and the phase shift is zero.

The confocal distance identifies a region used to define the propagation in "near field", $z << z_c$, or in "far field", $z >> z_c$, and is defined as:

$$z_c = \frac{\pi * \omega_0}{\lambda} \qquad [3.4]$$

At a distance equal to the confocal distance, the beam waist radius is equal to $\sqrt{2}*\omega_0$, the radius of curvature is $2*z_c$ (minimum value of radius of curvature) and the phase shift is $\pi/4$.

These Gaussian beam formulas describe the behaviour of the radiation emerging from a horn as function of distance from the waist. After propagating a distance larger than the confocal distance the beam grows significantly. The use of focusing elements allows confining the beam of radiation and avoids its excessive growth. A thin lens or a mirror can be used to refocus the beam and change its radius of curvature to produce a converging beam. In reference to our case, the equations that govern the Gaussian beam transformation by thin lens are the following:

$$d_{out} = f + \frac{d_{in} - f}{\left(\frac{d_{in}}{f} - 1\right)^2 + \left(\frac{z_c}{f}\right)^2} \qquad [3.5]$$

$$\mathfrak{M} = \frac{1}{\sqrt{\left(\frac{d_{in}}{f} - 1\right)^2 + \left(\frac{z_c}{f}\right)^2}} \qquad [3.6]$$

$$\mathfrak{M} = \frac{\omega_{0out}}{\omega_{0in}} \qquad [3.7]$$

where din and dout are the distances of the beam waist in input and output, $\omega_0$in and ω_{0out}, from the thin lens and $\mathfrak{M}$ is the thin lens magnification.

A simple system of two thin lenses, resulting in an achromatic doublet, is described in [25]. The main feature of the achromatic doublet is to give a constant output beam waist if the input beam waist is proportional to the wavelength (which is the case at the focus of a telescope). The equations for design this system of lenses is the following:

$$\omega_{0out}^2 * \omega_{0in}^2 = \frac{f_e^2 * \lambda^2}{\pi^2} \quad [3.8]$$

$$d = f_2 + \frac{x * f_1}{(x - f_1)} \quad [3.9]$$

$$f_e = \frac{f_2}{f_1} * (x - f_1) \quad [3.10]$$

$$x' = x * \left(\frac{f_2}{f_1}\right)^2 + f_2 * \left(1 - \frac{f_2}{f_1}\right) \quad [3.11]$$

where f_e is the equivalent focal length of the doublet, f_1 and f_2 are the focal length of the single thin lenses, x is the distance of the input beam waist from the first lens and x' is the distance of the output beam waist of the second lens (Fig. 3.5).

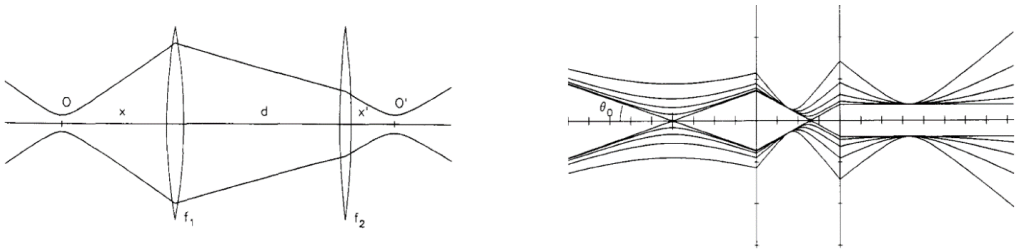

Fig. 3.5: *Left*: Geometry of doublet lenses; *Right*: Behaviour Gaussian beam for the Achromatic Doublet [28].

For our optical configuration, we use the formulas described above [3.1-3.11].

The beam waist radius required at the Gregorian focus of the Sardinia Radio Telescope to illuminate the antenna at the edge taper level of 13dB (frequency-independent illumination) is:

$$\omega_{0\_GREG} = 0.216 * \sqrt{T_e} * F_c * \lambda = 0.216 * \sqrt{13} * 2.35 * 3 = 5.491mm \quad [3.12]$$

The initial data of the 3mm horn [23-24] and the Sardinia Radio Telescope are listed in Tabs. 3.1-3.2.

	Horn beam waist radius horn	Horn HDPE lens distance	HDPE lens focal length
Rx 3mm	4.15 mm	41.5 mm	30 mm

Tab. 3.1: Parameters of the 3mm receiver.

	Primary reflector diameter	Secondary reflector diameter	Focal ratio at Gregorian focus	Edge taper level
SRT	64 m	7.906 m	2.35	13 dB

Tab. 3.2: Parameters of the Sardinia Radio Telescope.

The proposed optical solution is shown schematically in Fig. 3.6. Since it is preferable not to replace the HDPE lens, as it is an integral part of the receiver, we designed a new external elliptical mirror which results in an achromatic doublet compatible with SRT.

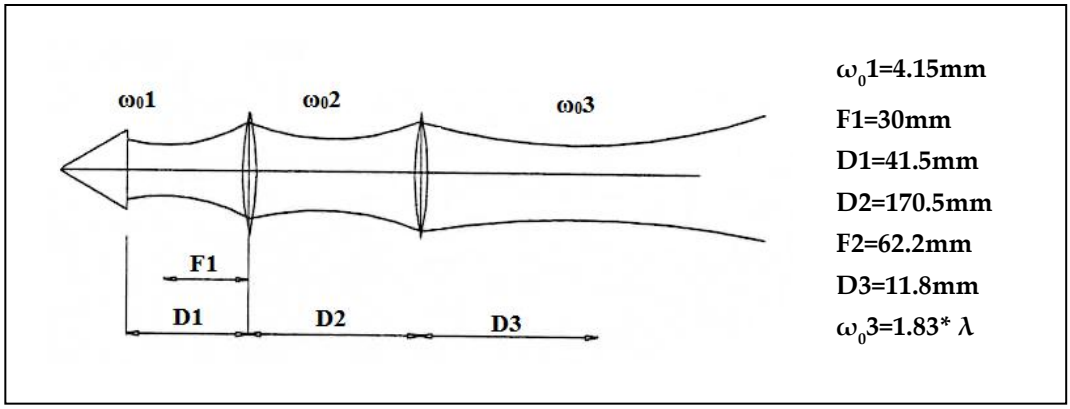

Fig. 3.6: Optical solution chosen.

An external elliptical mirror with focal length of 62.2 mm is placed at 170.5mm distance from the HDPE lens. The new achromatic doublet generates a beam waist of 1.83λ at 111.8mm of distance from the mirror.

3.2.2. Mechanical design

The receiver cabin on the SRT Gregorian focus is equipped with a rotating turret, which can host up to eight receivers, allowing to place automatically into focus the chosen instrument (Fig. 3.7). The Gregorian focus is located 2.5m above the cabin floor, close to the cabin ceiling. The available space and the configuration of the turret impose important mechanical constraints on the instrument to be installed inside it. In particular, the maximum available space for the receivers is

600mm orthogonal to the optical axis (in order to avoid touching the wall of the room).

Also, the mechanical configuration must take into account the constraints of the particular cryostat of the receiver: the ex-PdBI dual-channel receiver is based on an hybrid dewar (HDV10from Infrared Laboratories) with two cryogenic stages at 80 K and 15K provided by a commercial closed-cycle cold head (CTI-Cryodine, model 350 CP) and a 4.2 K stage provided by a 10 inch diameter high thermal conductivity plate in thermal contact with an inner vessel of liquid helium (7l in size). Because of the presence of liquid helium, to avoid spilling out of the cryogenic fluid when the Gregorian room rotates with the dish around its elevation axis, the vessel must be placed at an angle of 45° with respect to the vertical when the antenna looks at the zenith. In this configuration, when the dish points towards the horizon, the receiver vessel will be oriented at -45°; whatever the telescope elevation angle, the receiver will always be within ±45° from the vertical.

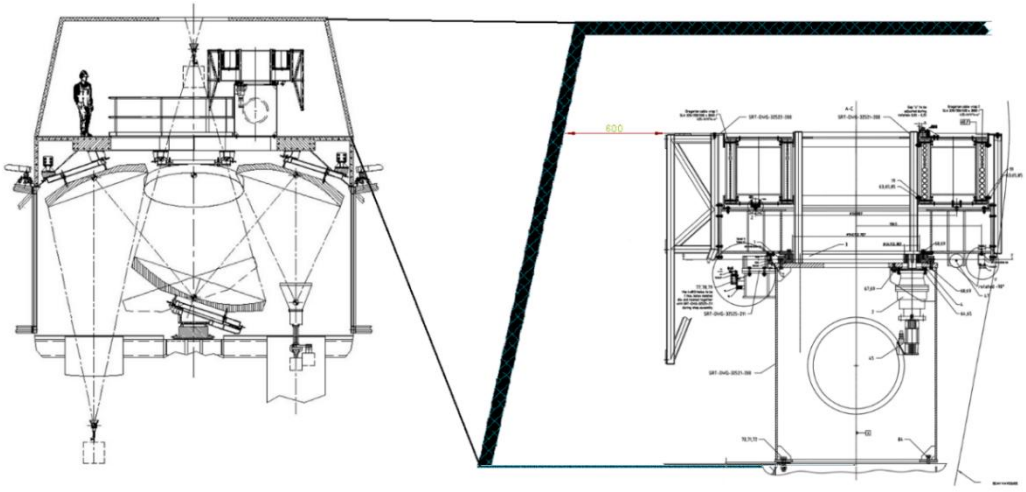

Fig. 3.7: View of the SRT receiver cabin showing the Gregorian Focus with the rotating turret (top left) and the beam waveguide focal points (bottom left). The details of the rotating turret on which the 3mm SIS receiver will be installed are illustrated on the inset (right).

Because of the 45° tilting, the maximum amount of the liquid helium that can be transferred to the reservoir is only 5 litres, instead of 7 litres. However, this will ensure that the 4.2K stage will be maintained at its nominal temperature for more than 15 days before a new helium refilling will be required. The first configuration we tried to implement foresaw the 3 mm receiver tilted at 45° inside the rotating turret. However, with such setup it would not be possible to switch the observations to the other receivers already installed in the turret (among which a K-band multibeam receiver) until the liquid helium vessel of the 3 mm receiver would be fully evaporated (when putting into focus another receiver, the liquid helium vessel of the 3 mm receiver would be in horizontal position for some elevation angles, and the helium would leak the cryostat). Though this constraint

limits the ‘frequency agility’ of the SRT, we tried to design a configuration that takes into account of this receiver position, as illustrated in Fig. 3.8.

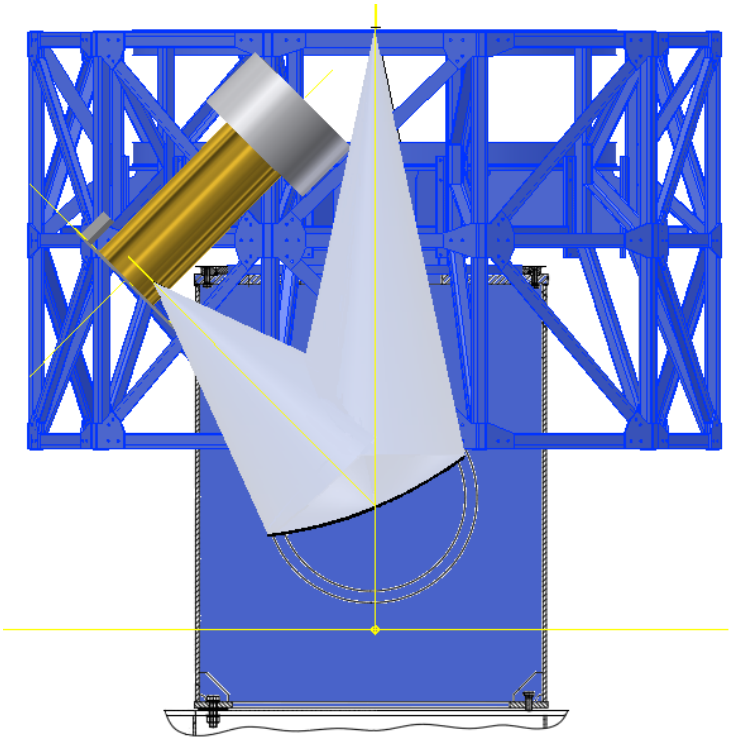

Fig. 3.8: Simulation of the mechanical configuration.

Unfortunately, this configuration is not suited to SRT for reasons of limited available space. In particular, the horn position in the lower left of the dewar, the receiver rotated at -45°from the vertical axis, and the Gregorian focus of the SRT located close to the ceiling and cabin walls, would require to use a big elliptical mirror, external to the receiver, to redirect the beam from SRT inside the ex-PdBI 3mm receiver horn. The total size of this system would exceed the available space.

Taking into account the aforementioned optical configuration and mechanical constraints, we are investigating a solution, which foresees to get rid of the liquid helium and use an additional close-cycle cryocooler capable to achieving the 4K physical temperature without requiring manipulation of cryogenic fluids (Fig. 3.9). The 4K stage cryocooler would operate in parallel to the existing CTI cryocooler and the receiver could be oriented in any direction, independently of the antenna pointing elevation angle. The chosen cold head, from Advanced Research Systems (ARS), model DE-204SF [54], has a 20K stage and a 4K stage delivering 8W and 0.2W of cooling power at respectively, 20K and 4K. A modification to the dewar is required to host the second cryocooler. The receiver would be placed in the upper part of the rotating turret, in correspondence to the Gregorian focus, so that the output beam waist of the external elliptical mirror and the beam waist of the SRT would coincide. We also designed a mechanical

support to place the hot and cold calibration loads at the correct distance (beam waist distance) from the 3 mm band receiver horn.

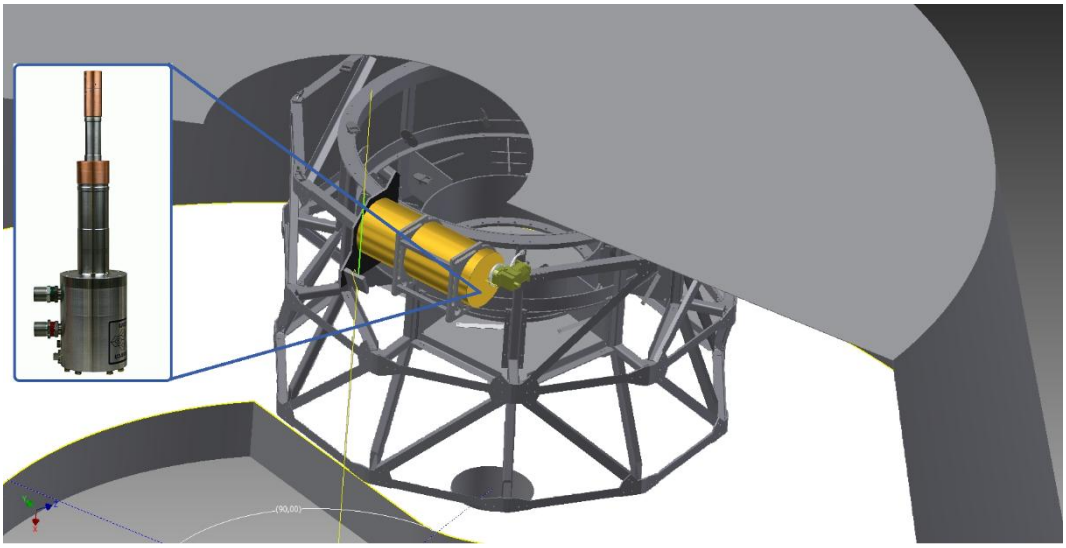

Fig. 3.9: Mechanical configuration chosen for antenna installation.

Currently, the INAF - Cagliari Astronomy Observatory laboratory is being equipped to carry out the modifications and following tests of the receiver before its installation on the antenna.

Chapter 4: Feed horn for S-band multi-beam of the Sardinia Radio Telescope

In 2013, the Sardinian Regional Government, the European Union (EU) and the Italian National Institute for Astrophysics (INAF) funded a fundamental research project with the target to enhance the knowledge of some astrophysical problems, which have greater impact on the understanding of the physical laws that govern the universe by using a state-of-the-art facility as SRT. In order to fulfil the aforementioned scientific target, the project also includes the design, fabrication and installation of a state-of-the-art multi-beam receiver operating at the frequency band of interest: 2.3 GHz – 4.3GHz (S radio astronomy band).

In this chapter, the design of a new wideband quadruple-ridged horn antenna for the multifeed S-band receiver of the Sardinia Radio Telescope is presented.

4.1.Key requirements of radio astronomical feeds

Radio telescopes are reflector antennas. The most simple reflector antenna consists of a parabolic or shaped reflector with a small feed placed in its focus. The size of reflector is much larger of the wavelength while the size of feed is smaller than wavelength. In this way, the reflector is in the far field of the feed and this simplifies analysis.

Two techniques can be used to analyse the performance of the reflector antennas: current distribution method based on physical optics approximation and aperture distribution method based on geometrical optics technique [27]. The first method provides an accurate calculation of the field in the main lobe of the reflector antenna but it is quite complex. The second method provides less accurate results but it is valid both in the main lobe area and in the secondary lobes area. The advantage of this method is that it considers the reflector antennas as aperture antennas characterized by an aperture plane perpendicular to the axis of the reflector. The peculiar characteristic of the reflector antennas is that a spherical wave generated by a point source placed in the focus of the reflector is reflected into a plane wave propagating in any plane orthogonal to its axis (Fig. 4.1). This

surface is an equi-phase plane for the various rays: all the rays that arrive on this plane are in phase each other, and thus constitute the phase front of a plane wave.

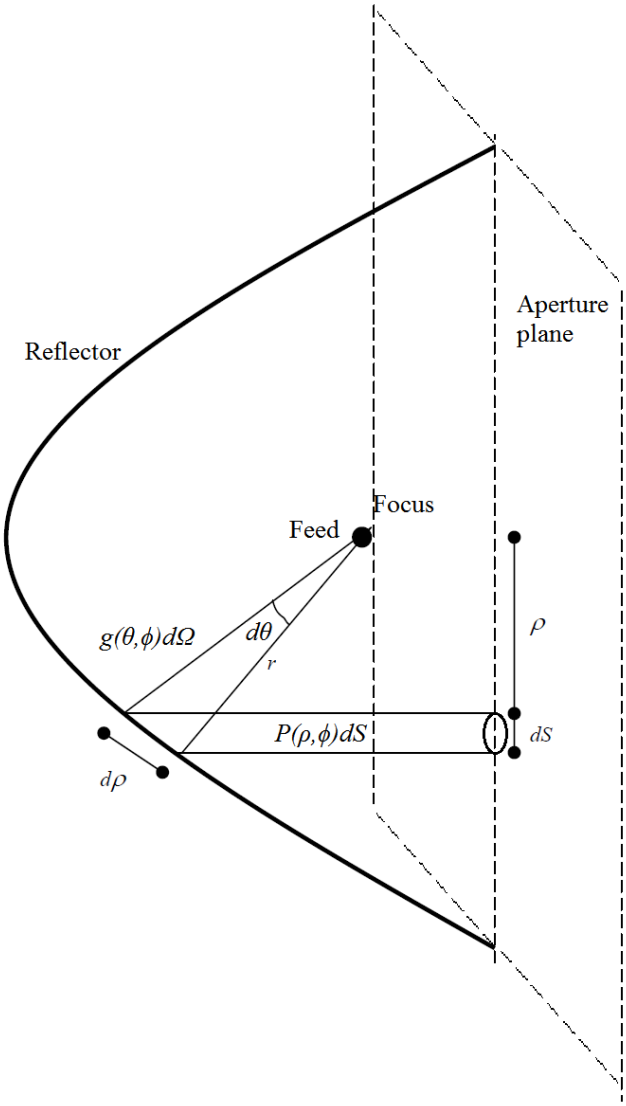

Fig.4.1: Signal's path of a reflector antenna system.

Therefore, the reflected field over the aperture can be written as:

$$P(\rho,\varphi) = g(\vartheta,\varphi) * \frac{1}{r^2} \qquad [4.1]$$

Namely, the field depends both on the diagram of the feed irradiation, $g(\vartheta,\phi)$, and on the geometric factors, r^2.

The directivity is a very important figure of merit in the design of antennas and can be written as:

$$D = \frac{4\pi}{\lambda^2} * A_{eff} \qquad [4.2]$$

where A_{eff} is the effective area of an antenna and it is defined as the area of a uniformly illuminated aperture that yields the same gain G. When the effective area is equal to physical area, the directivity, D_M, or directivity gain, G_M, reaches the maximum value:

$$D_M = G_M = \frac{4\pi}{\lambda^2} * A_{phys} \quad [4.3]$$

The aperture efficiency, or antenna efficiency, is then defined as the ratio of an antenna's effective area to its physical area that is a circle area for a paraboloid:

$$\epsilon_{AP} = \frac{A_{eff}}{A_{phys}} = \frac{D}{D_M} = \frac{A_{eff}}{\pi R^2} \quad [4.4]$$

In general, the aperture efficiency of a reflector antenna is the product of the different loss factors [27]:

- **Spillover efficiency** ϵ_s: it is the fraction of the total power that is radiates by the feed, intercepted, and collimated by the reflecting surface, it can be written as:

  $$\epsilon_s = \frac{D_f}{4\pi} \int_0^{2\pi} \int_0^{\Psi/2} g(\theta, \varphi) d\Omega \quad [4.5]$$

  where D_f is the directivity of feed and Ψ is the total aperture angle of the reflector;
- **Taper efficiency** ϵ_t: it is the uniformity of the amplitude distribution of the feed pattern over the surface of the reflector;
- **Phase efficiency** ϵ_p: it is phase uniformity of the field over the aperture plane;
- **Polarization efficiency** ϵ_x: it is polarization uniformity of the field over the aperture plane and measure the peak of cross-polarization level in the ϕ=45° plane;
- **Blockage efficiency** ϵ_b: it is the fraction of total power that is blocked by feed apparatus;
- **Random error efficiency** ϵ_r over the reflector surface.

Thus, we can write the aperture efficiency as:

$$\epsilon_{AP} = \epsilon_s \epsilon_t \epsilon_p \epsilon_x \epsilon_b \epsilon_r \quad [4.6]$$

The aperture efficiency ϵ_{AP} is always smaller than 1 because of all of aforementioned loss factors. It is possible to increase ϵ_{AP} if the reflector antenna has a small total aperture angle Ψ and high edge illumination but it is exactly what reduces the spillover efficiency ϵ_s. Therefore, it need found a trade-off between illumination and spillover. The theoretical maximum aperture efficiency of a symmetric parabolic reflector antenna is almost 80% attained at approximately -10 dB feed edge taper. The realized aperture efficiency will necessarily be lower.

In this context, the design of feed is fundamental. In fact, some of the parameters of interest in the design of a reflector antenna such as gain, spillover, first and far-out sidelobe levels, cross-polarization level are strongly dependent on the feed antenna performance and are most commonly quantified via aperture efficiency.

Spillover and non-uniform amplitude distribution losses are the two main factors that contribute to the aperture efficiency and are two loss factors that depend primarily on the feed pattern.

The design of feed, together with the design of the all receiver chain, has the aim to maximize the gain and minimize system noise temperature, both of which increase telescope's sensitivity.

The guidelines to design practical feeds to be used in radio astronomy are:

- High aperture efficiency;
- Constant beam width;
- Circularly symmetric radiation pattern;
- Small phase center variation;
- Low cross-polarization;
- Good input return loss to reduce impact on T_{sys}.

4.1.1. State of art in wideband feeds

In the previous section, we are listed the specifications that an optimal feed for reflector antennas must have. Typically, the feeds used in radio astronomy are waveguide horns because fulfil all specification aforementioned. In fact, they can produce radiation patterns having extremely good axial symmetry, relatively constant beamwidths as a function of frequency, high beam efficiency, low cross-polarization levels, very low sidelobes and back lobes, good return loss, and the same phase centers in all cut planes containing the antenna's boresight [27-30]. Waveguide horns for radio astronomy applications are typically realized using a rectangular or a circular waveguide, which flares into a wider open-end radiating termination, using different configurations and shapes. In most of the designs present in the literature, a linear corrugation profile with slot depths greater than a quarter of a wavelength at the low end of the frequency band and less than a half wavelength at the high end was used to obtain a maximum relative bandwidth of 2:1 [30-33]. To increase the frequency bandwidth of horns, more-complex designs have also been suggested in the literature.

However, standard waveguide horns are usually too directional to effectively illuminate such a large reflector as the 64-meter primary reflector of SRT, with operating frequency band is of the order of 40-50%. Moreover, the radiating aperture of a standard waveguide horn could be too large to be employed in a multi-feed system, especially in our case, wherein space and weight constraints are critical.

In the 40s, Cohn [34] identifies the capabilities of the ridges in the waveguide to broaden the operating band lowering the dominant mode cutoff frequency by nearly a factor of four. Subsequently, [35-36] expanded on his studies, which they provided in addition to the transverse-resonance methods to calculate cutoff frequencies, the parametric studies of the cutoff frequencies and attenuation, and the analysis to include the complete eigenvalue spectrum of these structures. Therefore, the advantage of a wide bandwidth and low impedance compatible with coaxial cables, due to a low cutoff frequency, has encouraged the development of these structures that have many applications in microwave and antenna systems.

Two different configurations of ridged waveguide is possible to design, depending on whether they have two or four ridges loaded symmetrically in a square, diagonal, circular or shaped waveguides:

- Double-ridged waveguide or horn;
- Quad-ridged waveguide or horn.

The first configuration is widely used in antenna and radar systems but have the limitation to support only the single linear polarization. In the applications where dual or circular polarizations are fundamental, the quad-ridged configuration is used.

Furthermore, the quad-ridged waveguides have been analysed to determine its modal characteristics. [37-39] determined the characteristics of square, circular and diagonal quadruple-ridged waveguides, including cutoff frequencies, attenuation, impedance and modal field distributions. The analysis of [39] shows that the fundamental mode in a quadruple-ridged waveguide has a cutoff frequency very close to that of the second-lowest mode. Thus, the natural single mode bandwidth is very small respect to dual-ridged configuration. However, if the structure has both x- and y- symmetry, the second-lowest mode is effectively suppressed or not excited, and a very wide bandwidth (6:l) can be achieved.

The aforementioned papers on quad-ridged waveguides only assign the guidelines on the first few eigenmodes and, therefore, the design of these structures lacks of a theoretical or empirical analysis. [40-41] provide some horn profiles that can be used to design the ridge and sidewall profiles.

Different configurations of quadruple-ridged horn antennas for radio astronomy applications are available in the literature, as proposed in [3, 42-45] based on circular waveguide or as proposed in [46-48] based on square waveguide.

However, none of these works is suitable for our application. In fact, the physical dimension of the horn radiating aperture is too large for application in the multifeed system of SRT. Moreover, those solutions are found not suitable to illuminate the primary reflector of SRT, which has an F_1/D of 0.33.

In the next section, the project for the new multifeed receiver to install in the Sardinia Radio Telescope is presented.

4.2.S-band multi-feed receiver[52]

New research project, entitled “An attack on open questions of modern physics with the development of advanced technologies”, of the radio astronomy community of Astronomical Observatory of Cagliari (OAC) was funded. The purpose of this proposal is to investigate some unsolved questions about the origin and evolution of the Universe and better understand the laws that govern it, through the development of high-technology equipment, which will allow unprecedented observations. In particular, main scientific aims of this project are:

- Pulsar observations (survey and monitoring) in the galactic center region; evaluation of the pulsar dispersion measure variations;
- Simultaneous observations of pulsars within the Large European Array for Pulsars (LEAP) for gravitational wave detection;
- Mapping and characterization of the radio spectra of galactic supernova remnants;
- Study of the radio polarization of a sample of halos in nearby galactic clusters.

The observational strategy has as common denominator, the development of a new generation receiver to be installed in the Sardinia Radio Telescope. The frequency band chosen by astrophysical researches for the aforementioned research is the S-band: 2 – 4 GHz. Furthermore, to efficiently perform these astronomical surveys, the new receiver must have the following characteristics:

- maximum available instantaneous bandwidth, as large as possible field of view (FOV);
- very low system temperature to maximize the radio telescope sensitivity;
- double circular polarization;
- very low cross-polarization level to better distinguish the radio source signal polarization.

Therefore, the new receiver must take into account the scientific requirements, the SRT electromagnetic and mechanical constraints, and the radio signal interference (RFI) scenario around the SRT site [52].

A preliminary RFI measurement campaign at the frequency range between 2 and 5 GHz has shown the presence of the UMTS and Wi-Fi signals around at 2.1 GHz and 2.44 GHz respectively with the high power level, especially for UMTS signal.

According to all the considerations aforementioned, it was decided that the project for the new receiver provides a bandwidth of 2 GHz, between 2.3GHz and 4.3GHz. To satisfy the prerequisite of field of view (FOV) as large as possible,

the receiver is equipped with the maximum possible number of feeds on a focal plane array: seven feeds. Furthermore, the instantaneous bandwidth of 2 GHz allows us to take advantage of the new generation digital backend [49-50] that can process an intermediate frequency (IF) between 0.1-2.1 GHz. In this way, the sky frequency RF is down-converted to baseband using only two fixed local oscillators.

The focal position chosen for this receiver (Fig. 4.2) is the primary focus of the SRT because the F_1/D of primary focus of the radio telescope is smaller than the F/D of other focal positions (F_1/D=0.33, F_2/D=2.34, F_3/D=1.37, F_4/D=2.81)[51]. This allow us to keep small enough the size of multi-feed and, at the same time, this allow us to have the maximum number possible of feeds.

Since the S-band receiver is intended to be mounted in the primary focus of SRT, a suitable edge taper must be provided by the feed to achieve the optimal illumination of the 64-meter primary parabolic surface of SRT. Moreover, in our case, the single feed is a part of a multifeed configuration and, therefore, the feed design must also take into account the limited room available in the focal cabin of SRT, and the load constraints of the primary focus positioner (Fig. 4.2). Consequently, each single feed horn of the "multifeed array" must be compact, light, and with a reduced radiating aperture.

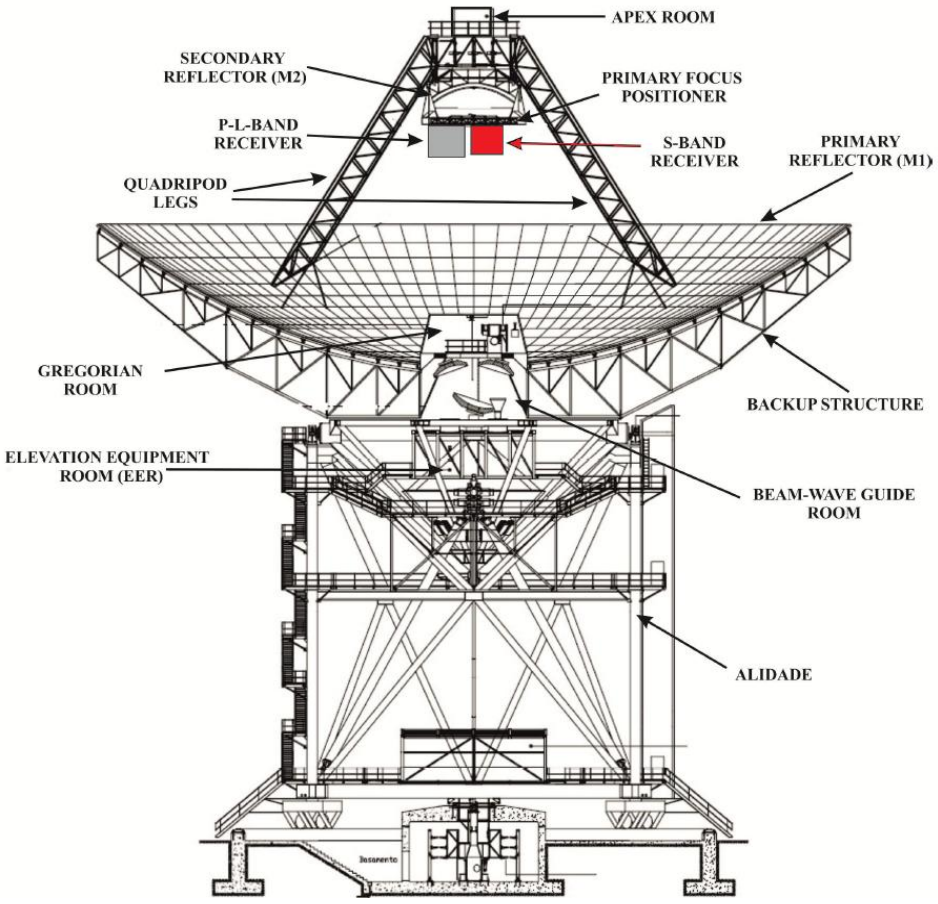

Fig. 4.2: Schematics of SRT: the position of S-band multi-feed is highlighted.

The preliminary electromagnetic analysis was carried out to estimate the specifications of single feed that determinate the optimal SRT aperture efficiency. The 3D electromagnetic analysis software GRASP was used. In the GRASP model of SRT (Fig. 4.3), we have taken into account the blocking effects of the subreflector, with an 8 m diameter hole centered in the main reflector, and the quadrupod structure (struts). To simulate the coupling between the SRT and the radiation pattern of a feed, we are chosen an ideal point-like Gaussian feed. It was simulated at 3.3 GHz by varying the feed edge taper from -7 to -19 dB with a return loss equal to -5, -15, and -20 dB. The estimated radio telescope sensitivity was obtained by means the evaluation of the system equivalent flux density (SEFD), which is defined as the ratio between the system temperature (T_{sys}) and the antenna gain (G) at a given frequency. The result are shown in table 4.1 [Table 1 of 52].

Frequency [GHz]	T_{RIC}^{*} [K]	T_B (0^0) [K]		Edge Tapet [dB @74°]	SEFD [J_Y] (RL=5dB)	SEFD [J_Y] (RL=15dB)	SEFD [J_Y] (RL=20dB)
3.3	18	5		-7	142.53	100.38	98.21
3.3	18	5		-10	107.57	75.95	74.29
3.3	18	5		-13	102.32	72.24	70.67
3.3	18	5		-16	108.80	76.82	75.15
3.3	18	5		-19	129.80	91.75	89.65

Tab. 4.1: SRT sensitivity in term of SEFD at 3.3 GHz at the zenith [52].

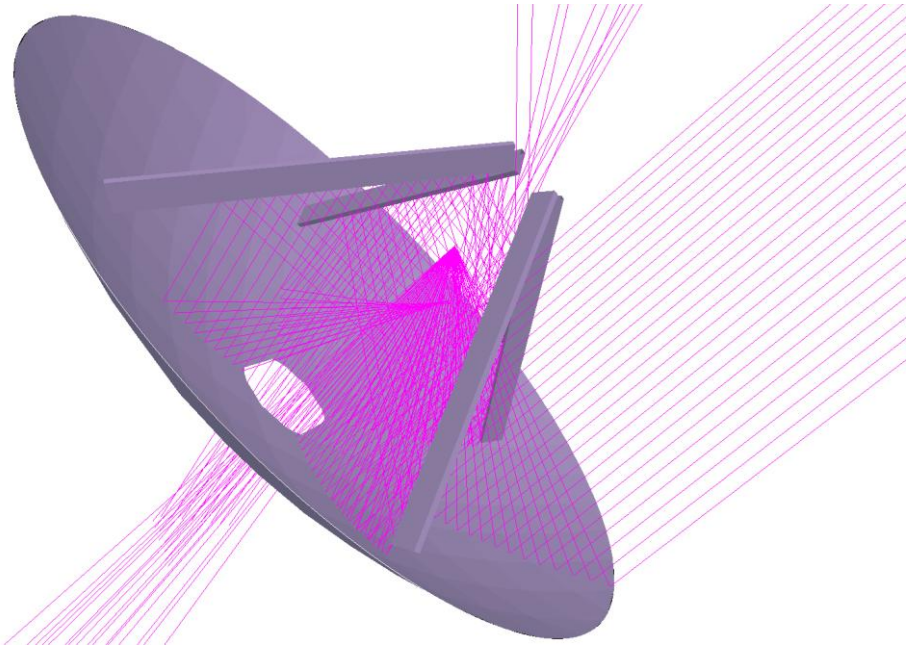

Fig. 4.3: Grasp model of the SRT used.

By comparing the last three columns in Table 4.1, the best antenna sensitivity turns out to be with an edge taper of -13 dBm with a RL greater than 20 dB.

The specifications required for the single feed design resulting from electromagnetic analysis aforementioned are:

- Bandwidth: 2.3 GHz- 4.3 GHz (60% of relative bandwidth);
- Return loss > 20dB;
- Insertion loss < 0.2 dB;
- Cross polarization < -35dB;
- Edge taper @74° (3.3 GHz) -13dB;
- Diameter feed < 91mm ~1λ at 3.3GHz.

The last one specification is fundamental to design the multi-beam array. By using the same SRT GRASP model, we are estimated the best aperture efficiency by changing the feed position from the focal point to another point on the SRT focal plane (Tab. 4.2).

Position [mm]	T_{RIC}^{*} [K]	T_B (0^0) [K]	RL [dB]	Aperture Efficiency [%]	SEFD (Tsys/G) [J_Y]
0 mm	18	5	20	66,2	70.67
100 mm	18	5	20	56,57	82.75

Tab. 4.2: Aperture efficiency of SRT simulated by GRASP [Tab.3 of 52].

The values were chosen equal to 0, when the feed was in F1, and equal to 100 mm, when the feed was placed on the position of the FPA configuration considered. The value equal to 100 mm (Fig. 4.4) was obtained taking into to account the Half Power Beam Width (HPBW), defined as 1.22*λ/D where λ is the wavelength at central frequency and D the M1 diameter, and the minimum distance between two main beams on the sky, equal to 982 arcsec, that fulfills the Nyquist sampling interval (*dmin*/F1> λ/D). Moreover, this value takes into account of the thickness of the feed waveguide external edge, about 3 mm, and the distance between the border of two feeds: equal to 3 mm.

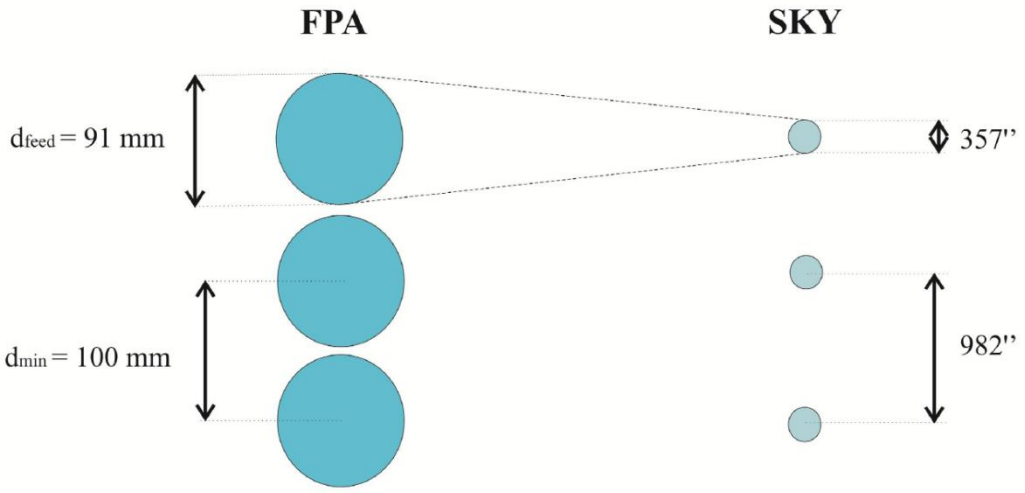

Fig. 4.4: Size and distance between FPA feeds (mm) related to HPBW and distance between two main beams on the sky (arcsec) [Fig.5 of 52].

The optimal focal plane array configuration was also estimated to produce the better mapping of an extended radio astronomical source: it is the Hexagon Pattern.

In the follow section, the design a waveguide feed for the S-band multifeed receiver of the Sardinia Radio Telescope (SRT) is presented. The performances of the feed designed are in good agreement with the aforementioned specifications.

4.2.1. Design

The design specifications, presented in the previous section, are guidelines used to design the new device. The design and optimization of the waveguide feed horn have been performed using the FEM commercial software Ansys HFSS [20].

Initially, the design of the new feed was focused on a device with a simple configuration and easy to manufacture. Briefly, we describe two configurations that have given the best results.

The first configuration consists of a circular waveguide with two matching metallic cylindrical irises arranged along the optical axis of the feed to improve the operating bandwidth, Fig. 4.5. The diameter of feed is D=90.9mm with 270mm length. The inner diameter of two irises is 86.3 mm with a distance of L_{I1}=81.1 mm and L_{I2}=35.6 mm from the feed aperture.

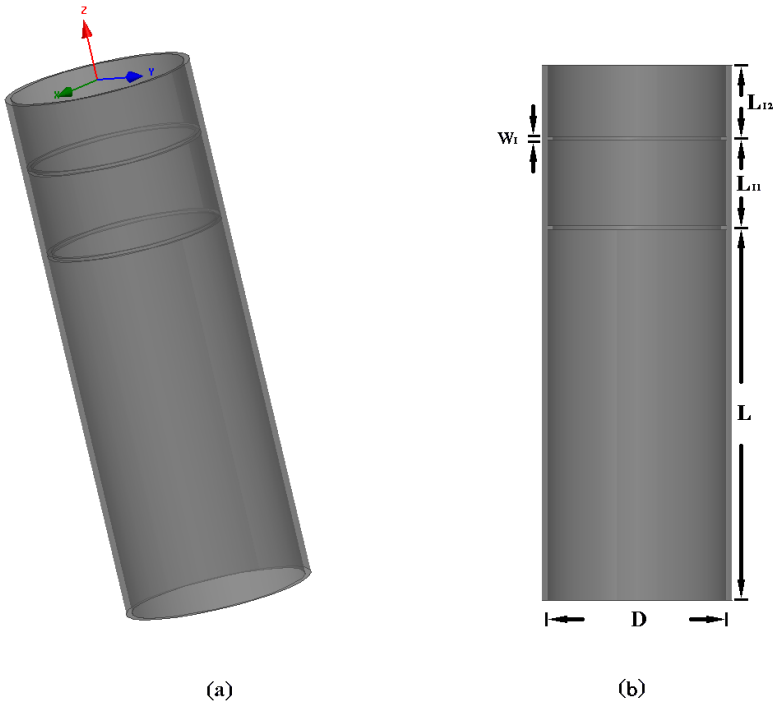

Fig. 4.5: Geometry of the first horn antenna: (a) 3D view; (b) sectional view.

Figs. 4.6, 4.7 and 4.8 show the performances of the feed, respectively, the return loss and normalized gain in the ϕ=45° at 2.3 GHz, 3.3 GHZ and 4.3 GHz.

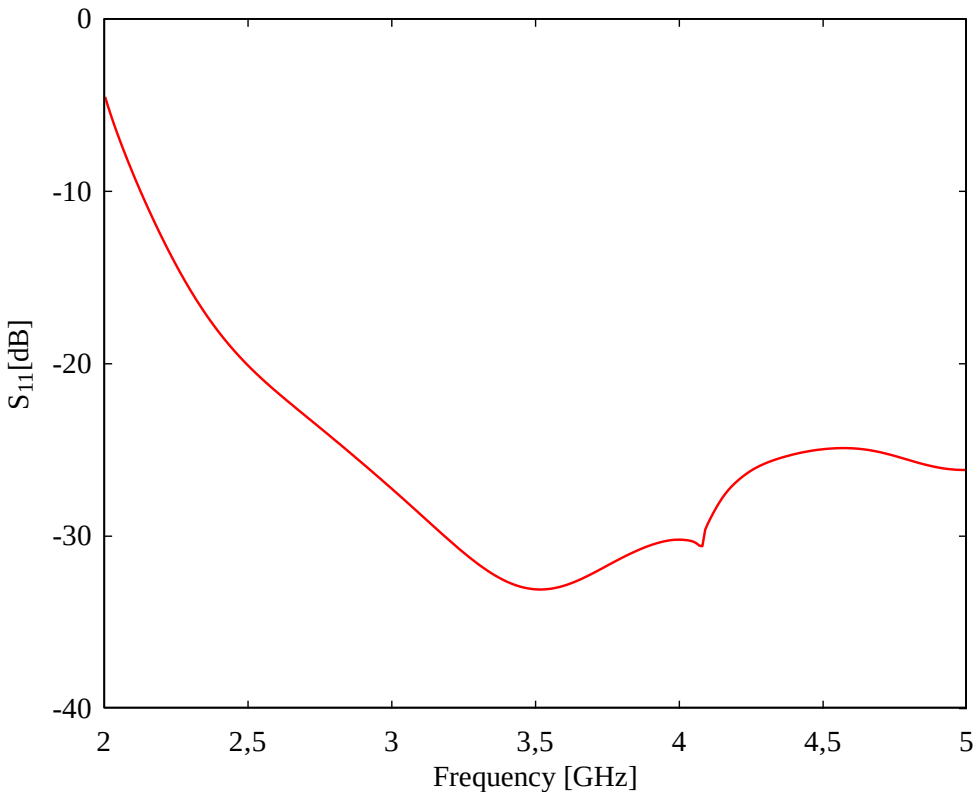

Fig. 4.6: Simulated reflection coefficient of the feed.

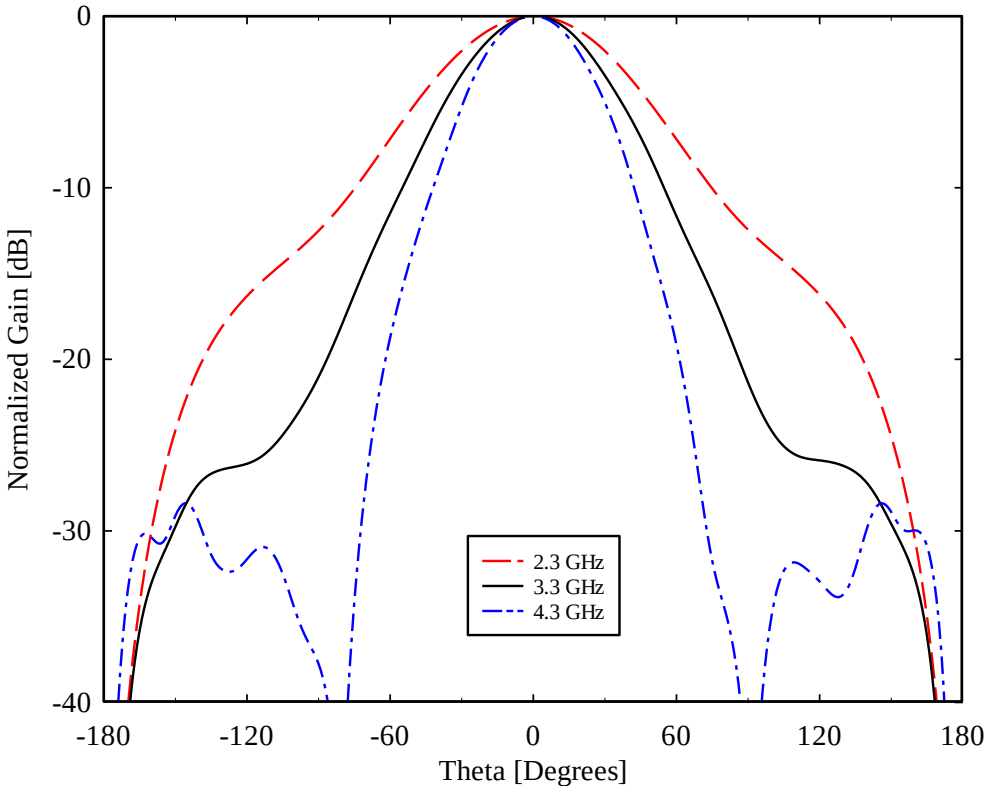

Fig. 4.7: Normalized radiation patterns of the feed at 2.3 GHz, 3.3GHz and 4.3 GHz in the ϕ = 45° plane.

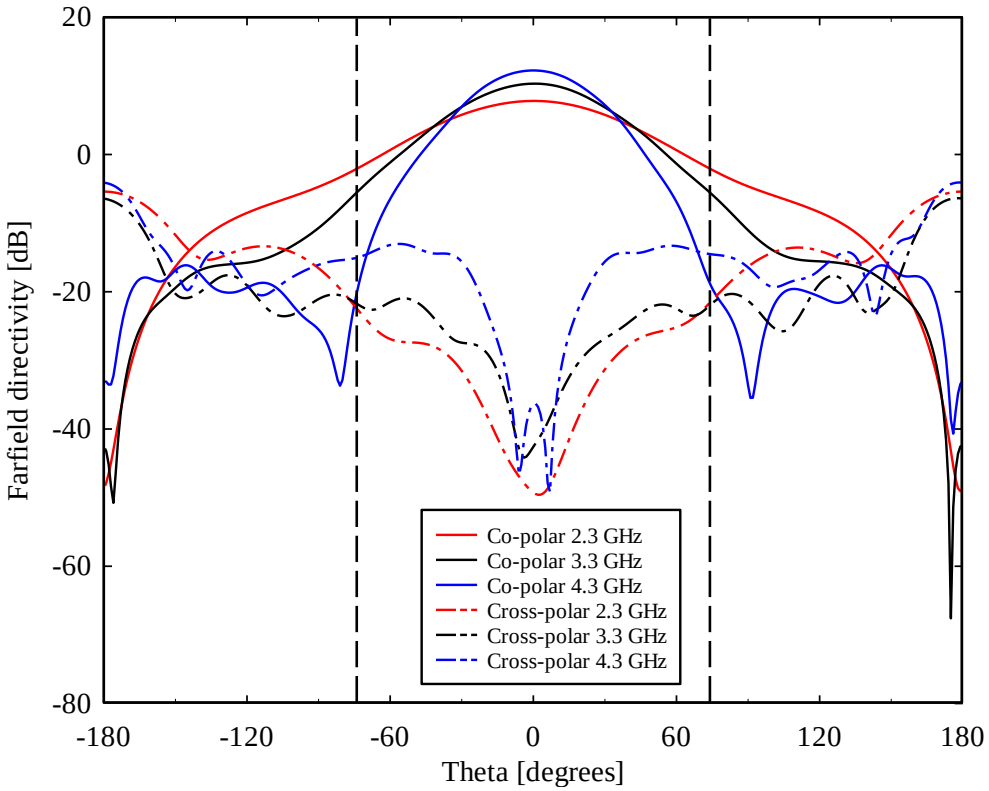

Fig. 4.8: Radiation patterns of the feed at 2.3 GHz, 3.3GHz and 4.3 GHz in the ϕ = 45° plane.

Although the return loss of the feed is acceptable, it is below -15dB in the band of interest, the radiation pattern is not acceptable for the SRT requirements. Fig. 4.7 highlights this effect showing the co-polarization and cross-polarization components of the far field directivity. In fact, the radiation pattern is too directive, especially at 4.3 GHz, and does not meet specifications of -13 dB of edge taper at 74° at 3.3 GHz. Moreover, the reference lines at ±74° highlight that the cross-polarization level at 4.3 GHz is too high for the SRT requirements.

The second configuration consist of a circular waveguide with variable inner diameter, Fig. 4.9. The inner diameter ranges from the maximum value of D_I=90.9 mm at the back-short to the minimum D_O=80 mm at the feed's aperture. In the middle, a conical section matches those external parts. The length of each section is respectively L=270 mm, L_{I1}=54.5 mm and L_{I2}=102 mm.

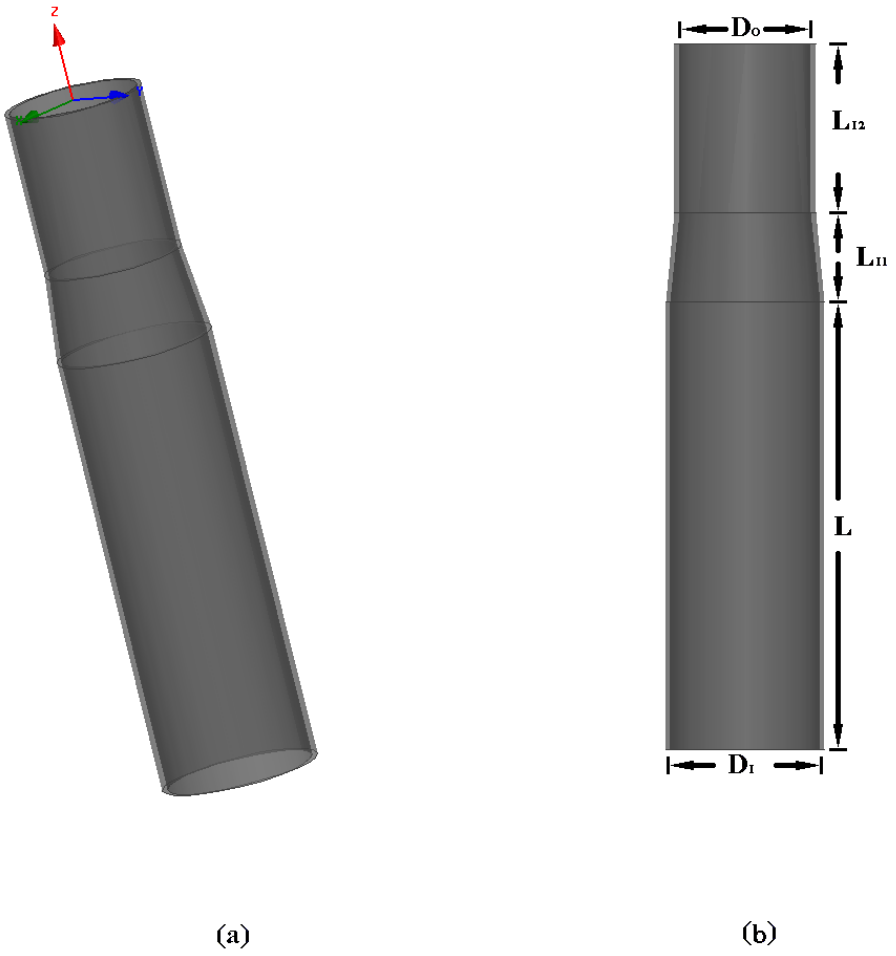

Fig. 4.9: Geometry of the second horn antenna: (a) 3D view; (b) sectional view.

Figs. 4.10, 4.11 and 4.12 show the performances of the feed, respectively, the return loss and normalized gain in the ϕ=45° at 2.3 GHz, 3.3 GHz and 4.3 GHz. In this case, the radiation pattern meets the feed specifications, but the return loss is RL=-4dB at the lower frequency, 2.3 GHz, is not acceptable. The cut-off frequency of the fundamental mode, equal to 1.9 GHz, is too close at the starting frequency of the receiver operating bandwidth and it conditions the return loss.

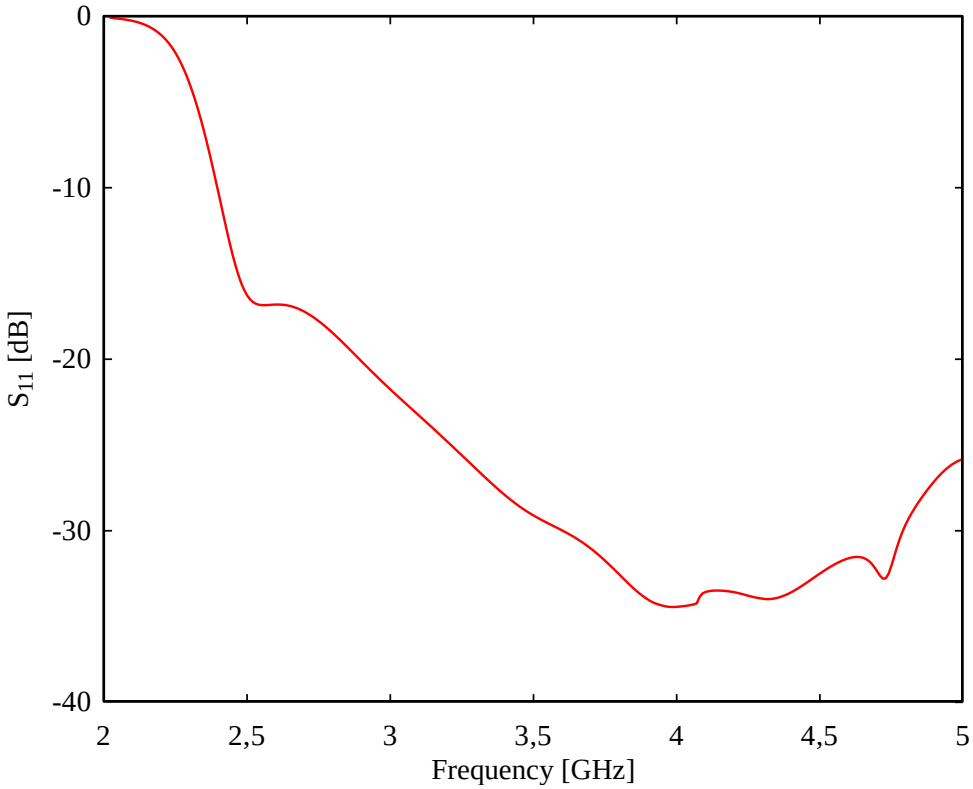

Fig. 4.10: Simulated reflection coefficient of the feed.

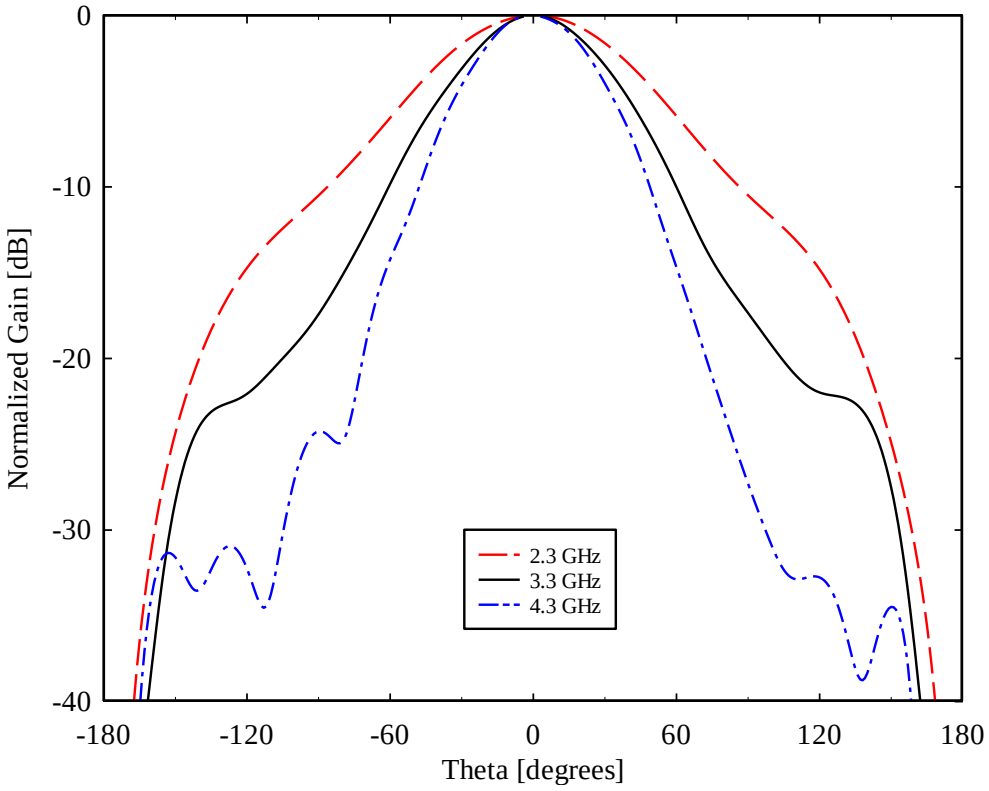

Fig. 4.11: Normalized radiation patterns of the feed at 2.3 GHz, 3.3GHz and 4.3 GHz in the ϕ = 45° plane.

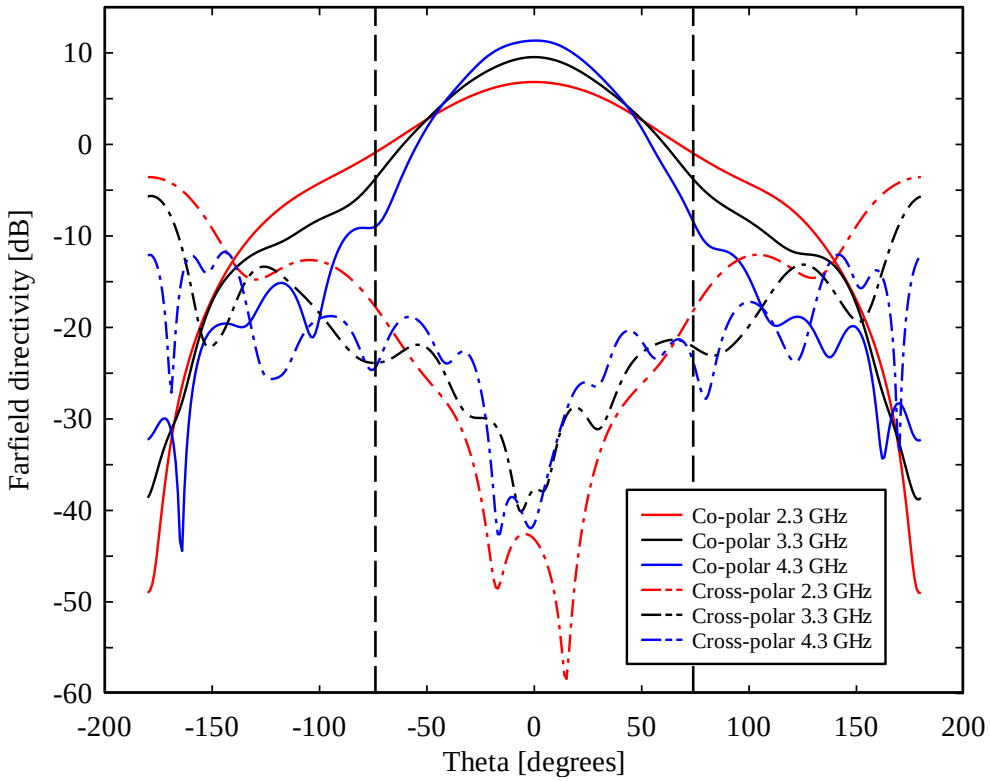

Fig. 4.12: Radiation patterns of the feed at 2.3 GHz, 3.3GHz and 4.3 GHz in the ϕ = 45° plane.

In addition to not optimal performances, these previous configuration of feeds are too long for SRT space requirements. In fact, the maximum space available for the receiver in the Primary Focus Positioner is a cube of 1 m on each side. The receiver design provides that the elements of the receiver chain inside the dewar must be arranged as in Fig 4.13.

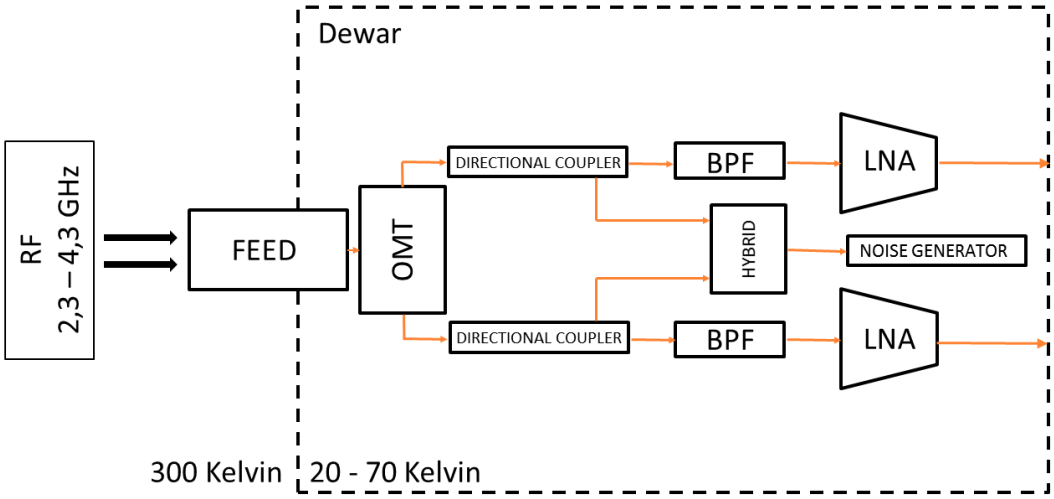

Fig. 4.13: Schematics of single receiver chain of S-band multifeed receiver

For this reason, the space available for the feed, if it is possible, must be less than 350mm. The other devices show in the Fig. 4.13 and the mechanical structure of the receiver with heat shields, vacuum windows, etc. occupy the remaining space.

In order to meet the design specification of the feed system, both on the bandwidth and on the required edge taper, keeping a compact and light realization, and aiming to minimize the waveguide horn transverse section, we have decided to design a new configuration based on the ridged circular waveguide [34-40].

The geometry of the proposed feed is shown in Fig. 4.14. It essentially consists of a truncated circular waveguide with four ridges of variable height inside. In the design and optimization of this configuration, we can identify three parts:

- a circular waveguide of diameter D_I;
- four ridges with a sinusoidal profile;
- the open-end radiating termination.

Each one of these parts must be accurately designed to comply with the required specifications, which are reported in the previous section.

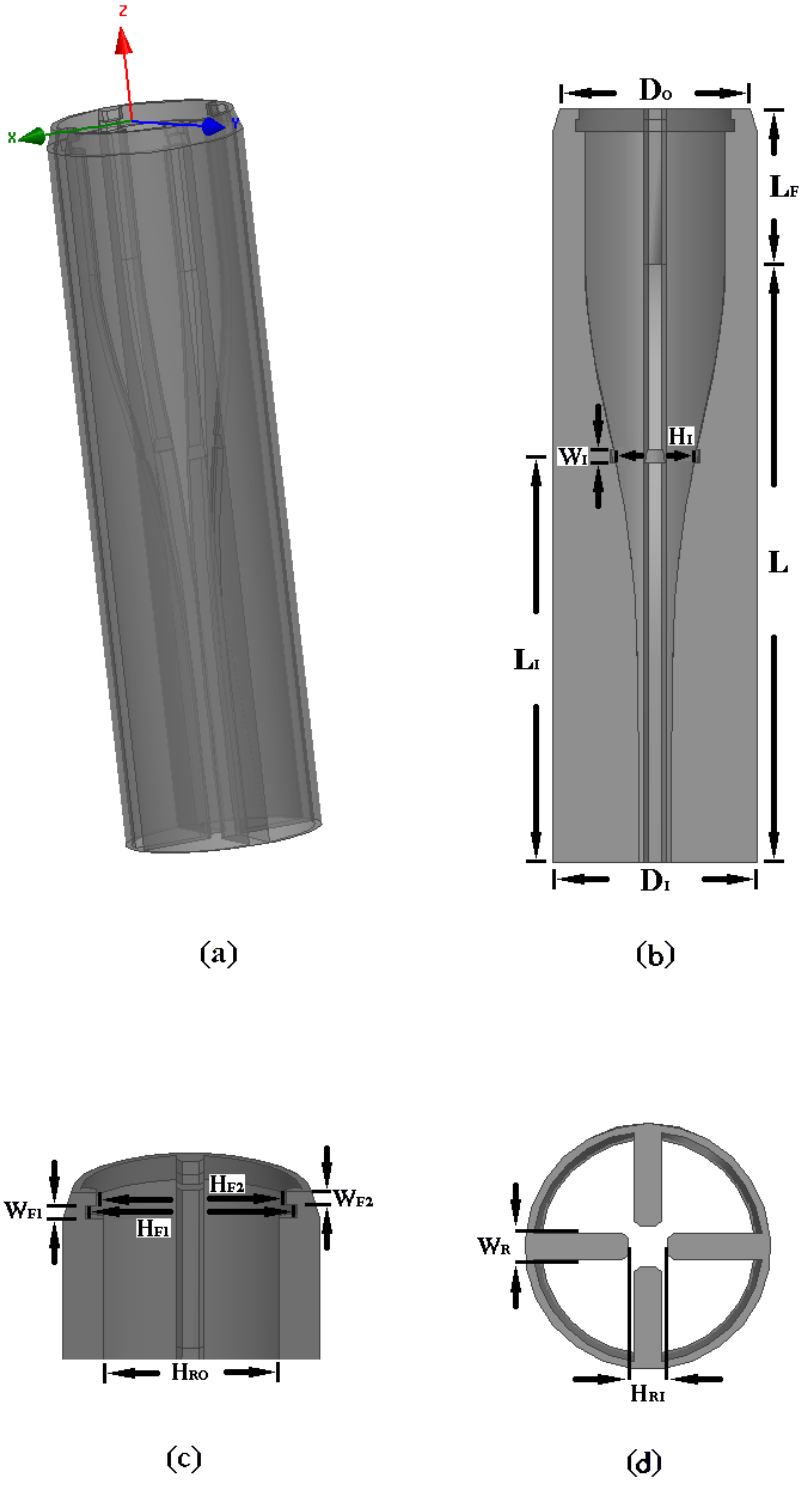

Fig. 4.14: Geometry of the proposed quadruple-ridge horn antenna: (a) 3D view; (b) sectional view; (c) detailed view of radiating aperture; (d) view from the bottom looking up.

The circular waveguide diameter D_I has been selected equal to 86 mm, the initial dimensions of the ridges, H_{RI} and W_R in Fig. 4.14d has been selected equal to 12.9 mm. These values are dictated by the formulas used to study the characteristics of a ridged waveguide in [39-40]. In Fig. 4.15 are reported the plots of the parametric design curves of a quadruple-ridged waveguide that to show the dependence of cutoff frequency and waveguide impedance on the ridge dimensions.

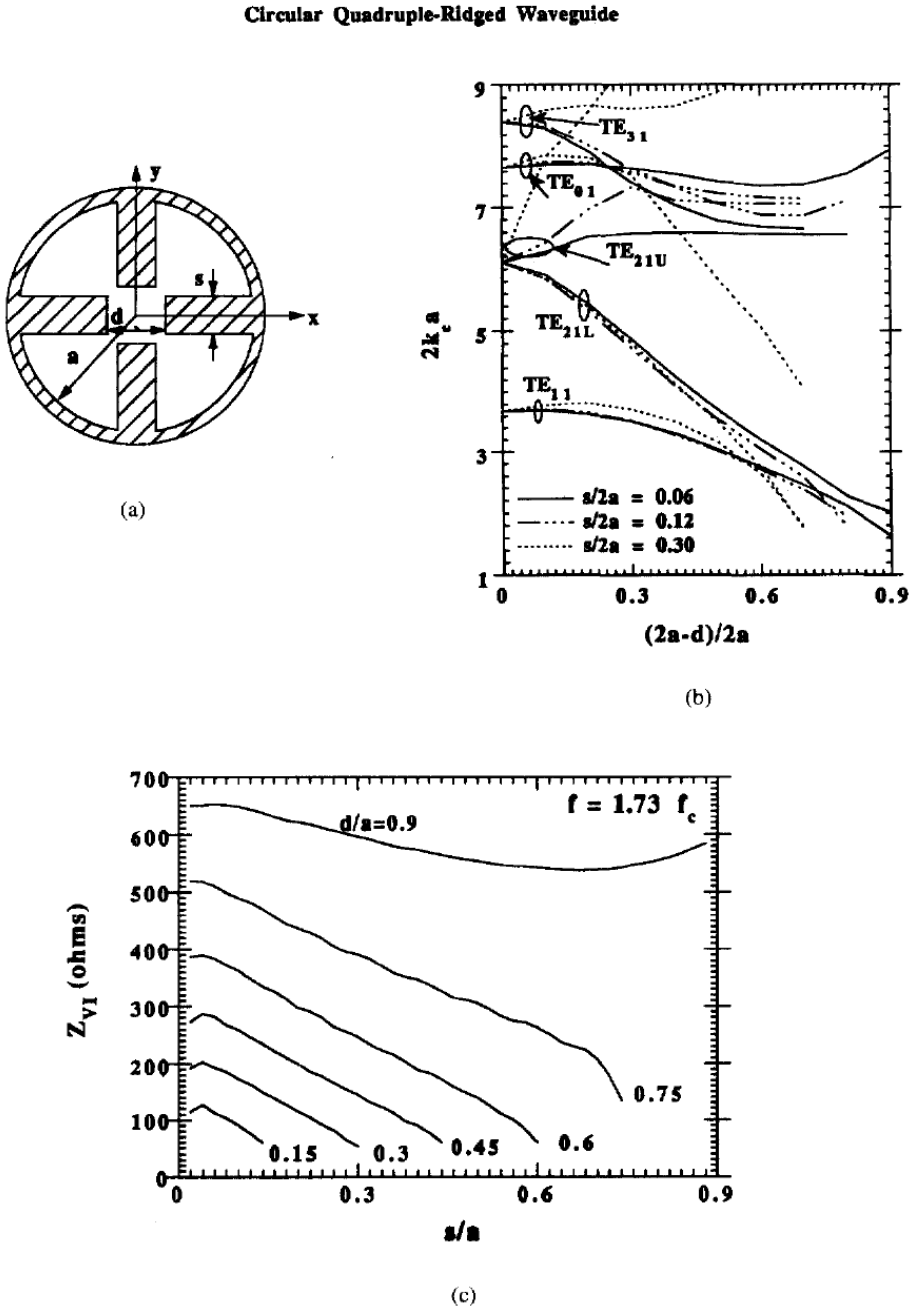

Fig. 4.15: Geometry of typical circular quadruple-ridged waveguides (a), normalized cutoff wave numbers, versus the ridge geometry (b), voltage-current impedance versus the ridge thickness (c) [40].

The ridge dimensions chosen, together with the waveguide diameter, guarantee that the position of cut-off frequency of the fundamental mode of the ridged circular waveguide is well below the starting frequency of the receiver operating bandwidth, which is equal to 0.9 GHz in our case (Fig. 4.16), and the impedance at the input port of the ridged waveguide is 50 Ω. These values are the same used by the architecture of the circular Ortho Mode Transducer, which is realized using the same quadruple-ridged configuration [52], and connects to the input port of the feed.

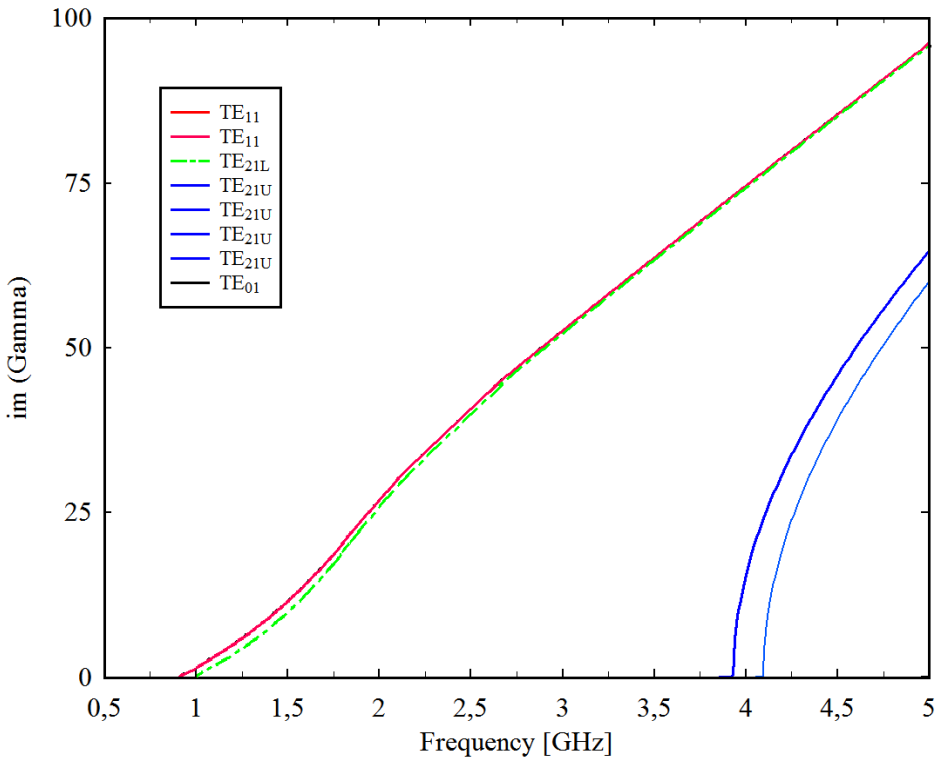

Fig. 4.16: Positions of cut-off frequency of the fundamental mode and first superior modes of proposed feed.

The choice of the profile of the ridges, which can be observed in Fig. 4.14b, is a key point in the antenna design since it must be suitably selected both to match the 50 Ω input impedance of the ridged waveguide to the free space impedance. Moreover, the ridge profile contributes to have a circular radiation pattern with a constant beamwidth. To obtain a constant beam width from a circular aperture, the aperture field distribution must shrink in area as frequency is increased. The ridge profile produces a difference in path lengths along the horn's longitudinal axis that introduces an additional phase to fields near the aperture rim. The additional phase increases as frequency increases and this produces a reduced aperture area with uniform phase [3].

Different profile options are available to the feed-horn designer, and have been investigated in [41]. The most commonly used profiles in the literature are the exponential and elliptical profiles for both ridges and sidewall.

For our application, we have found that the best results are achieved using the sinusoidal profile (see Fig. 4.14), which is described by the following equation:

$$a(z) = a_i + (a_o - a_i)\left[(1 - A)\frac{z}{L} + A\sin^p\left(\frac{\pi z}{2L}\right)\right] \qquad [4.7]$$

wherein a_i e a_o are, respectively, the initial height of the ridges (i.e. H_{RI}, at the input port of the feed), and the height of the ridges at the end of the sinusoidal profile (H_{RO} in Fig. 4.14c). L is the length of the ridges along the sinusoidal tapering and, in our case, is equal to 270 mm. The parameter A can assume values in the range [0, 1] and weighs the profile linearity; $p \in [0, \infty]$ is the exponent of the sine. The optimization of the latter parameter is very important since it strongly influences the side-lobe level (SLL) and, therefore, the illumination of the reflector. In our case, we have selected p = 6, which provides the required SLL.

The final stretch of the feed, including a ridged circular waveguide with constant section, of length L_F, and a radiating aperture with an indentation of dimensions W_{F1}, W_{F2}, H_{F1}, H_{F2} (see Fig. 4.14c) has been optimized for the best input match over the operating bandwidth.

As apparent from the profile of the ridges, shown in Fig. 4.14b, another indentation of dimensions H_I, W_I (see Fig. 4.14b) has been realized at the distance L_I form the input port of the feed. This parameter has been used as a further parameter in order to improve the input match.

The optimization procedure on the parameters L_F, H_{F1}, H_{F2}, W_{F1}, W_{F2}, H_I, W_I, and L_I has been performed using Ansys HFSS. The final values are reported in Table 4.3.

L_F	H_{F1}	H_{F2}	W_{F1}	W_{F2}	L_I	H_I	W_I
70 mm	76 mm	68 mm	5 mm	5 mm	180 mm	20 mm	6 mm

Table 4.3: Optimized parameters of geometry feed.

The plots of optimization of some parameters is presented. In Figure 4.17 we show the frequency response of the feed (S_{11}) for different values of the length L_I, in Figure 4.18 the frequency response for different values of the length L_F and, in Figure 4.19, the frequency response for different values of the height H_{F1}.

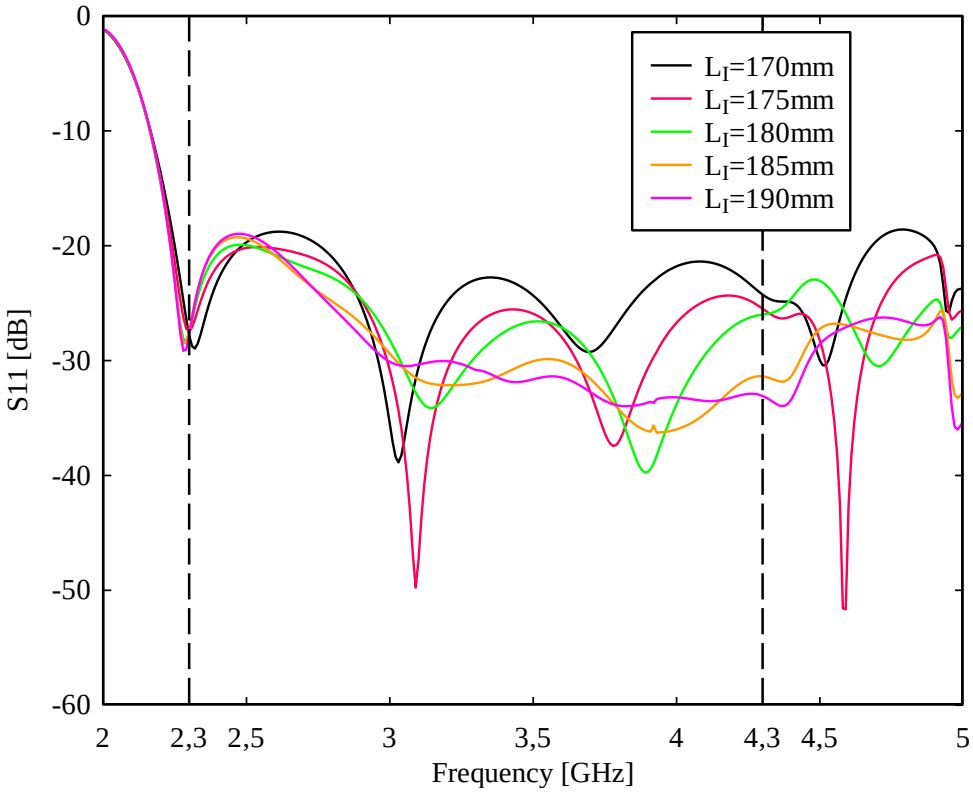

Fig. 4.17: Frequency response for different values of the length L_I.

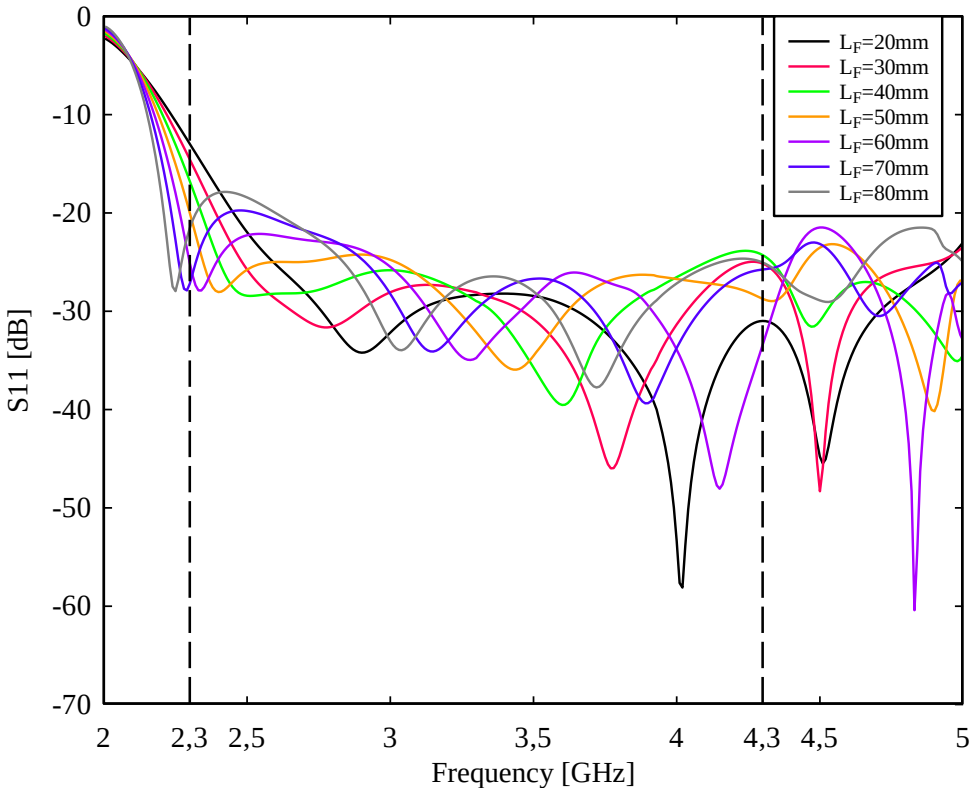

Fig. 4.18: Frequency response for different values of the length L_F.

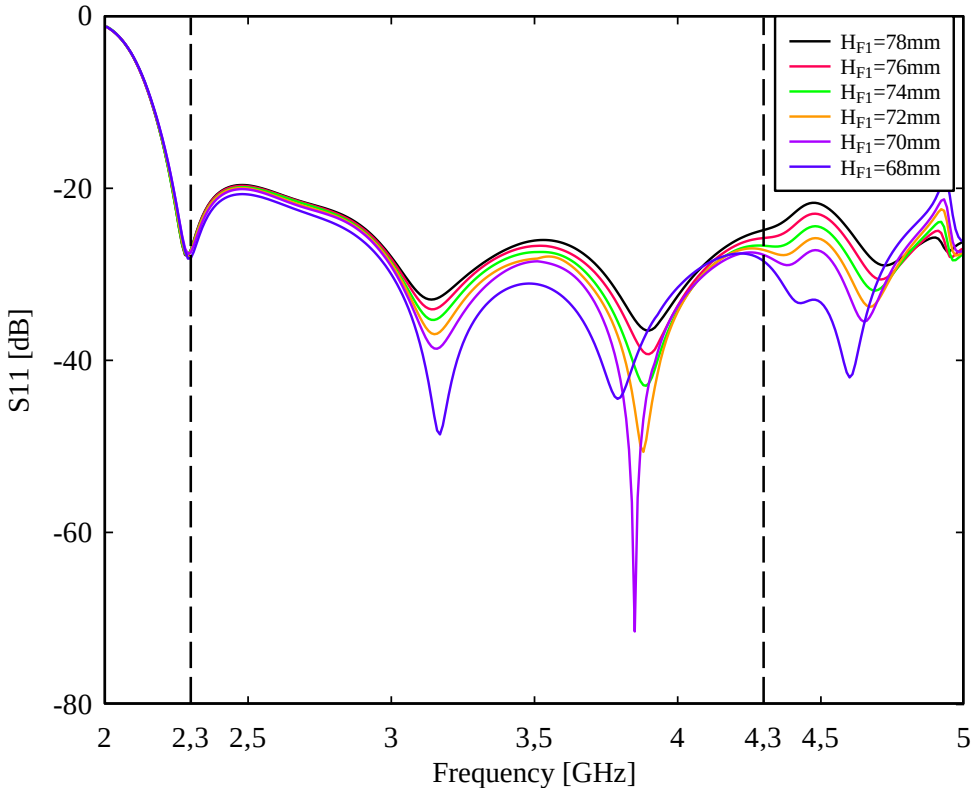

Fig. 4.19: Frequency response for different values of the length H_{F1}.

The simulation performances of the proposed antenna are presented.

The reflection coefficient of the isolated feed is below -20 dB over a 60% bandwidth (Fig. 4.20).

Figs 4.21, 4.22 and 4.23 show the normalized radiation pattern in the ϕ=0°, ϕ=45°, and ϕ=90° planes at the frequencies 2.3 GHz, 3.3 GHz, and 4.3 GHz. Variations between the patterns can be observed at these frequencies. The radiation patterns of only one polarization are plotted for brevity. However, the performance of the other polarization is virtually the same.

As can be seen from Figure 4.22, the initial request of an edge illumination of -13 dB at 74° at 3.3 GHz was basically met, whereas the edge illumination at 2.3 GHz and 4.3 GHz is, respectively, -9 dB and -19 dB. The radiation pattern at the central frequency, 3.3 GHz is optimal; the pattern at 2.3 GHz is quite good, and at 4.3 GHz the edge taper can be considered still acceptable [52].

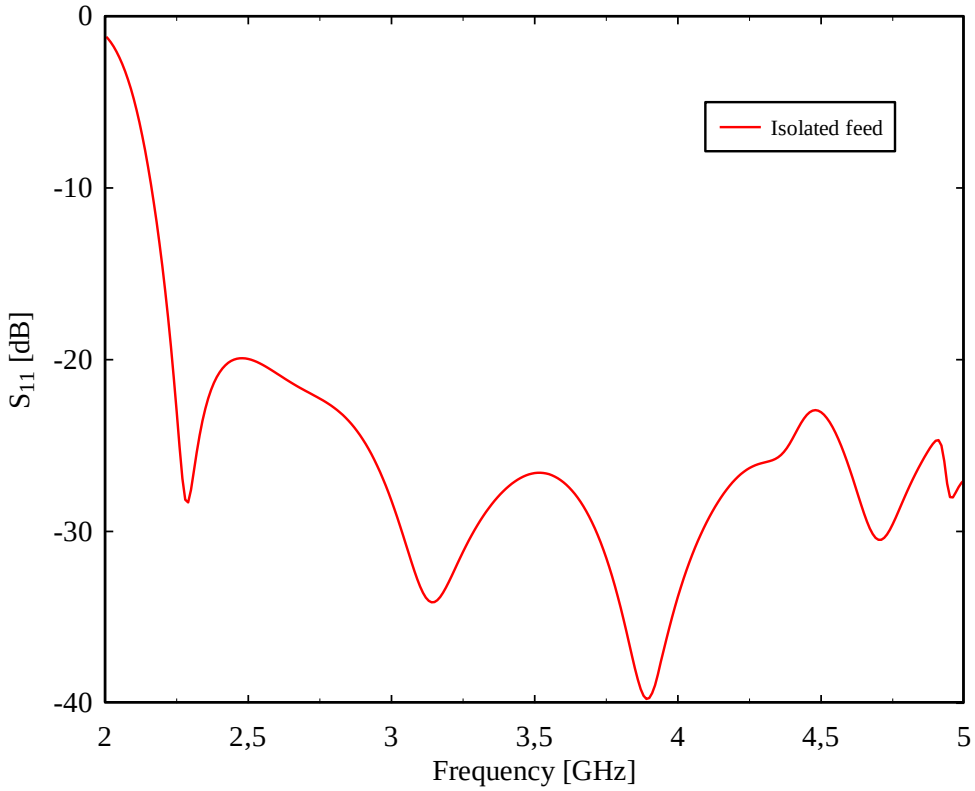

Fig. 4.20: Return loss of the isolated feed.

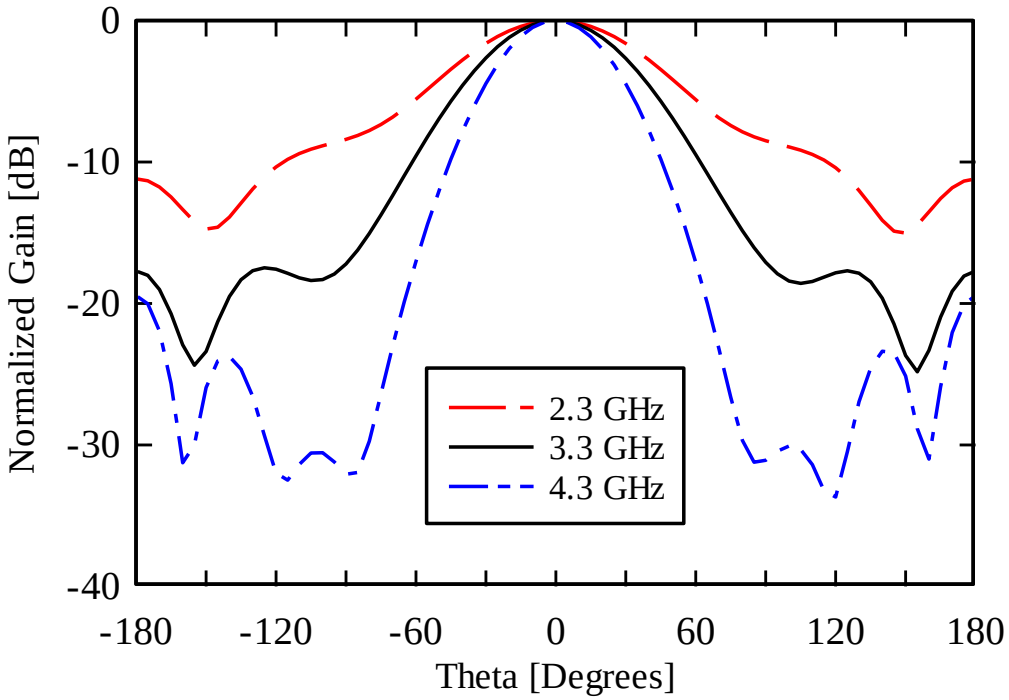

Fig. 4.21: Normalized radiation patterns of the isolated feed at 2.3 GHz, 3.3GHz and 4.3 GHz in the ϕ = 0° plane.

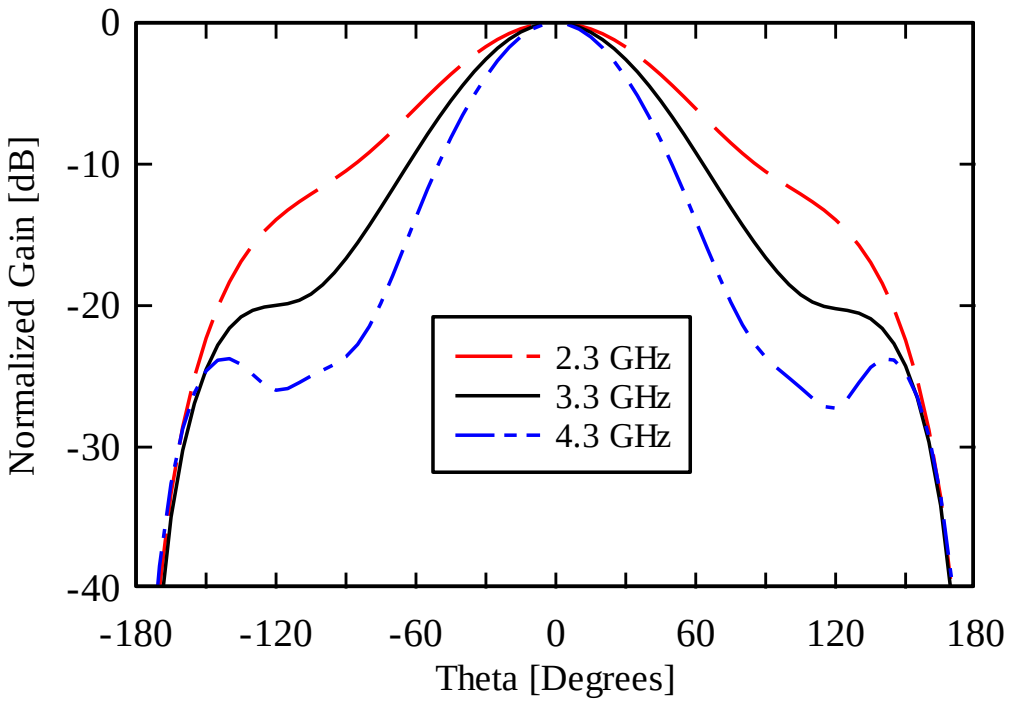

Fig. 4.22: Normalized radiation patterns of the isolated feed at 2.3 GHz, 3.3GHz and 4.3 GHz in the ϕ = 45° plane.

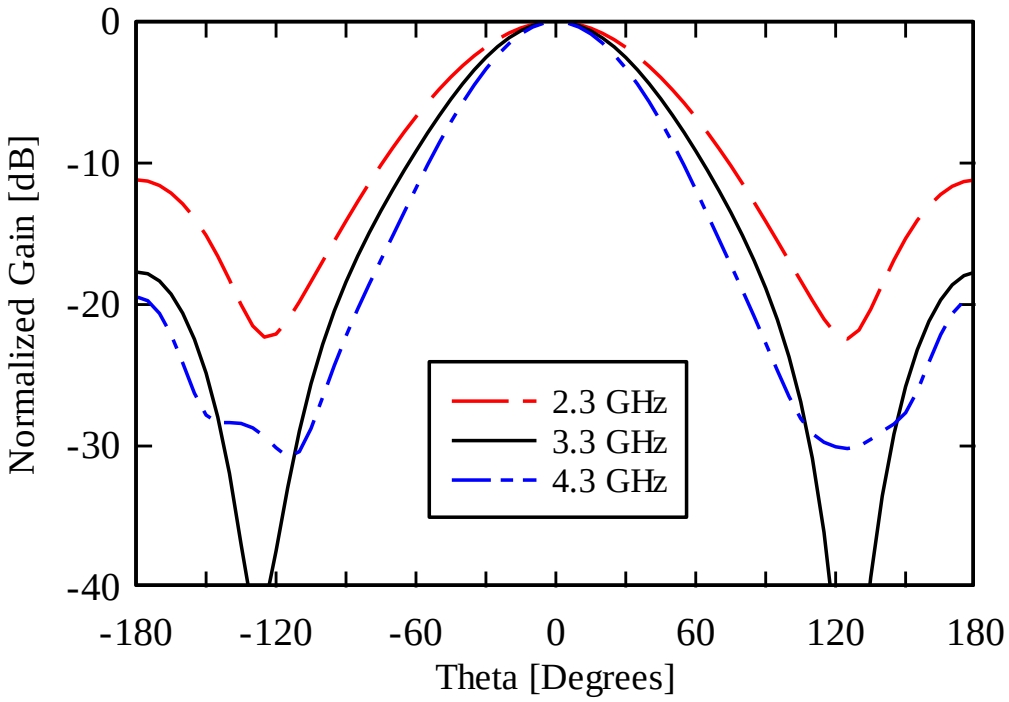

Fig. 4.23: Normalized radiation patterns of the isolated feed at 2.3 GHz, 3.3GHz and 4.3 GHz in the ϕ = 90° plane.

The design previously described has considered an isolated feed horn, but the real implementation involves an array of seven elements in a hexagonal grid. As explained in the previous section, the choose of the spatial configuration in this hexagonal grid and the number of feeds on a focal plane array (FPA) have been selected to maximize the Field of View of the antenna, keeping in mind the available room in focal cabin of SRT and load limit of the Primary Focus Positioner (PFP) of the Sardinia Radio Telescope. The minimum distance between centers of feeds, which maximize the aperture efficiency of the antenna and produces the better mapping of an extended radio astronomical source, is equal to 100 mm [52].

In order to evaluate the mutual coupling effect between the feeds in the multifeed configuration, we simulated the electromagnetic behavior of the structure with, respectively, three, five and seven elements.

Fig. 4.24 shows the illustration of the first configuration of multibeam receiver with three elements, where *d*=100mm, *Di*=43mm and *De*=48mm and Fig. 4.25 shows the multibeam layout used in the 3D electromagnetic software Ansoft HFSS.

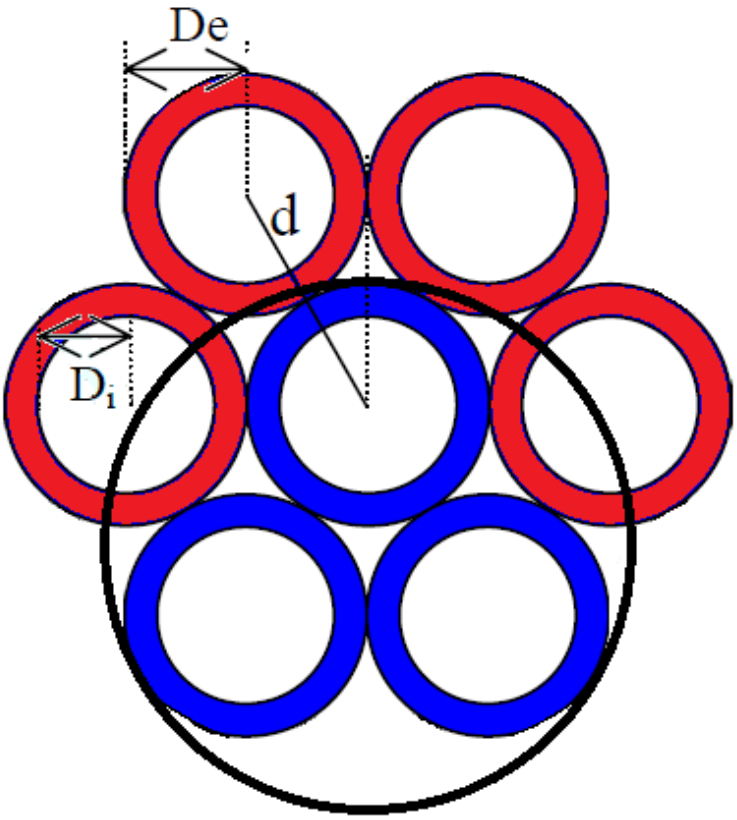

Fig. 4.24: Multibeam configuration with three elements.

Fig. 4.25: HFSS multifeed layout.

Figs. 4.26, 4.27 and 4.28 show the performances of the Feed1 of this configuration in terms of return loss and radiation pattern.

The reflection coefficient is below -20 dB over a 60% bandwidth. The normalized radiation pattern is show in the ϕ=45° plane at the frequencies 2.3 GHz, 3.3 GHz, and 4.3 GHz.

In order to evaluate the mutual coupling effect between the feeds in the multifeed configuration, we show the comparison between the simulated performances of the central feed when included in the multifeed array and the simulated performances of the isolated feed.

The reflection coefficient remains below -20 dB. The isolation between feed2 and feed1 is below -28 dB. Variations between the pattern of multifeed configuration e isolated feed can be observed, especially at the lower frequency of the operating band. In fact, the radiation pattern of multibeam is asymmetrical than the radiation pattern of the isolated feed. This effect is due to the position not central of the feed in this configuration. All feeds are affected by the presence of the other two feeds only on a side, as we can see in Fig. 4.25.

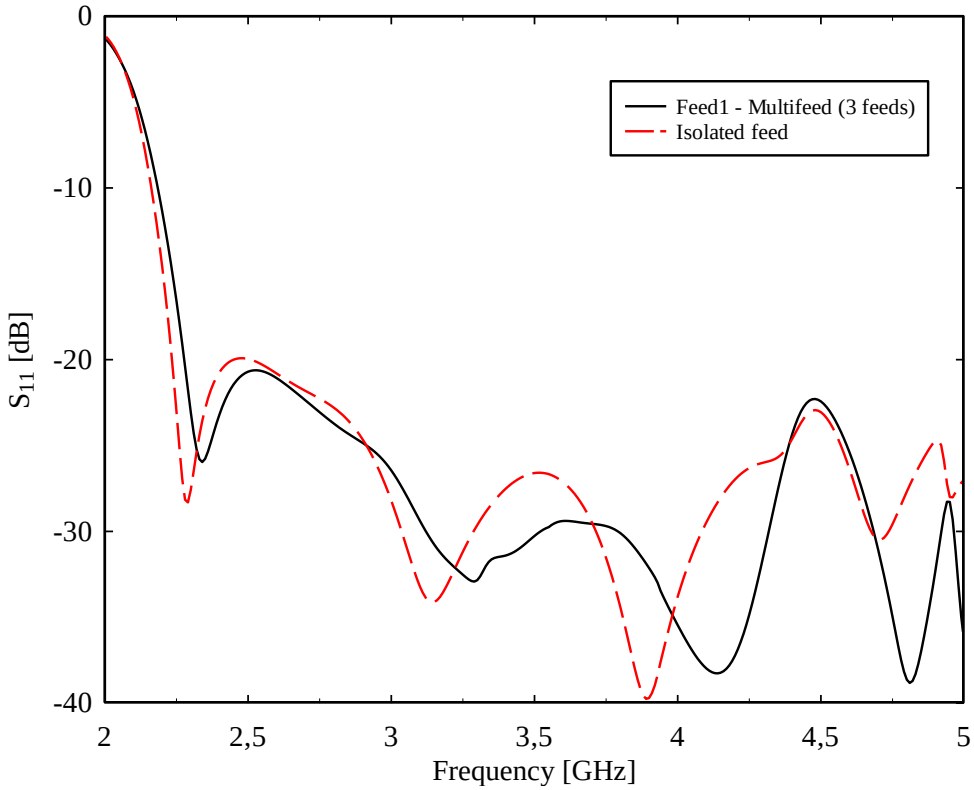

Fig. 4.26: Simulated reflection coefficient of the isolated feed and of the central element of the multifeed configuration with three feeds.

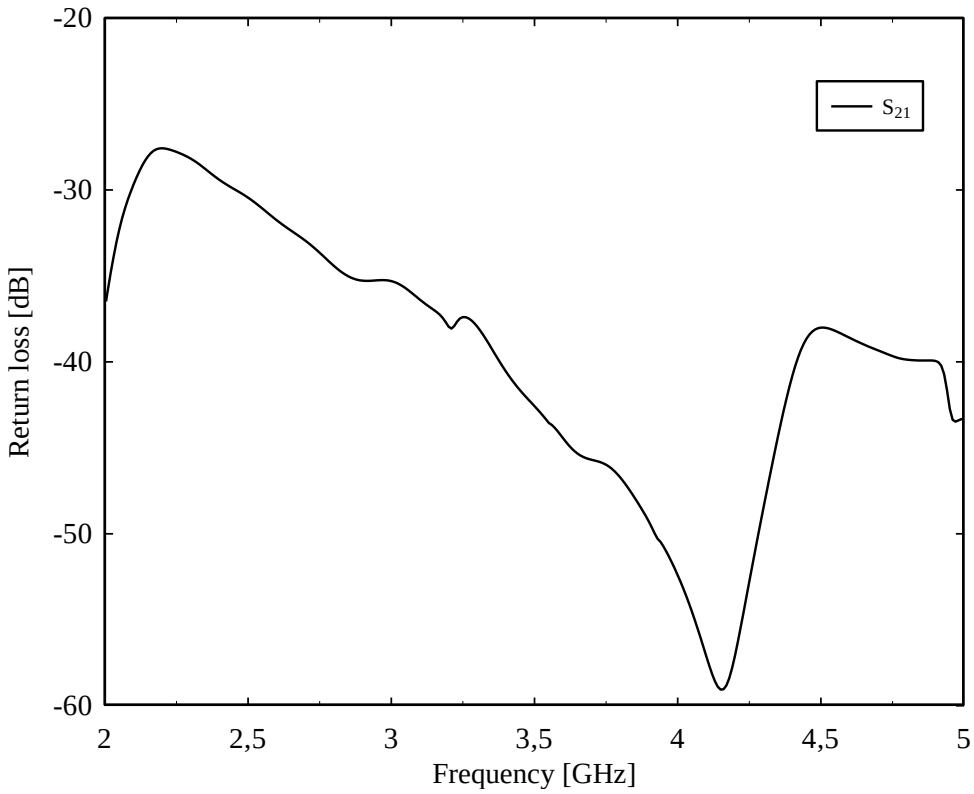

Fig. 4.27: Isolation between Feed1 and Feed2 of the multifeed configuration with three feeds.

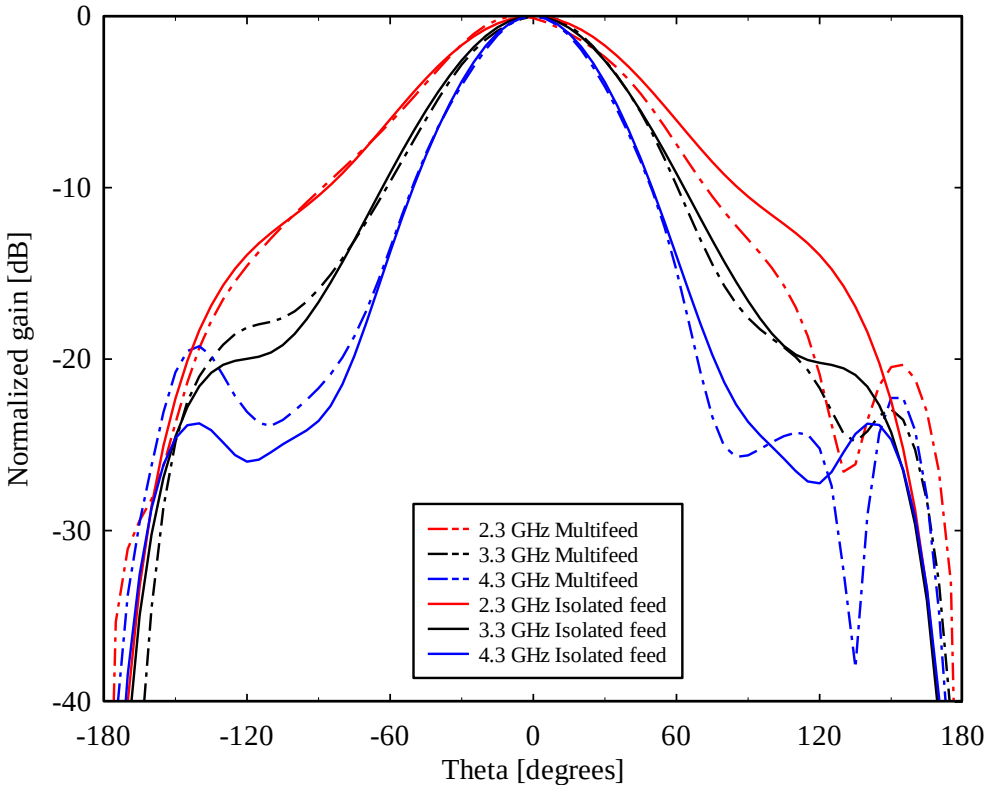

Fig. 4.28: Normalized radiation patterns of the feed1 of multibeam configuration and the isolated feed at 2.3 GHz, 3.3GHz and 4.3 GHz in the ϕ = 45° plane.

Fig. 4.29 shows the illustration of the second configuration of multibeam receiver with five elements, where *d*=100mm, *Di*=43mm and *De*=48mm and Fig. 4.30 shows the multibeam layout used in the 3D electromagnetic software Ansoft HFSS.

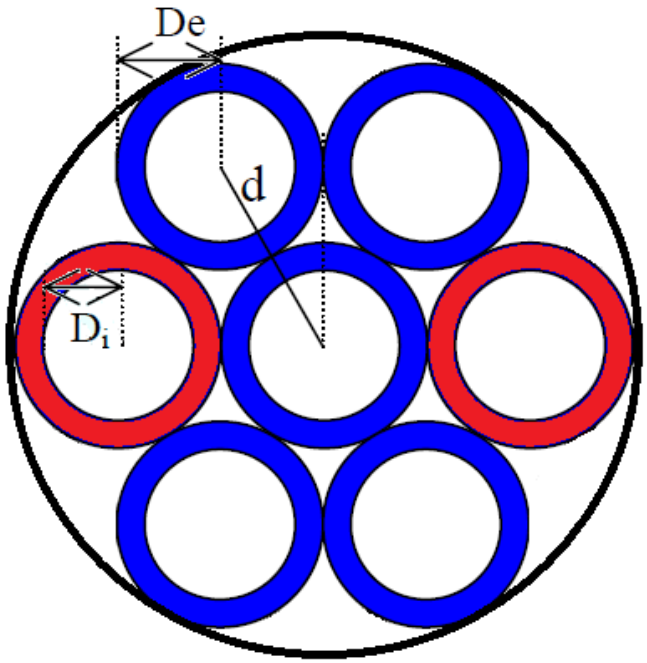

Fig. 4.29: Multibeam configuration with five elements.

Fig. 4.30: HFSS multifeed layout.

Figs. 4.31, 4.32 and 4.33 show the performances of the Feed1 of this configuration in terms of return loss and radiation pattern.

The reflection coefficient is below -20 dB over a 60% bandwidth. The normalized radiation pattern is show in the ϕ=45° plane at the frequencies 2.3 GHz, 3.3 GHz, and 4.3 GHz.

In order to evaluate the mutual coupling effect between the feeds in the multifeed configuration, we show the comparison between the simulated performances of the central feed when included in the multifeed array and the simulated performances of the isolated feed.

The reflection coefficient remains below -20 dB, the isolation between feed1 and feed2 is below -28dB and the radiation pattern complies the feed design specifications. Variations between the pattern of multifeed configuration e isolated feed can be observed, especially at the lower frequency of the operating band. In fact, the radiation pattern of multibeam is more directive than the radiation pattern of the isolated feed. This effect is due to the position of the feed in this configuration that is affected by the presence of the other four feeds, as we can see in Fig. 4.30.

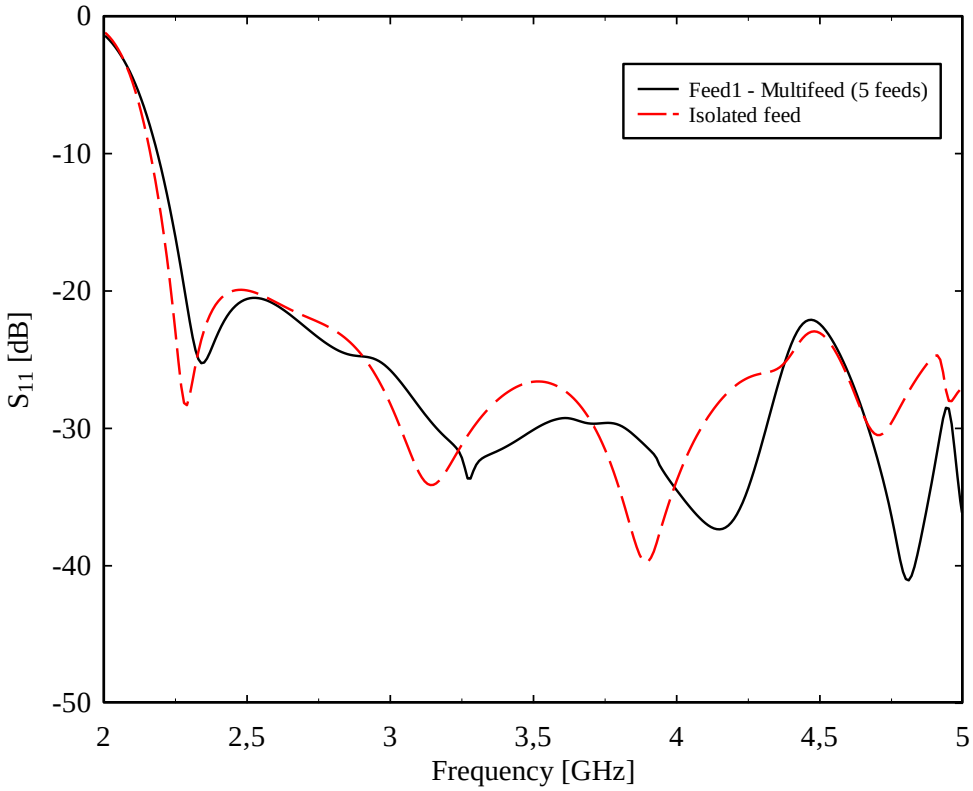

Fig. 4.31: Simulated reflection coefficient of the isolated feed and of the central element of the multifeed configuration with five feeds.

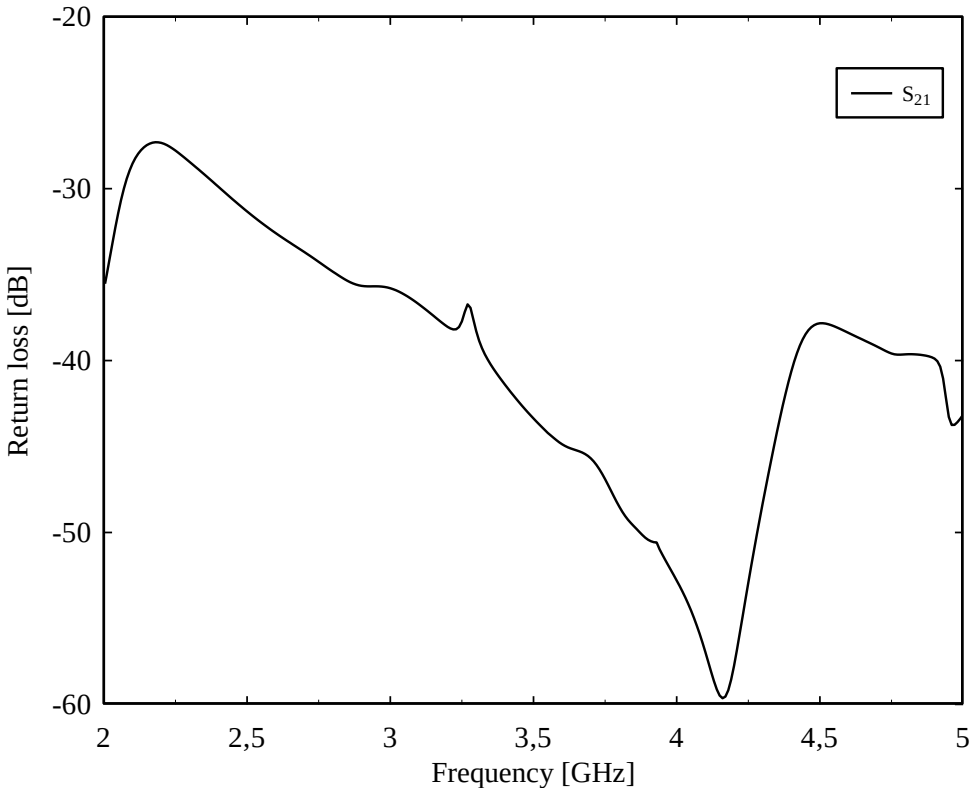

Fig. 4.32: Isolation between Feed1 and Feed2 of the multifeed configuration with five feeds.

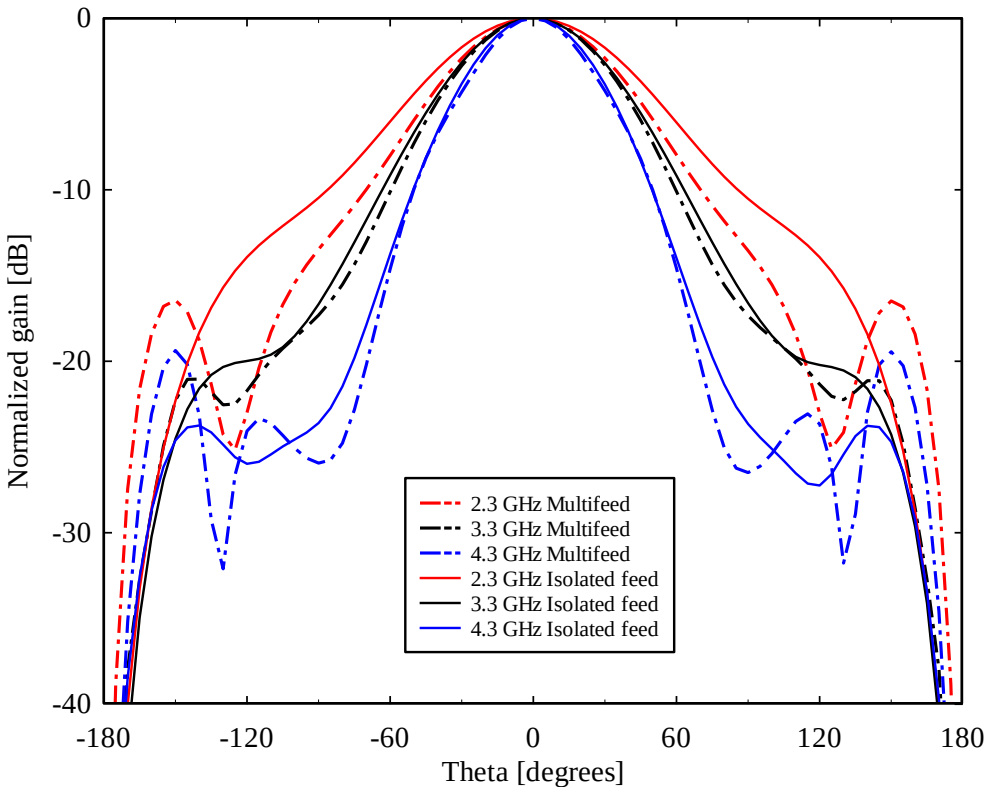

Fig. 4.33: Normalized radiation patterns of the feed1 of multibeam configuration and the isolated feed at 2.3 GHz, 3.3GHz and 4.3 GHz in the ϕ = 45° plane.

Fig. 4.34 shows the illustration of the third configuration of multibeam receiver with seven elements, where *d*=100mm, *Di*=43mm and *De*=48mm and Fig. 4.35 shows the multibeam layout used in the 3D electromagnetic software Ansoft HFSS. This is the final layout of multibeam receiver to install in the Sardinia Radio Telescope.

The design of the radiating aperture of single feed described above, takes into account the limited space available. Moreover, in order to minimize the mutual coupling effect between the feeds, we decided to fill the space between feeds with an absorbing material (i.e. Eccosorb MF-124). In Figure 4.35, the layout of multifeed with enclosure is shown where the absorbing material is displayed in green.

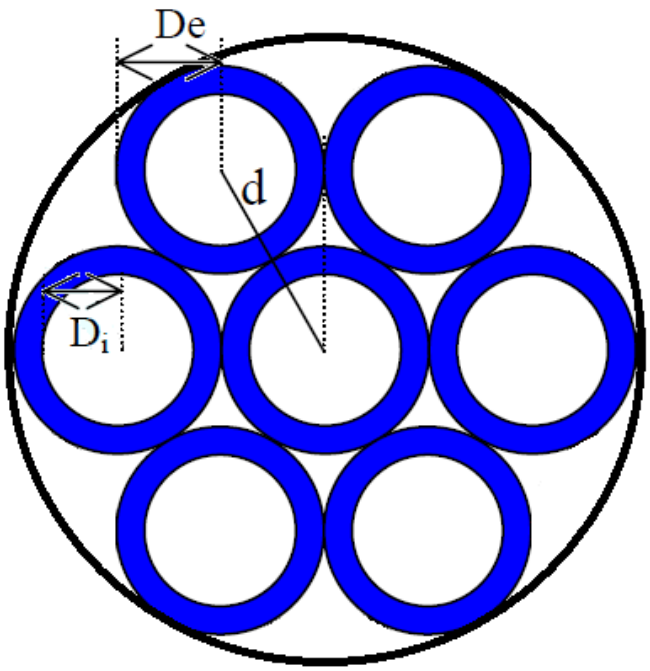

Fig. 4.34: Multibeam configuration with seven elements.

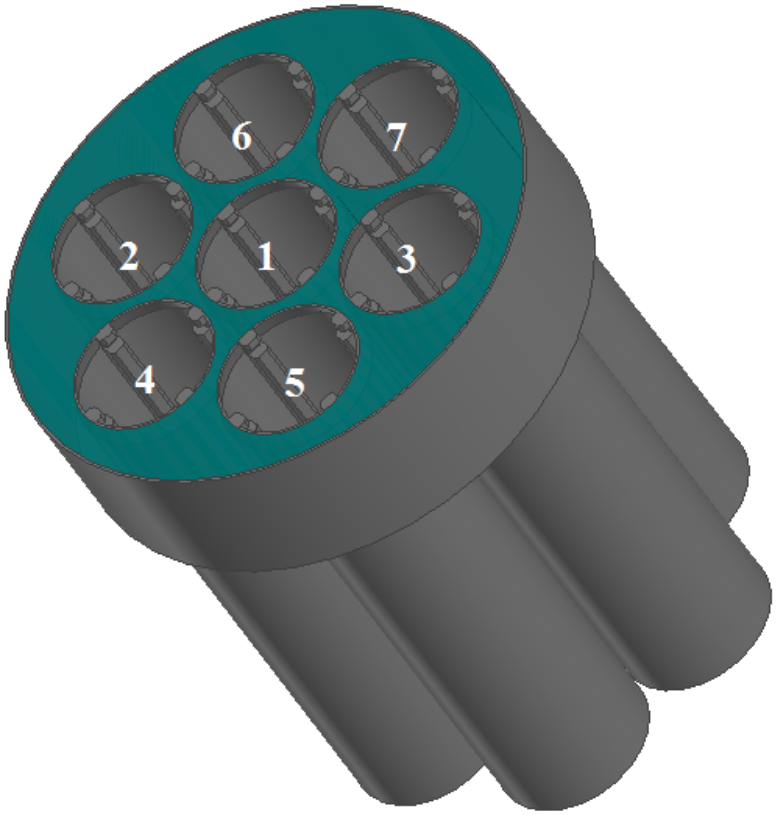

Fig. 4.35: Final multifeed layout.

Figs. 4.36, 4.37, 4.38, 4.39 and 4.40 show the performances of the Feed1 of this configuration in terms of return loss and radiation pattern.

The reflection coefficient is below -20 dB over a 60% bandwidth. The normalized radiation pattern is show in the ϕ=0°, ϕ=45°, and ϕ=90° planes at the frequencies 2.3 GHz, 3.3 GHz, and 4.3 GHz.

In order to evaluate the mutual coupling effect between the feeds in the multifeed configuration, we show the comparison between the simulated performances of the central feed when included in the multifeed array and the simulated performances of the isolated feed.

The reflection coefficient remains below -20 dB. The isolation is below -25 dB unless the lower frequency of operating bandwidth where is below -20dB. The radiation pattern complies the feed design specifications. Variations between the pattern of multifeed configuration e isolated feed can be observed, especially at the lower frequency of the operating band. In fact, the radiation pattern of multibeam is more directive than the radiation pattern of the isolated feed. This effect is due to the position of the feed in this configuration that is affected by the presence of the other six feeds, as we can see in Fig. 4.35.

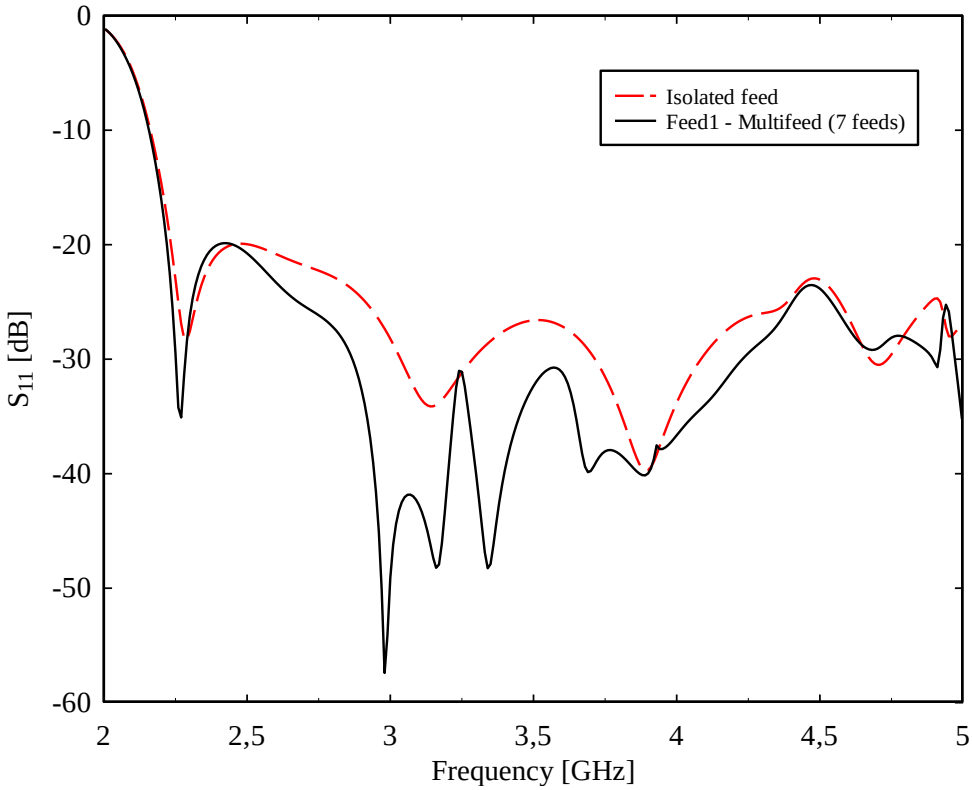

Fig. 4.36: Simulated reflection coefficient of the isolated feed and of the central element of the multifeed configuration.

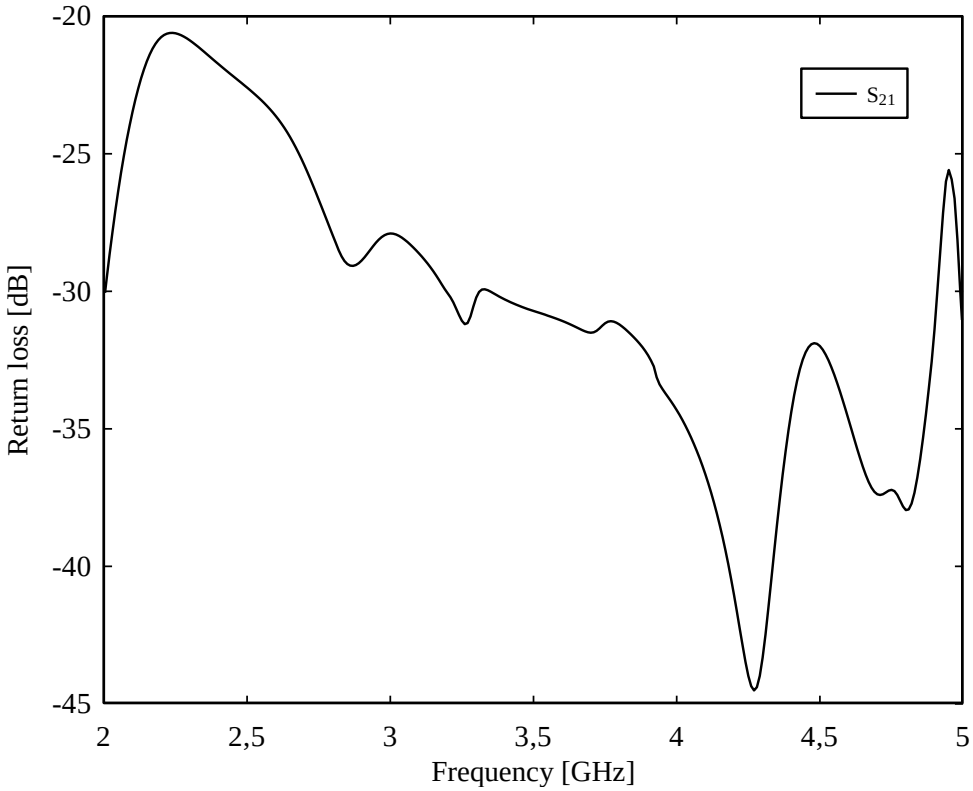

Fig. 4.37: Isolation between Feed1 and Feed2 of the multifeed configuration with seven feeds.

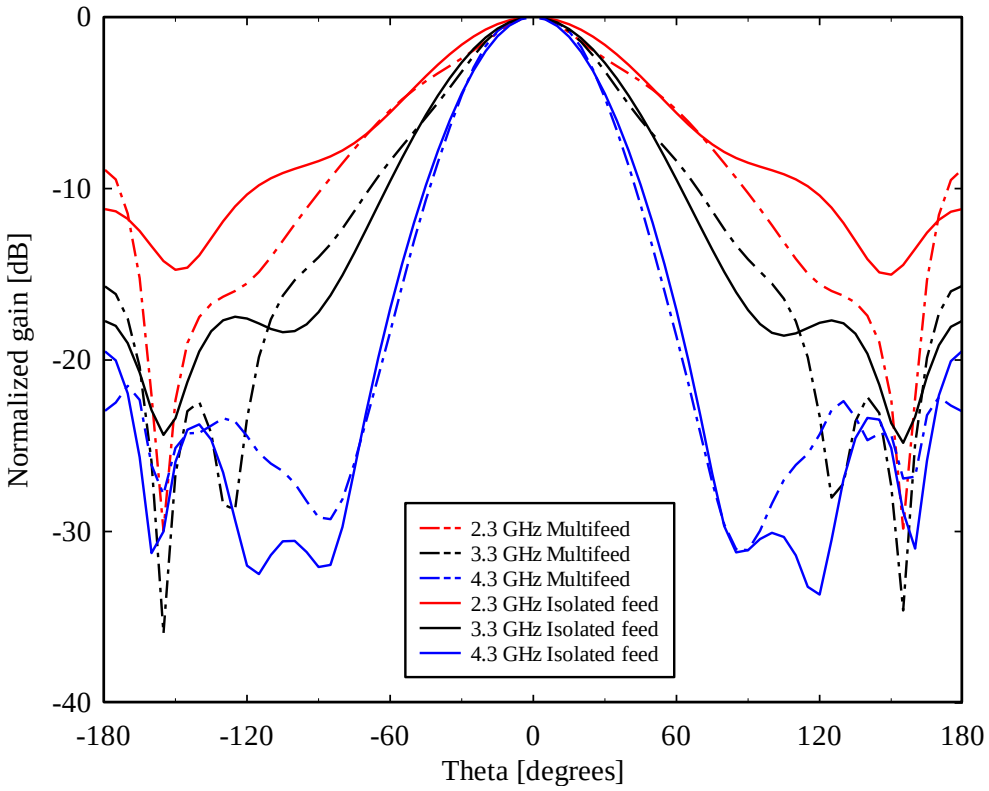

Fig. 4.38: Normalized radiation patterns of the feed1 of multibeam configuration and the isolated feed at 2.3 GHz, 3.3GHz and 4.3 GHz in the ϕ = 0° plane.

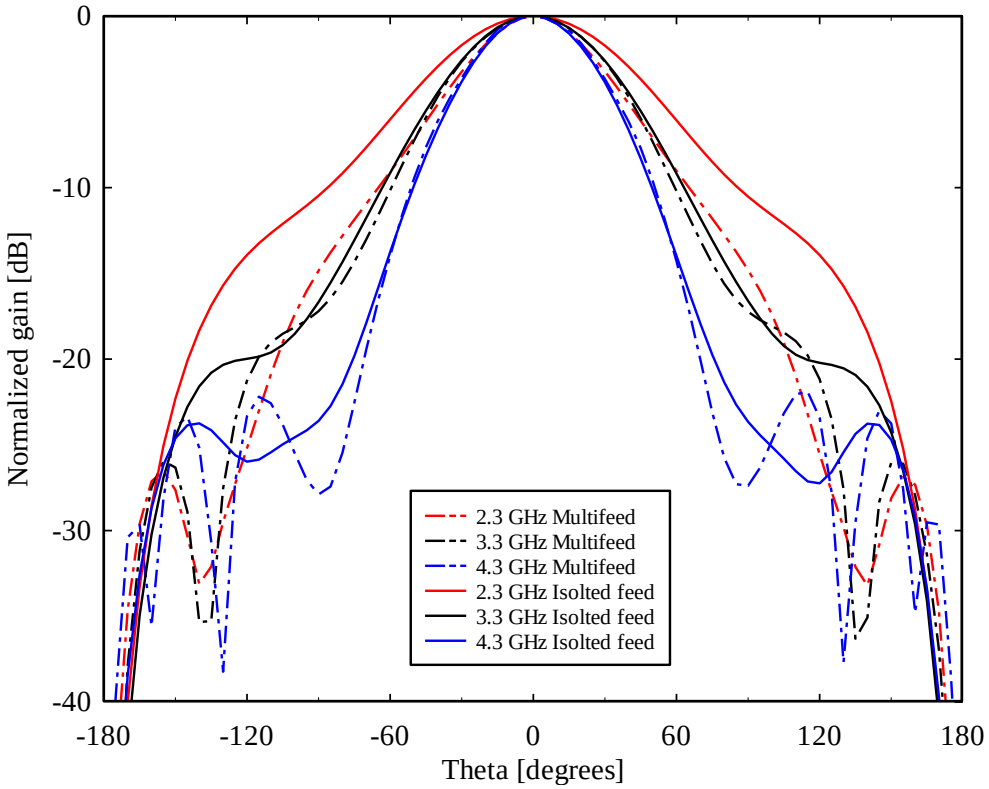

Fig. 4.39: Normalized radiation patterns of the feed1 of multibeam configuration and the isolated feed at 2.3 GHz, 3.3GHz and 4.3 GHz in the ϕ = 45° plane.

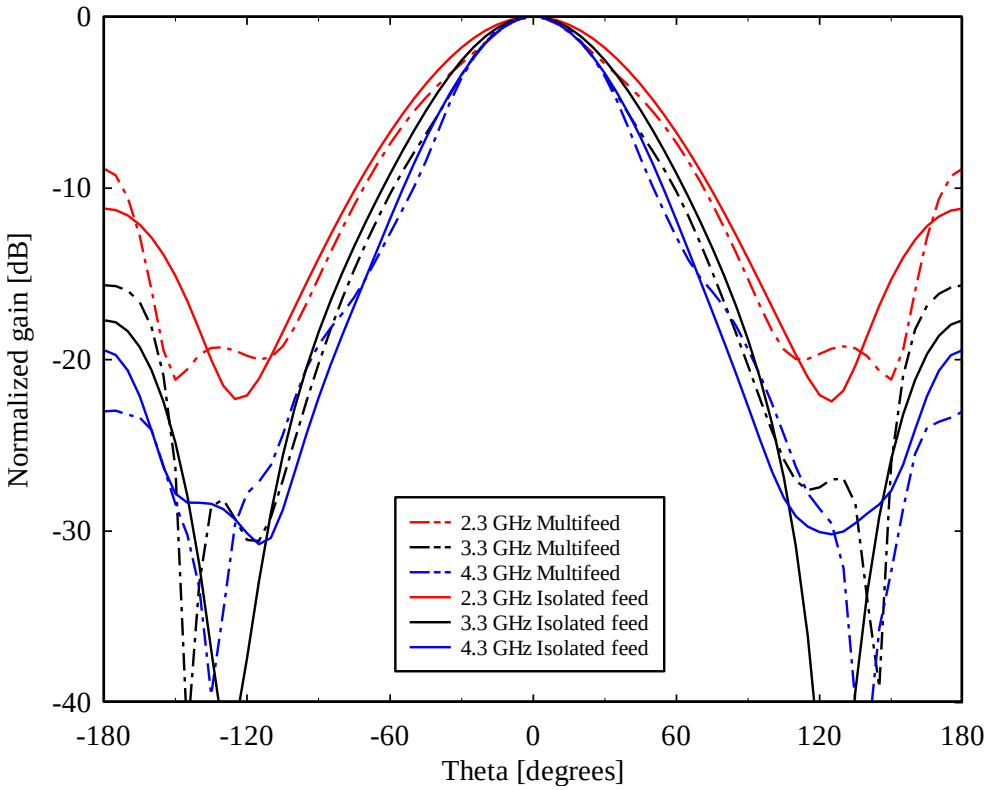

Fig. 4.40: Normalized radiation patterns of the feed1 of multibeam configuration and the isolated feed at 2.3 GHz, 3.3GHz and 4.3 GHz in the ϕ = 90° plane.

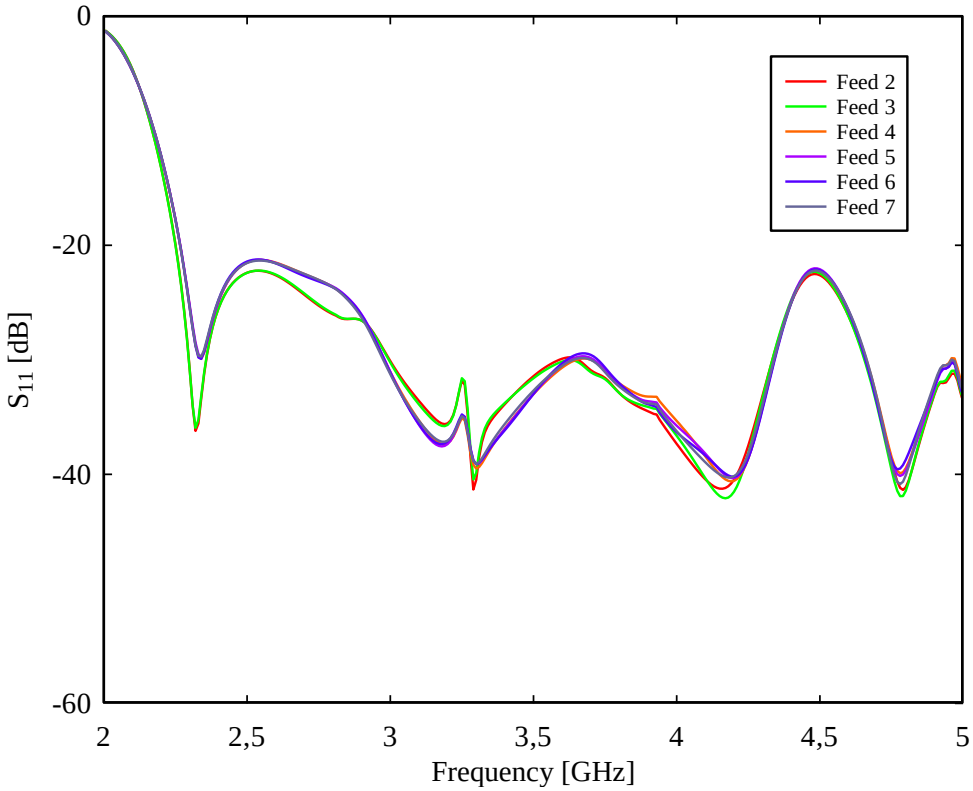

Fig. 4.41: Return loss of the other six feeds of multibeam receiver.

Fig. 4.41 shows the return loss of the other six feeds of multibeam receiver. The other feeds are affected by the central feed, but their return loss is below -20dB in the operating bandwidth.

We also show the comparison between the normalized radiation pattern of the feed2 and the feed4 of the multibeam receiver and the normalized radiation pattern of the feed1 of the multibeam in the worst case (ϕ=45° plane) at the frequencies 2.3 GHz, 3.3 GHz, and 4.3 GHz. The radiation pattern of feed2, see Fig. 4.42, is affected by central feed and the other two neighboring feeds, the feed6 and the feed4. The radiation pattern of feed4, see Fig. 4.43, is affected by central feed and the other two neighboring feeds, the feed2 and the feed5.

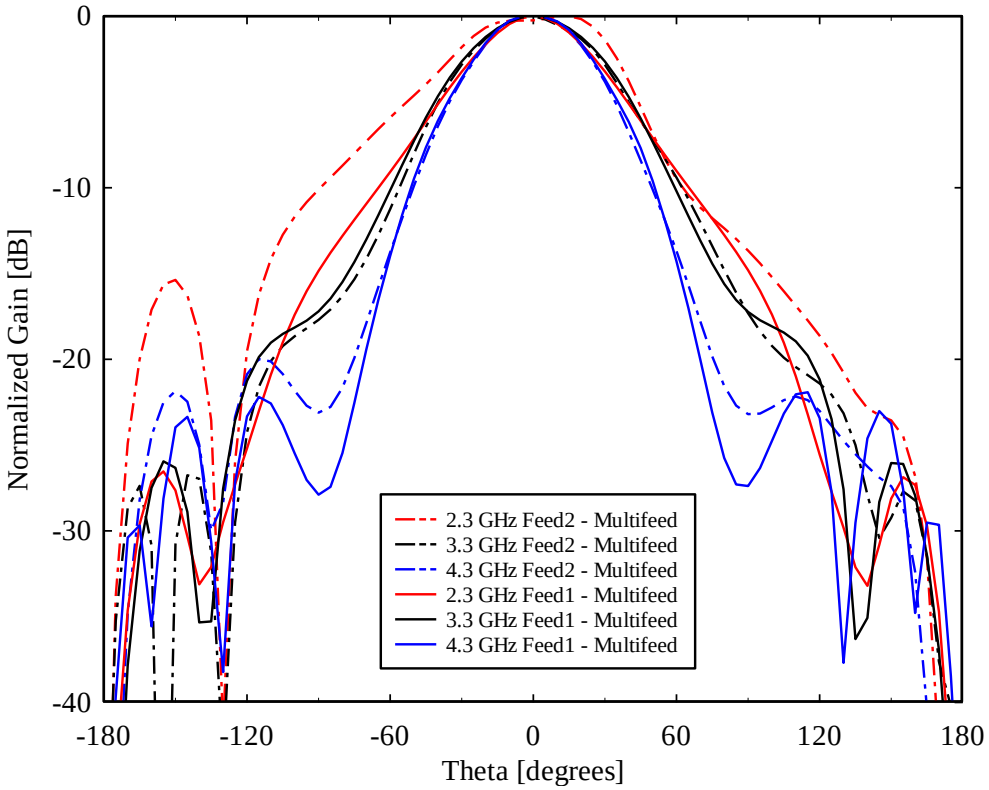

Fig. 4.42: Normalized radiation patterns of the feed2 and feed1 at 2.3 GHz, 3.3GHz and 4.3 GHz in the ϕ = 45° plane.

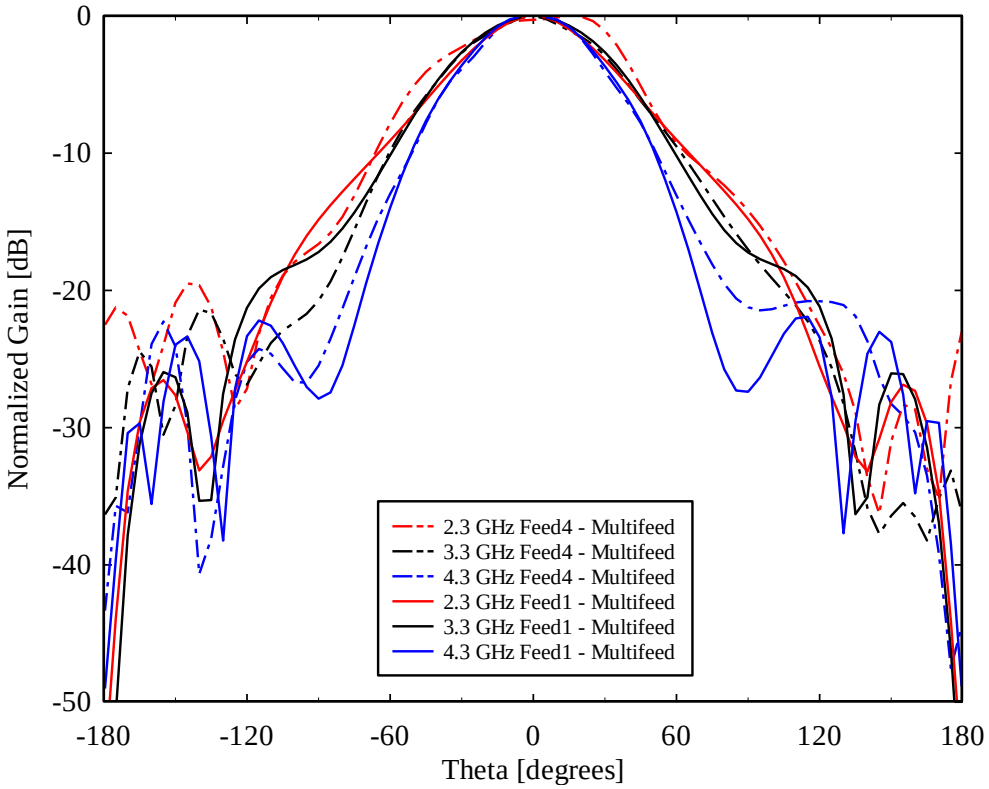

Fig. 4.43: Normalized radiation patterns of the feed4 and feed1 at 2.3 GHz, 3.3GHz and 4.3 GHz in the ϕ = 45° plane.

The electromagnetic coupling between the Sardinia Radio Telescope and the multifeed horn system has been simulated in order to estimate the antenna gain and the cross-polarization component. The complete system has been modeled using the 3D analysis software GRASP 9 by TICRA.

In general, most antenna systems, especially those with high gain and directivity used in radio astronomy must be analysed using detailed numerical models such as GRASP. This simulation tool is specifically tailored for the analysis of large radio telescopes, providing a very accurate modelling, and the results are, therefore, in very good agreement with experiment [53].

In the GRASP model of SRT we have taken into account the blocking effects of the subreflector, with an 8 m diameter hole centered in the main reflector, and the quadrupod structure (struts).

In order to evaluate the mutual coupling effect between the multifeed configuration and SRT, we simulated the electromagnetic behavior of the structure with, respectively, three, five and seven elements using the GRASP software. Only the blocking effects of subreflector is considered in the GRASP model of SRT used in these simulations.

In Fig 4.44, we show the radiation pattern of the SRT illuminated by the central feed of the multifeed array with three feeds, at 2.3 GHz, at 3.3 GHz, and at 4.3 GHz.

In Fig 4.45, we show the radiation pattern of the SRT illuminated by the central feed of the multifeed array with five feeds, at 2.3 GHz, at 3.3 GHz, and at 4.3 GHz.

In Fig 4.46, we show the radiation pattern of the SRT illuminated by the central feed of the multifeed array with seven feeds, at 2.3 GHz, at 3.3 GHz, and at 4.3 GHz.

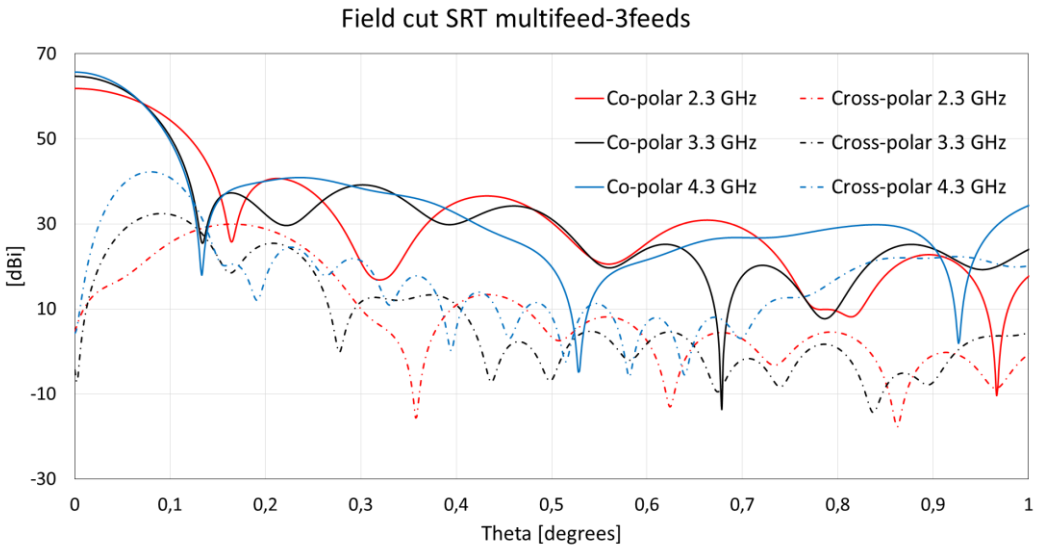

Fig. 4.44: Radiation pattern of the SRT with the multifeed system (3 feeds).

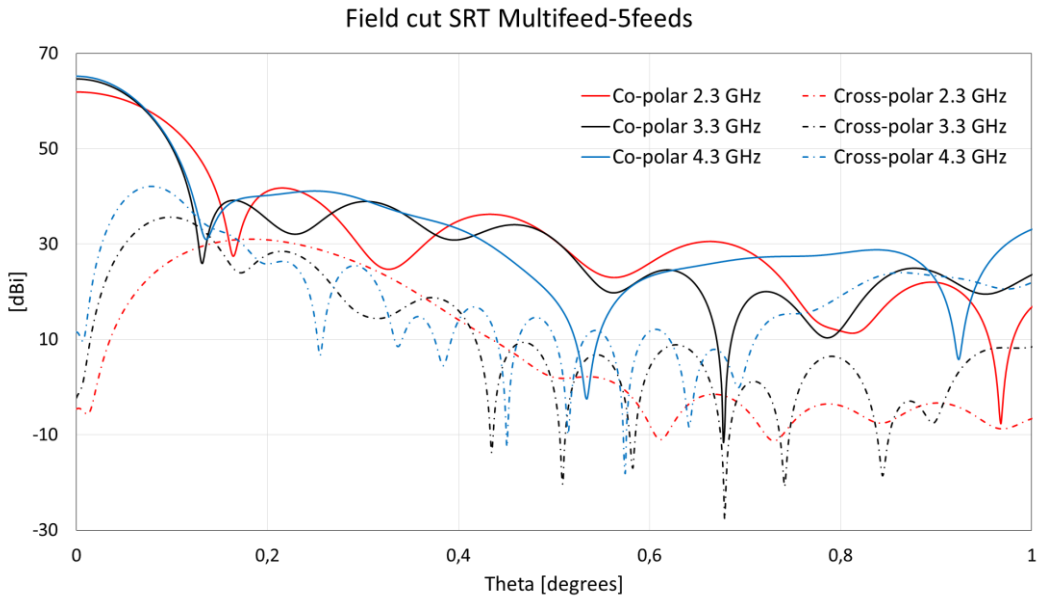

Fig. 4.45: Radiation pattern of the SRT with the multifeed system (5 feeds).

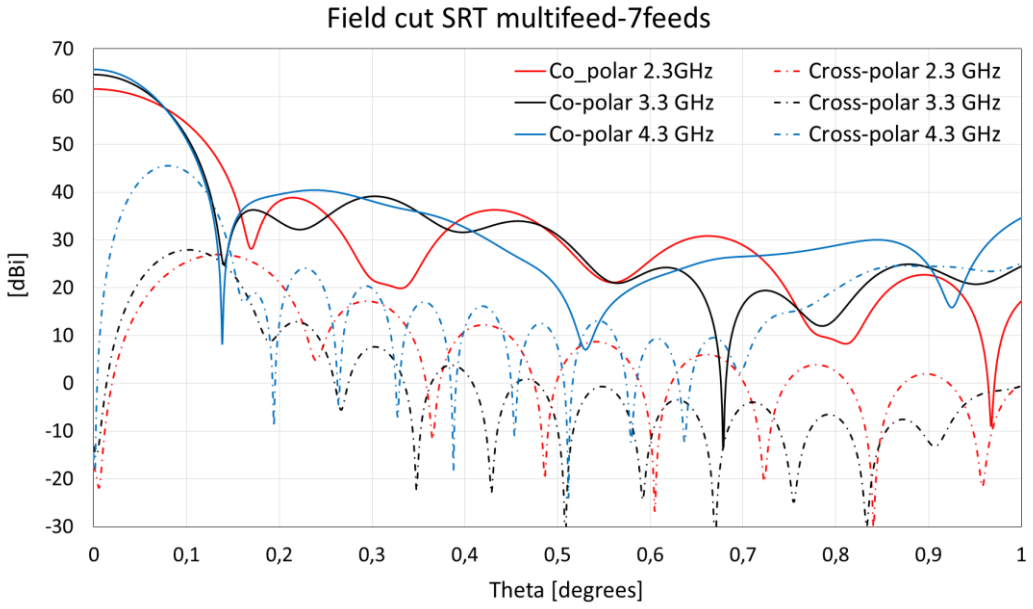

Fig. 4.46: Radiation pattern of the SRT with the multifeed system (7 feeds).

The antenna gain for all configurations is between 62 dBi at 2.3 GHz and 66 dBi at 4.3 GHz. The cross polarization level is very good (below -30 dB) at 2.3 GHz and 3.3 GHz, whereas it is quite higher (-20 dB), but still acceptable, at 4.3 GHz, caused by the particular design of radiating aperture.

We also simulated the electromagnetic behavior of the final configuration of multibeam receiver using for the simulation the complete GRASP model of SRT. Fig. 4.47, 4.48 and 4.49 show the radiation pattern of the SRT illuminated by the central feed of the multifeed array with seven feeds. We can see the effect caused by the quadrupod structure (struts) of SRT.

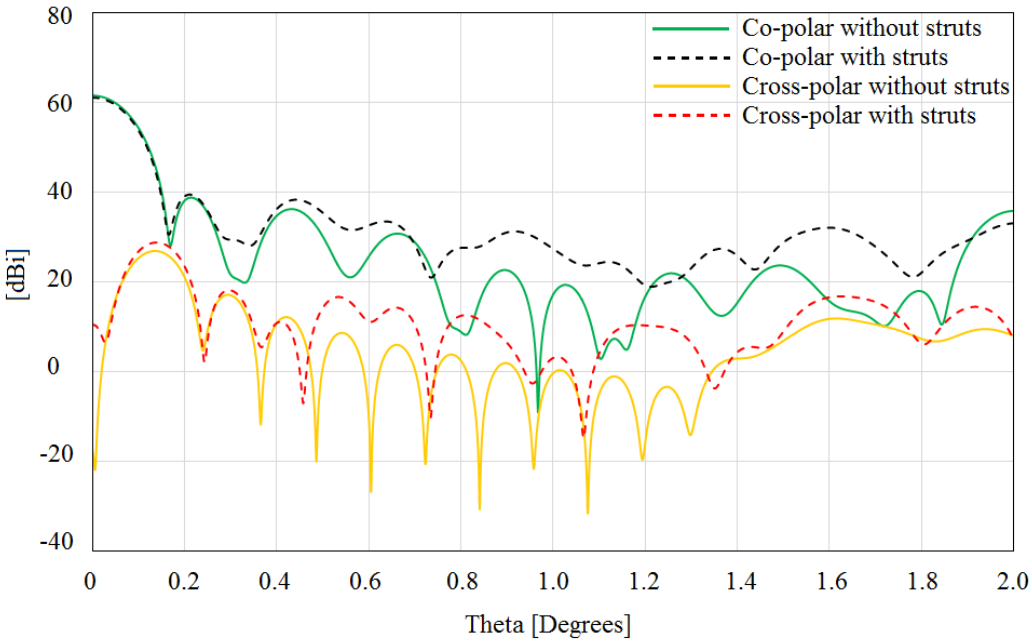

Fig. 4.47: Radiation pattern of the SRT with the multifeed system at 2.3 GHz.

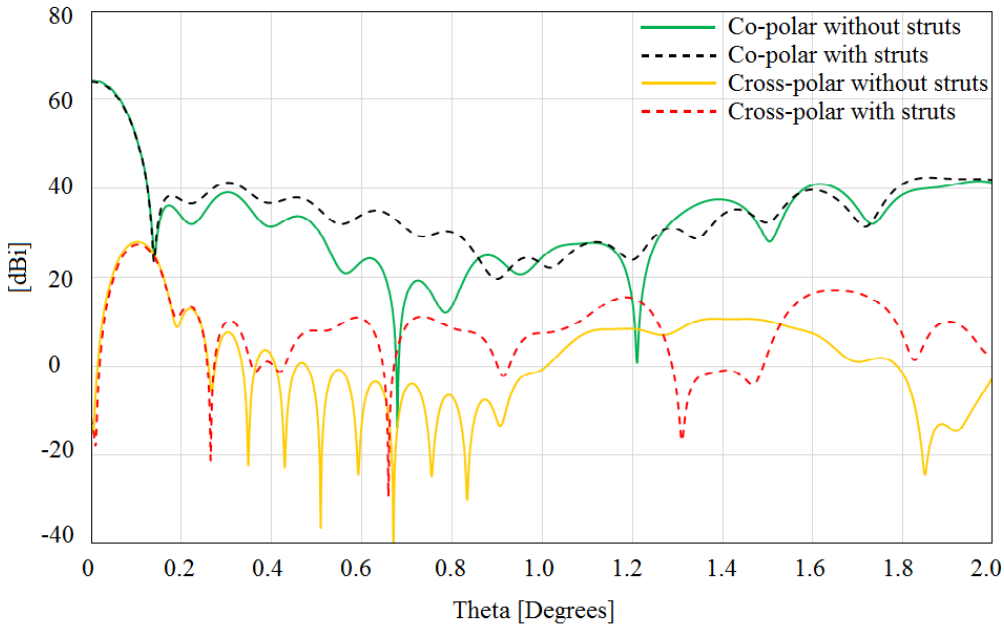

Fig. 4.48: Radiation pattern of the SRT with the multifeed system at 3.3 GHz.

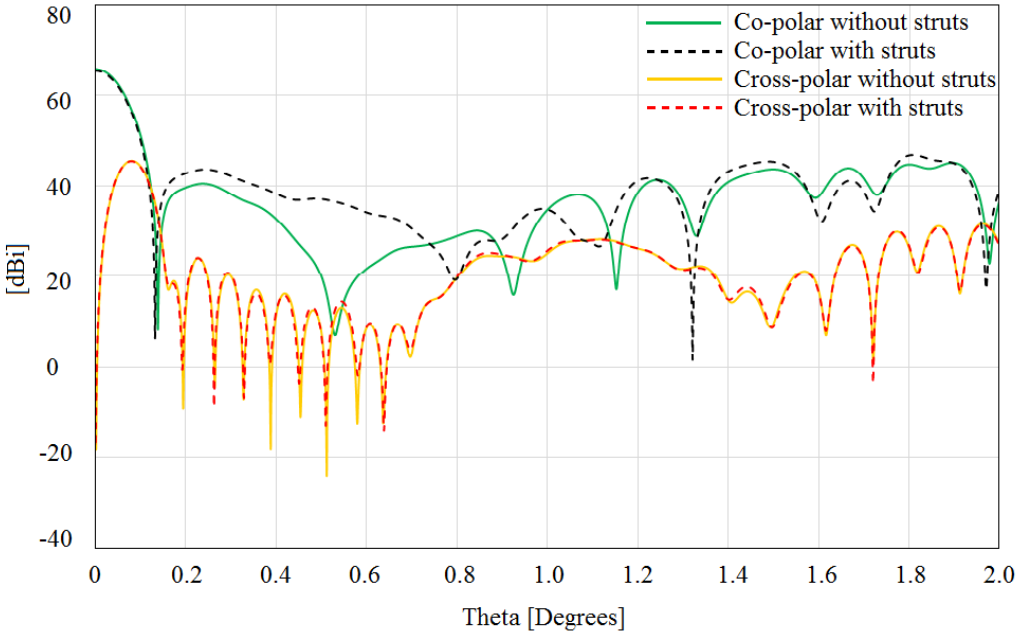

Fig. 4.49: Radiation pattern of the SRT with the multifeed system at 4.3 GHz.

In Figs 4.50, 4.51 and 4.52 we also show the radiation pattern of the SRT illuminated by the feed2 of the multifeed array, at 2.3 GHz, at 3.3 GHz, and at 4.3 GHz. The maximum value of the gain is shifted toward left direction of 0.21°. It is the main effect due to change of position of this feed which is shifted by 50 mm toward the negative x-axis, as we can see in Fig. 4.34. The antenna gain is between 61.5 dBi at 2.3 GHz and 65 dBi at 4.3 GHz at -0.21°.

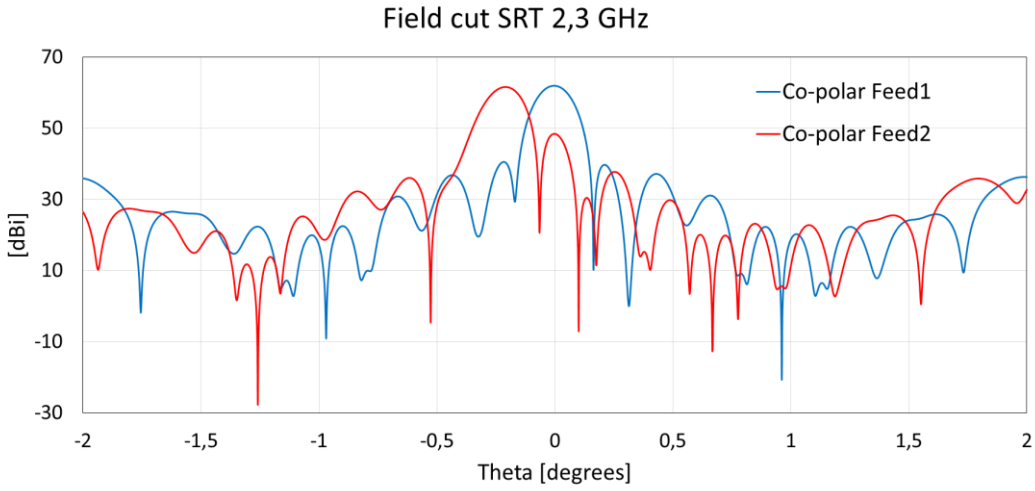

Fig. 4.50: Radiation pattern of the SRT with the feed1 and feed2 of the multifeed system at 2.3 GHz.

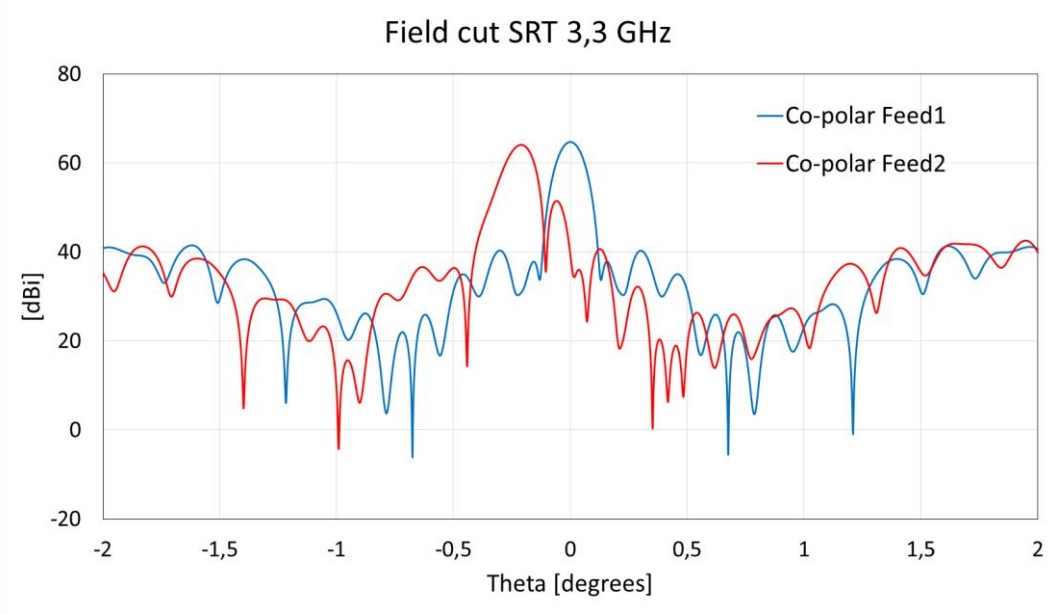

Fig. 4.51: Radiation pattern of the SRT with the feed1 and feed2 of the multifeed system at 3.3 GHz.

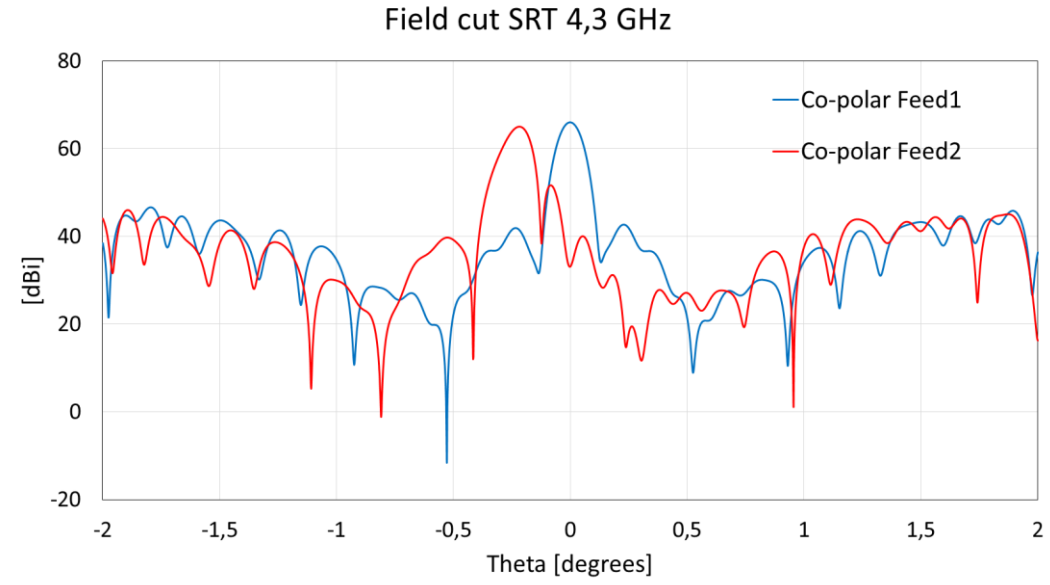

Fig. 4.52: Radiation pattern of the SRT with the feed1 and feed2 of the multifeed system at 4.3 GHz.

To complete the research activity, the realization of a prototype of the proposed feed and tests in the laboratory are foreseen. Unfortunately, this part of research activity was blocked because of the results of a new RFI measurement campaign around SRT site. In fact, at the beginning of 2015, the RFI (Radio Frequency Interference) measurement campaign around SRT site highlighted the presence of pulsed emissions very strong coming from radar systems (the higher power level about -13dBm at 2750 ± 50 MHz). In Fig. 4.53 is shown the maximum signal spectral power density level expected at the input of the feed. The spectrum depicts the signals acquired during a 360-degree scan in azimuth around a

geographic place situated almost at the same altitude of the PFP with the following spectrum analyzer settings: a resolution and video bandwidth equal to 1 MHz, sweep time 0.1 s and 3000 measurement points (1 point for 1 MHz).

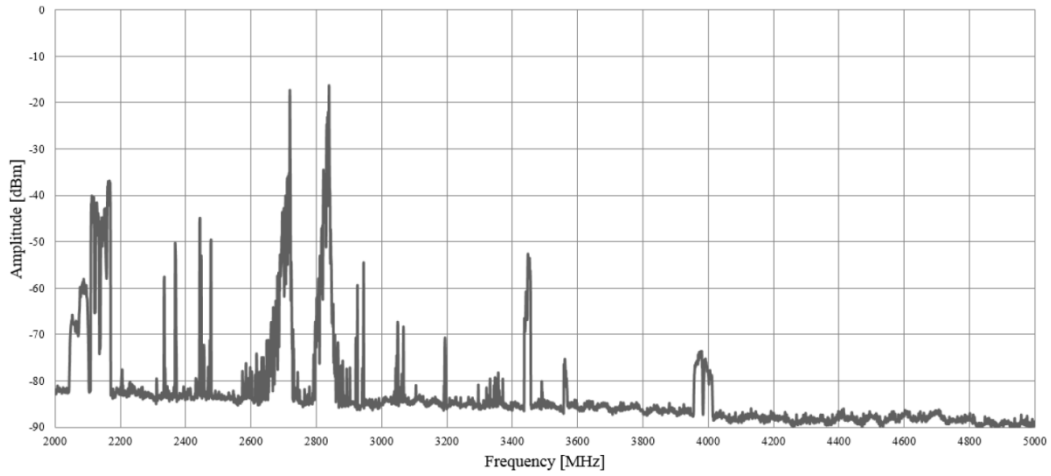

Fig. 4.53: Power spectrum measured by means of the receiving chain of the RFI van around the SRT site [52].

The receiver operation is likely to be seriously compromised because of the presence of strong RFIs in the band between 2.3GHz-3GHz. In order to install this feed on SRT, a quite complex receiving chain would be required to cut off a strong RFI. Therefore, during 2015, a new receiver configuration has been considered for the S-band, in which the horn has been required to provide part of the RFI rejection. Since the latter has a superior effectiveness, a new S-band feed has been designed with a frequency range of only 40% percent bandwidth (3-4.5 GHz).

The new configuration of the feed is presented in the next section.

4.2.2. Design of the new S-band feed configuration.

Since the bandwidth requirements are smaller, the feed specifications are tighter and the performances of this new feed are greatly improved.

The geometry of the new feed is shown in Fig. 4.54. It essentially consists of a circular waveguide horn with four ridges of variable height inside. In the design and optimization of this configuration, we can identify three parts:

- the sidewall profile;
- four ridges with a hyperbolic profile;
- the open-end radiating termination.

Each one of these parts must be accurately designed to comply with the required specifications.

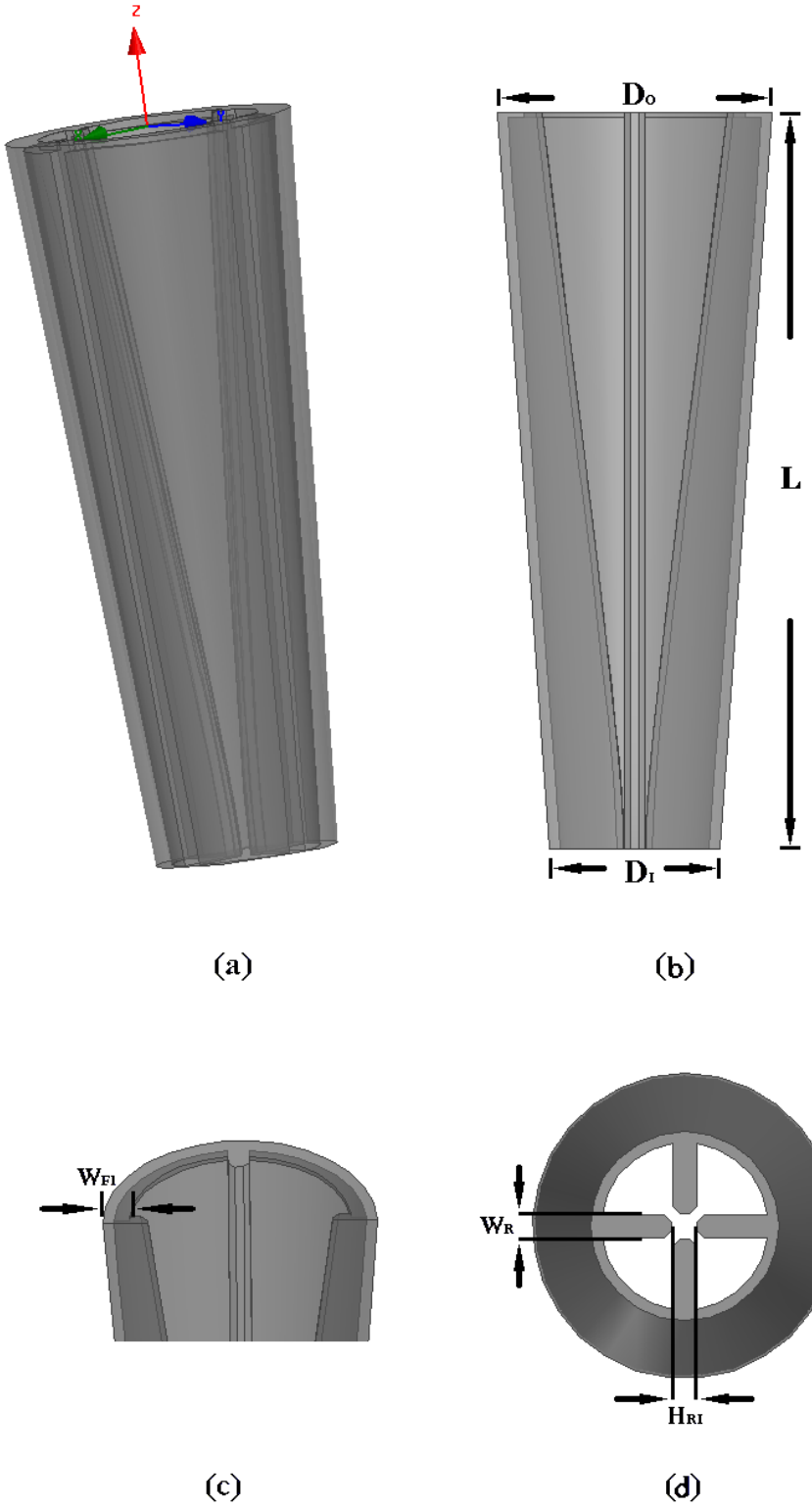

Fig. 4.54: Geometry of the proposed quadruple-ridge horn antenna: (a) 3D view; (b) sectional view; (c) detailed view of radiating aperture; (d) view from the bottom looking up.

The circular waveguide input diameter D_I has been selected equal to 46 mm and output diameter D_O has been selected equal to 78 mm, the initial dimensions of the ridges, H_{RI} and W_R in Fig. 4.54d has been selected equal to, respectively, 7 mm and 6.5mm

The ridge dimensions chosen, together with the waveguide diameter, guarantee that the position of cut-off frequency of the fundamental mode of the ridged circular waveguide is well below the starting frequency of the receiver operating bandwidth, which is equal to 1.45 GHz in our case (Fig. 4.55), and the impedance at the input port of the ridged waveguide is 50 Ω. These values are the same used by the architecture of the circular Ortho Mode Transducer, which is realized using the same quadruple-ridged configuration [52], and connects to the input port of the feed.

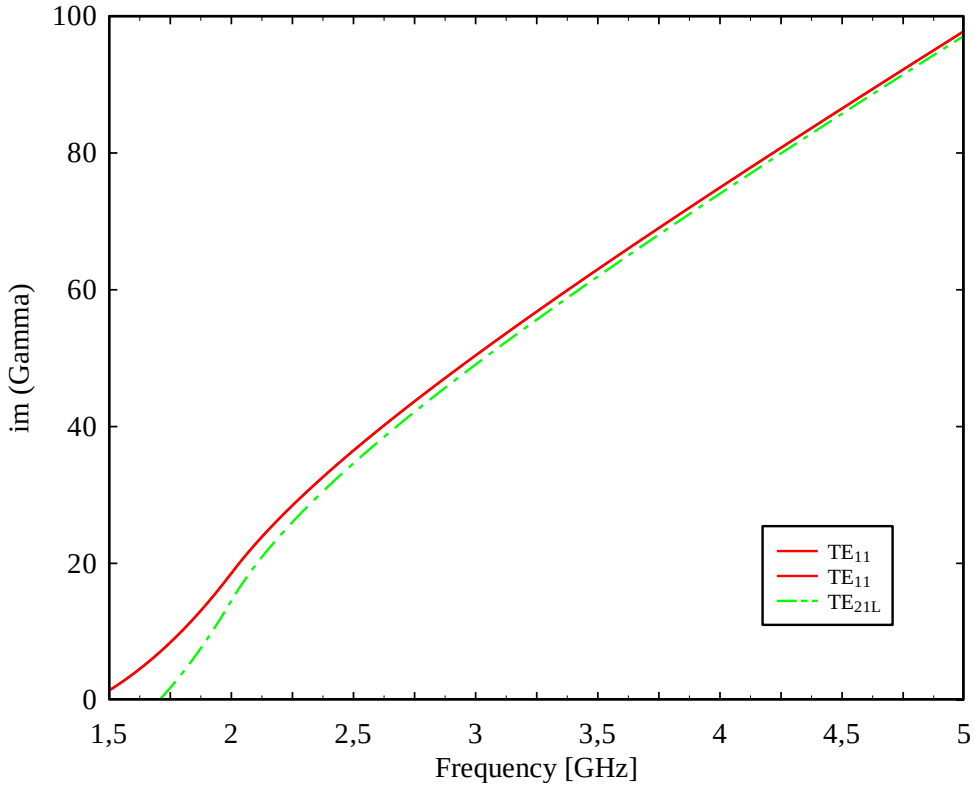

Fig. 4.55: Positions of cut-off frequency of the fundamental mode and first superior modes of proposed feed.

For our application, we have found that the best results are achieved using the hyperbolic profile (see Fig. 4.54), which is described by the following equation:

$$a(z) = \sqrt{a_i^2 + \frac{z^2(a_o^2 - a_i^2)}{L^2}} \qquad [4.8]$$

wherein a_i e a_o are, respectively, the initial height of the ridges (i.e. H_{RI}, at the input port of the feed), and the height of the ridges at the end of the sinusoidal profile (H_{RO} in Fig. 4.54c). L is the length of the ridges along the sinusoidal tapering and, in our case, is equal to 227 mm.

The final stretch of the feed has been optimized for the best input match over the operating bandwidth and for the best radiation pattern. As apparent from the profile of the ridges, a narrowing of the radiating aperture of dimensions W_{F1} and thickness t has been realized.

The optimization procedure on the parameters D_O, W_{F1} and t has been performed using Ansys HFSS. The final values are, respectively, 78mm and 10mm and 2.5 mm.

The simulation performances of the proposed antenna are presented. The new configuration of a quad-ridge horn antenna shows performances in accordance with the project specifications.

The reflection coefficient of the isolated feed is below -20 dB over a 40% bandwidth (Fig. 4.56).

Figs 4.57, 4.58 and 4.59 show the normalized radiation pattern in the ϕ=0°, ϕ=45°, and ϕ=90° planes at the frequencies 3 GHz, 3.75 GHz, and 4.5 GHz. Variations between the patterns can be observed at these frequencies. The radiation patterns of only one polarization are plotted for brevity. However, the performance of the other polarization is virtually the same.

As can be seen from Figure 4.58, the initial request of an edge illumination of -13 dB at 74° at 3.75 GHz was basically met, whereas the edge illumination at 2.3 GHz and 4.3 GHz is, respectively, -10.5 dB and -16.7 dB. The radiation pattern at the central frequency, 3.3 GHz is optimal; the pattern at 2.3 GHz and 4.3 GHz is quite good [52].

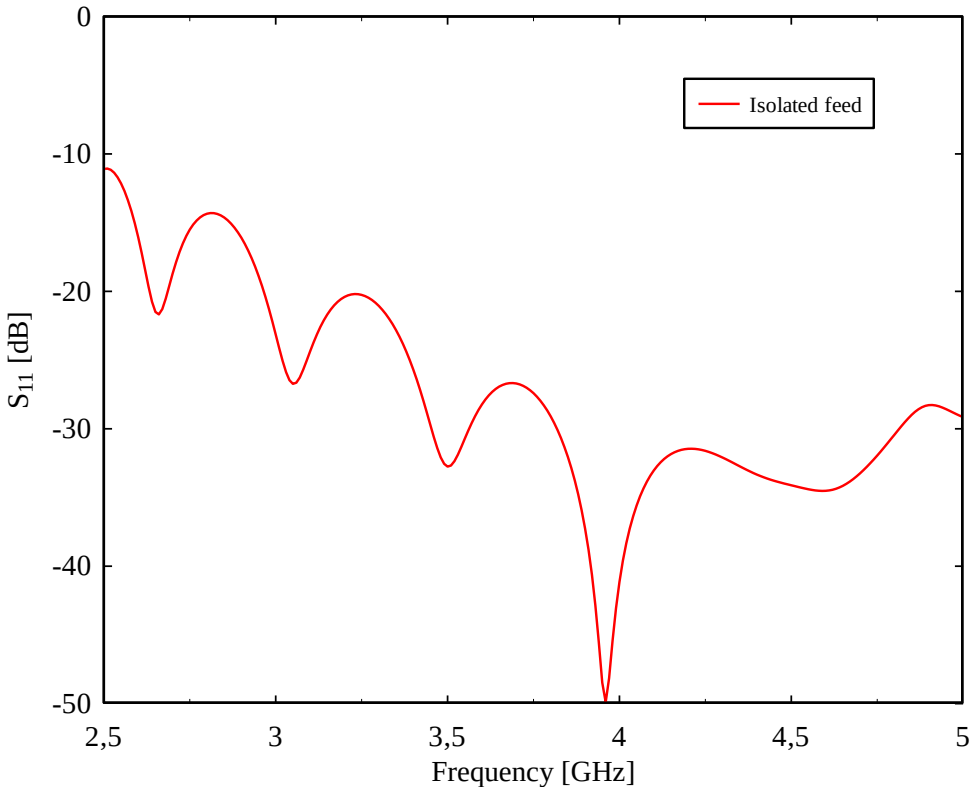

Fig. 4.56: Return loss of the isolated feed.

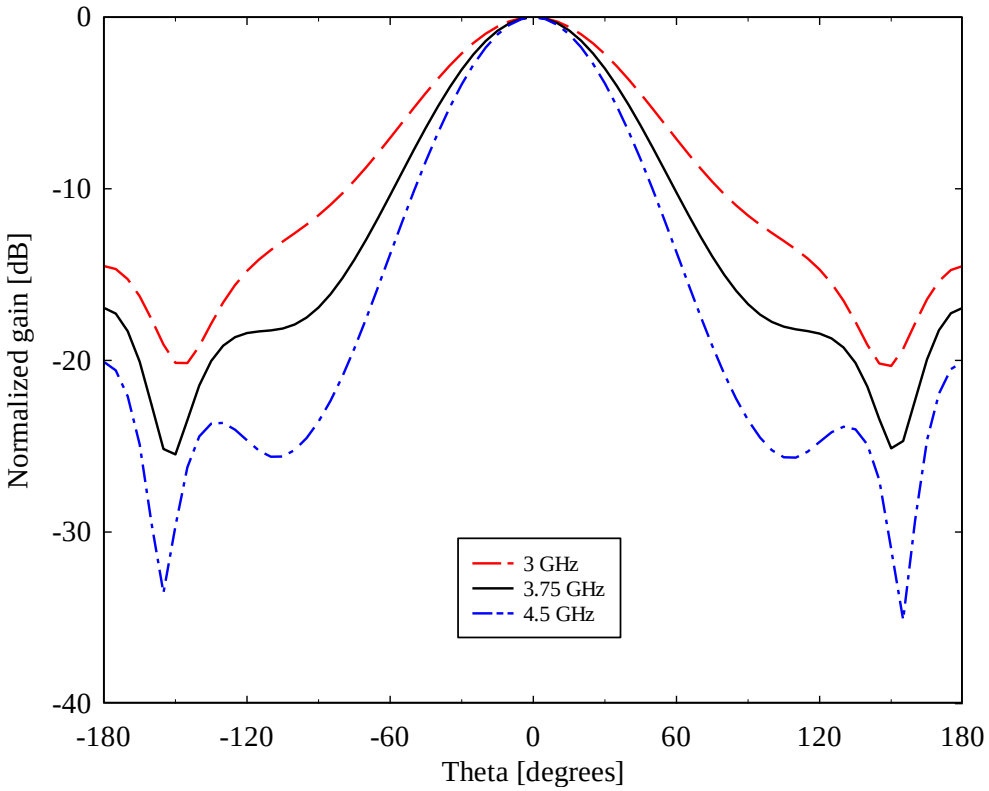

Fig. 4.57: Normalized radiation patterns of the isolated feed at 3 GHz, 3.75GHz and 4.5 GHz in the ϕ = 0° plane.

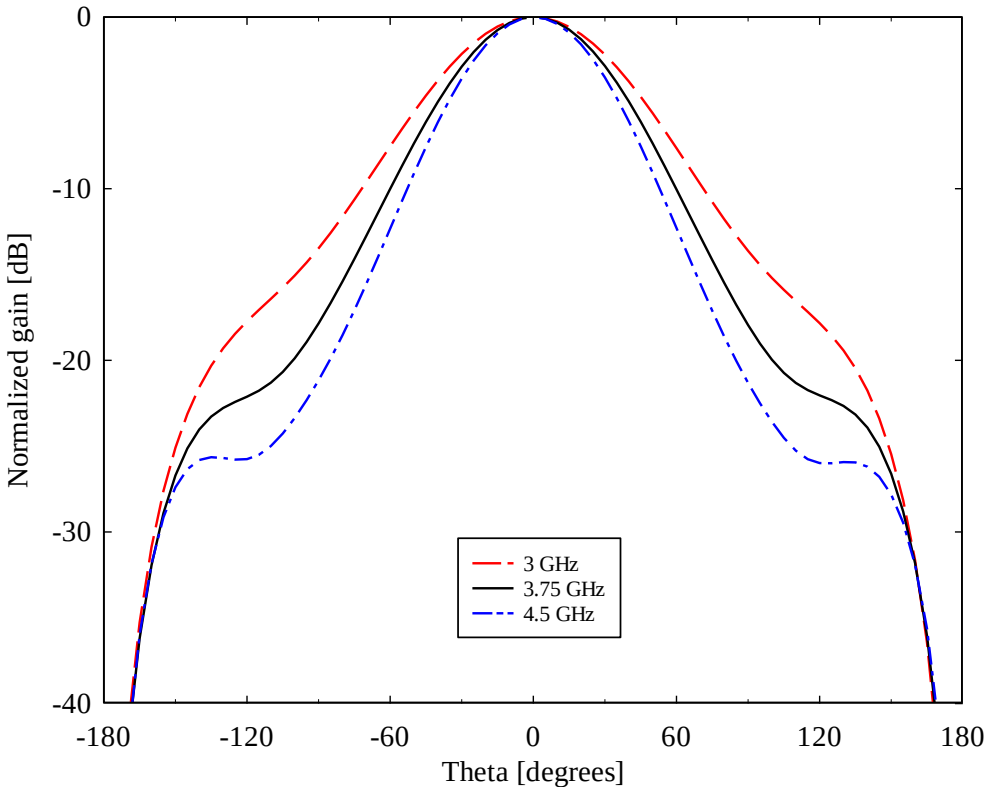

Fig. 4.58: Normalized radiation patterns of the isolated feed at 3 GHz, 3.75GHz and 4.5 GHz in the ϕ = 45° plane.

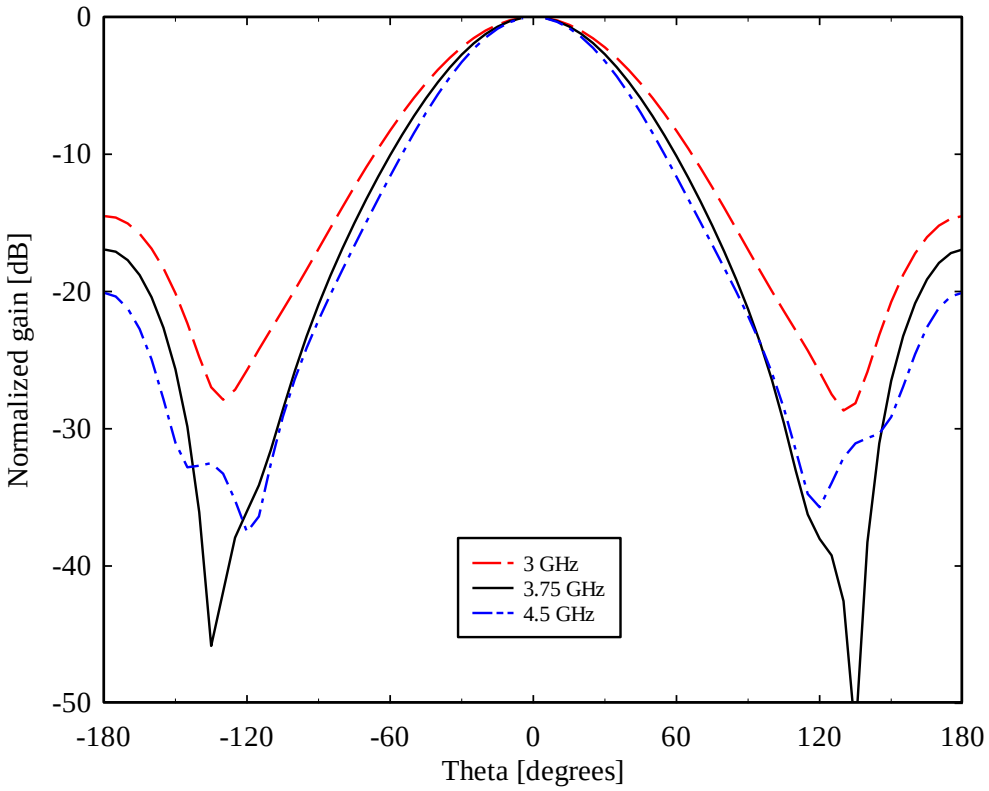

Fig. 4.59: Normalized radiation patterns of the isolated feed at 3 GHz, 3.75GHz and 4.5 GHz in the ϕ = 90° plane.

The design previously described has considered an isolated feed horn, but the real implementation involves an array of seven elements in a hexagonal grid. As explained in the previous section, the choose of the spatial configuration in this hexagonal grid and the number of feeds on a focal plane array (FPA) have been selected to maximize the Field of View of the antenna, keeping in mind the available room in focal cabin of SRT and load limit of the Primary Focus Positioner (PFP) of the Sardinia Radio Telescope. The minimum distance between centers of feeds, which maximize the aperture efficiency of the antenna and produces the better mapping of an extended radio astronomical source, is equal to 100 mm.

The design of the radiating aperture of single feed described above, takes into account the limited space available. Moreover, in order to minimize the mutual coupling effect between the feeds, we decided to fill the space between feeds with an absorbing material (i.e. Eccosorb MF-124). In Figure 4.60 the layout of multifeed is shown.

Fig. 4.60: Final multifeed layout.

Figs. 4.61, 4.62, 4.63, 4.64 and 4.65 show the performances of the Feed1 of this configuration in terms of return loss and radiation pattern.

The reflection coefficient is below -20 dB over a 40% bandwidth. The normalized radiation pattern is show in the ϕ=0°, ϕ=45°, and ϕ=90° planes at the frequencies 3 GHz, 3.75 GHz, and 4.5 GHz.

In order to evaluate the mutual coupling effect between the feeds in the multifeed configuration, we show the comparison between the simulated performances of the central feed when included in the multifeed array and the simulated performances of the isolated feed.

The reflection coefficient remains below -20 dB, the isolation between the Feed1 and the Feed2 is below -28dB and the radiation pattern complies the feed design specifications. Small variations between the pattern of multifeed configuration e isolated feed can be observed, especially in the ϕ=0° plane.

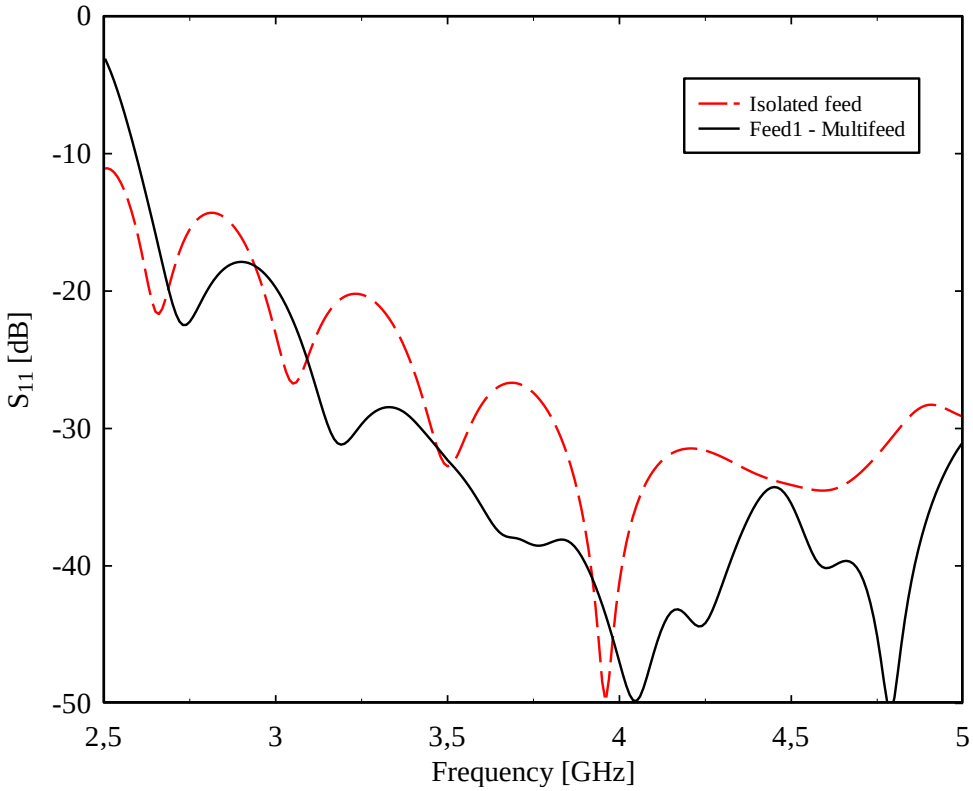

Fig. 4.61: Simulated reflection coefficient of the isolated feed and of the central element of the multifeed configuration.

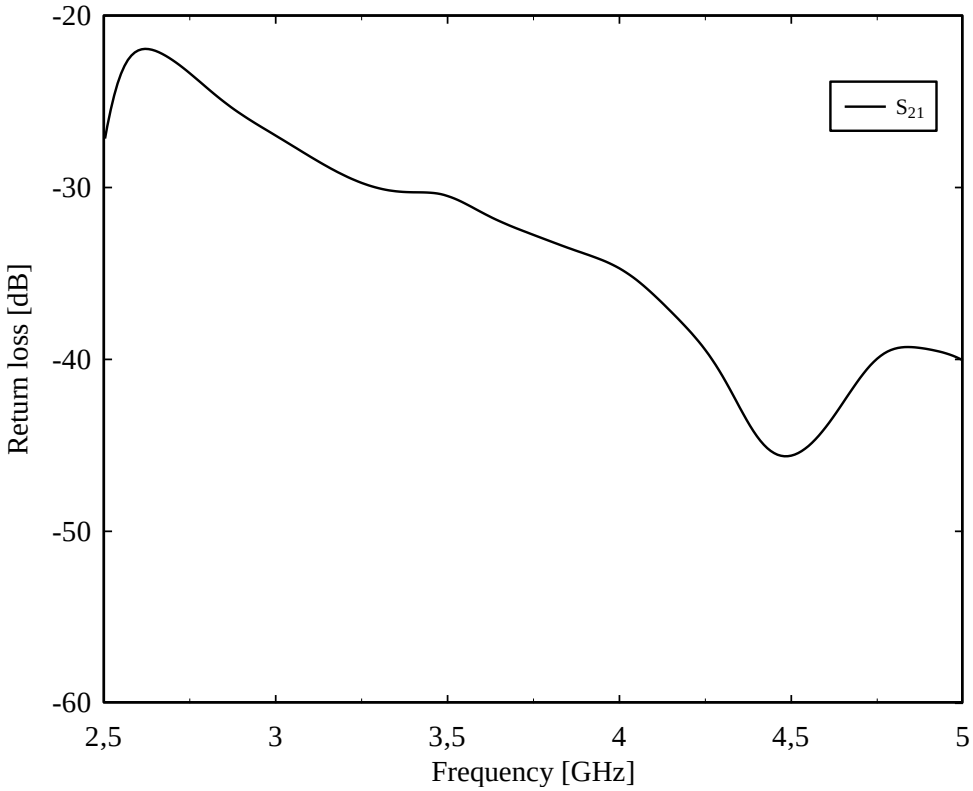

Fig. 4.62: Isolation between Feed1 and Feed2 of the multifeed configuration with seven feeds.

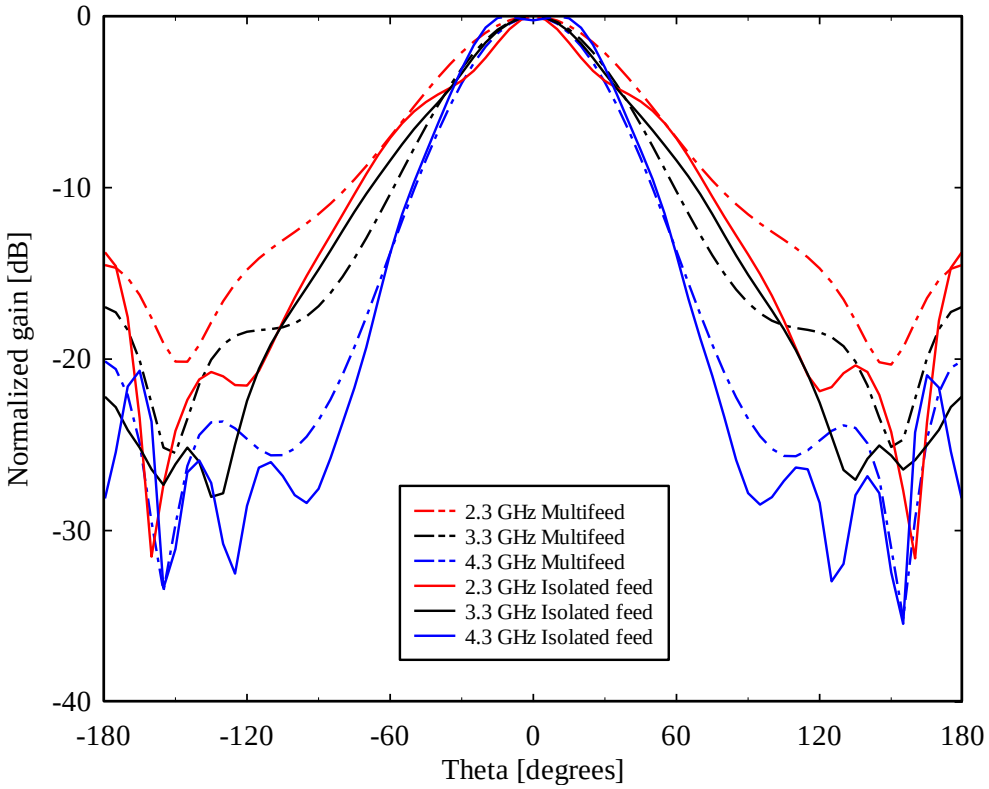

Fig. 4.63: Normalized radiation patterns of the feed1 of multibeam configuration and the isolated feed at 3 GHz, 3.75 GHz and 4.5 GHz in the ϕ = 0° plane.

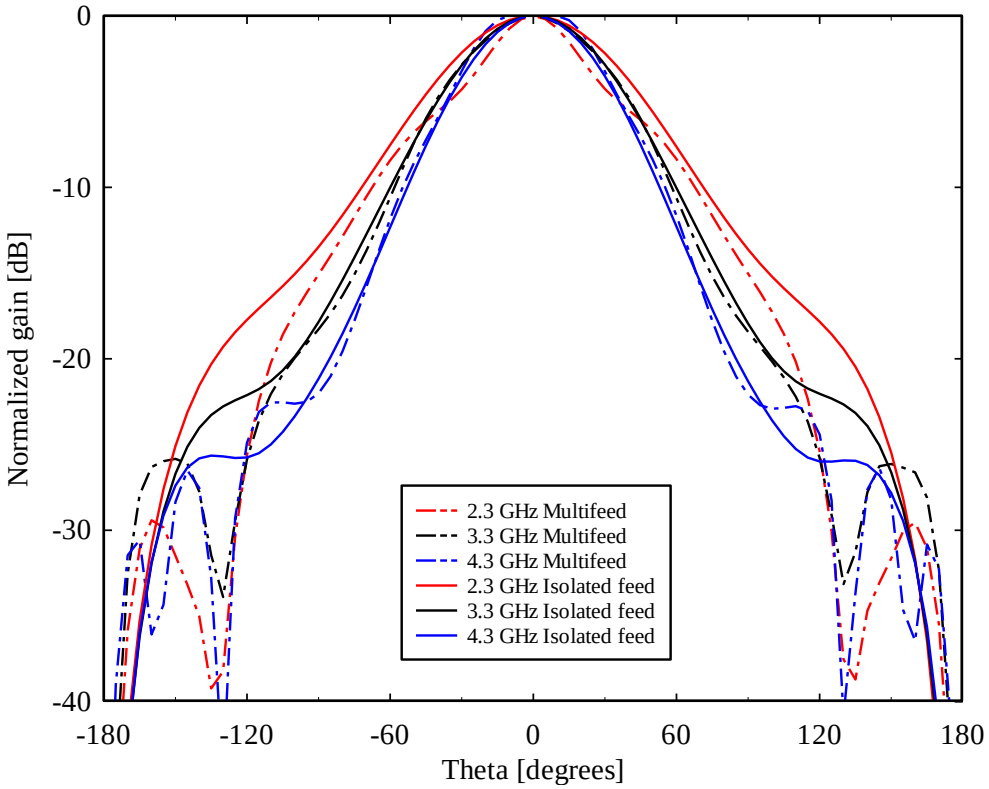

Fig. 4.64: Normalized radiation patterns of the feed1 of multibeam configuration and the isolated feed at 3 GHz, 3.75 GHz and 4.5 GHz in the ϕ = 45° plane.

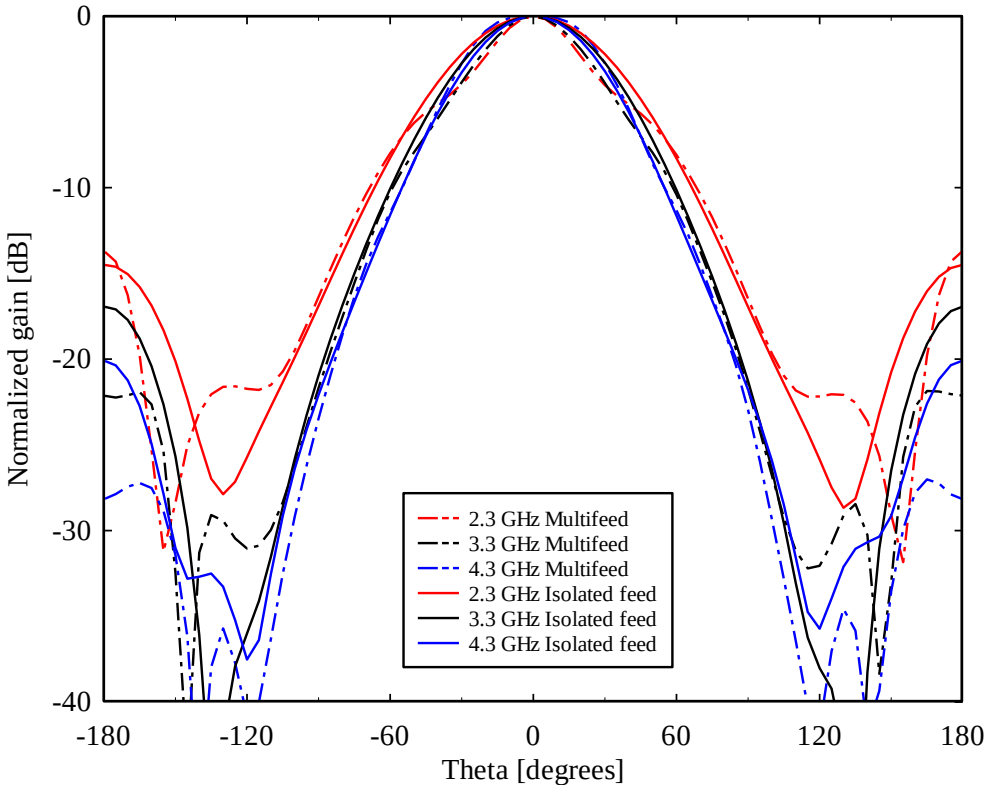

Fig. 4.65: Normalized radiation patterns of the feed1 of multibeam configuration and the isolated feed at 3 GHz, 3.75 GHz and 4.5 GHz in the ϕ = 90° plane.

The electromagnetic coupling between the Sardinia Radio Telescope and the multifeed horn system has been simulated in order to estimate the antenna gain and the cross-polarization component. The complete system has been modeled using the 3D analysis software GRASP 9 by TICRA.

In the GRASP model of SRT we have taken into account the blocking effects of the subreflector, with an 8 m diameter hole centered in the main reflector.

In order to evaluate the mutual coupling effect between the multifeed configuration and SRT, we simulated the electromagnetic behavior of the structure with, respectively, proposed isolated feed and with multibeam configuration.

In Fig 4.66, we show the radiation pattern of the SRT illuminated by the isolated feed, at 3 GHz, at 3.75 GHz, and at 4.5 GHz.

The antenna gain is between 64 dBi at 3 GHz and 66 dBi at 4.5 GHz. The cross polarization level is very good (below -30 dB) at 3 GHz, 3.75 GHz and 4.5 GHz.

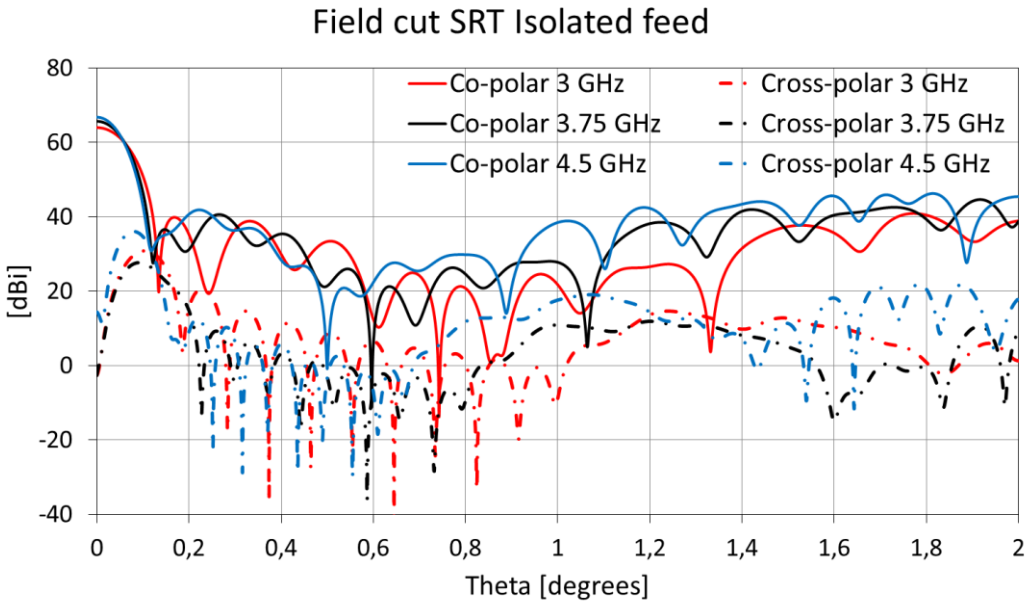

Fig. 4.66: Radiation pattern of the SRT with the isolated feed.

In Fig 4.67, we show the radiation pattern of the SRT illuminated by the central feed of the multifeed array with five feeds, at 3 GHz, at 3.75 GHz, and at 4.5 GHz.

The antenna gain is between 64.3 dBi at 3 GHz and 66.7 dBi at 4.5 GHz. The cross polarization level is very good, it is between 28 dBi at 3 GHz and 30.8 dBi at 4.5 GHz.

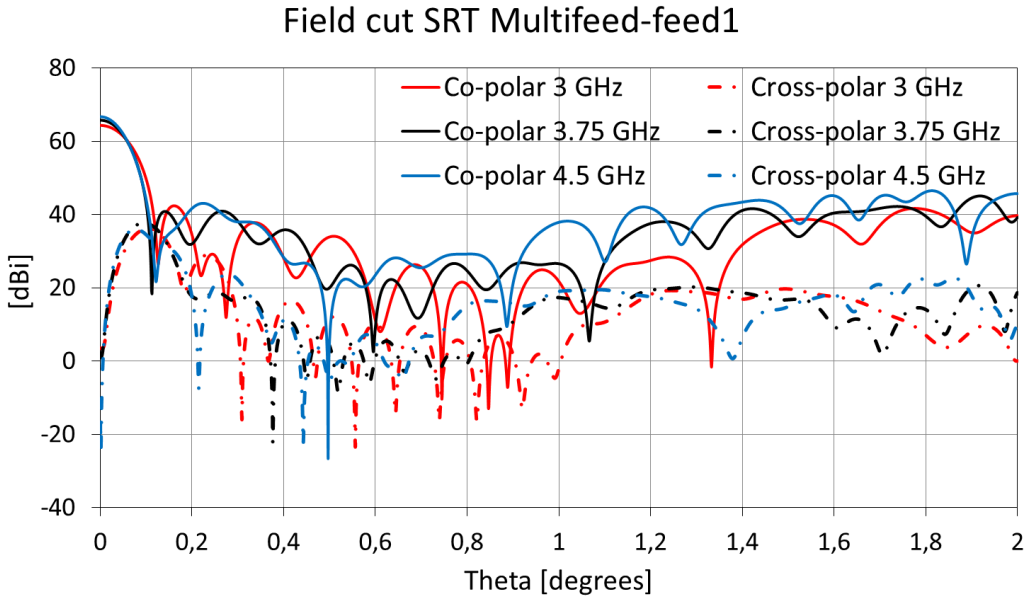

Fig. 4.67: Radiation pattern of the SRT with the multifeed system (7 feeds).

Conclusions

In this PhD thesis, the designs of three different microwave subsystems for radio astronomical receivers have been presented.

The first project regards on the design of a new quadrature branch-line hybrid with broadband performances and very flat phase-response. The design, operating in X-Ku band, is based on the transposition in microstrip technology of a combination of waveguide components used to build broadband polarizers.

The second project regards on the study of optical and mechanical configuration chosen to install a 3 mm SIS receiver in the Gregorian focus of the Sardinia Radio Telescope. Since the IRAM receiver was originally designed for the PdBI antenna, a new optical and mechanical configuration had to be studied to adapt the instruments to the SRT optics and to its cabin mechanical structure.

The third project regards on the design of a new wideband quadruple-ridged horn antenna for a new multifeed S-band receiver of the Sardinia Radio Telescope. The project consists of the design of two different configurations at the state-of-the-art of the waveguide feed horn. The design and optimization of the waveguide feed horn have been performed using the FEM commercial software Ansys HFSS. The developed feeds provide a S_{11} < -20 dB in the operating bandwidth and a good performance in terms of radiation pattern.

Nevertheless, the performances of the second configuration are greatly better than those in the first configuration. The tightened specifications due to the new bandwidth requirements, have allowed us to design a feed horn whose the specifications are in very good accordance with the project specifications required.

References

1. D. F. Miller, "*Basics of Radio Astronomy for the for the Goldstone-Apple Valley Radio Telescope*" April 1998;
2. K. Rohlfs and T. L. Wilson, *"Tools of Radio Astronomy"*, 4th ed., Springer 2004;
3. A. Akgiray: "*New Technologies Driving Decade-Bandwidth Radio Astronomy: Quad-Ridged Flared Horn & Compound-Semiconductor LNAs*" PhD thesis April 2013;
4. www.srt.inaf.it
5. E. Cenacchi, "*SRT Project Book*", Maggio 2007;
6. G. Valente, et al., "*The dual-band L-P feed system for the Sardinia Radio Telescope prime focus*", Proc. SPIEMillimeter, Submillimeter, and Far-Infrared Detectors and Instrumentation for Astronomy V, 7741, 2010;
7. A. Orfei, et al., "*A Multifeed Receiver in the 18-26. 5 GHz Band for Radio astronomy*", IEEE Ant. Prop. Magazine, 52(4), 62, 2010;
8. J. D. Kraus, "*Radio Astronomy*", McGraw Hill book company,October, 1966;
9. A. G. Fox, "*An Adjustable Wave-Guide Phase Changer*", Proc. IRE, vol.35, pp. 1489-1498, Dec. 1947;
10. N.B. Sultan, "*Generalized Theory of Waveguide Differential Phase Sections and Application to Novel Ferrite Devices*", IEEE Trans. MTT., vol. MTT-19, no. 4, pp. 348-357, Apr. 1971;
11. G. Pisano et al., "*A 90 GHz waveguide variable phase-shifter*", IEEE Microw. Wire. Comp. Lett., vol. 17, no.3, pp. 208-210, 2007;
12. G. Pisano et al., "*A Novel Broadband Q-band Polarizer with Very Flat Phase Response*", Journal of Electromagnetic Waves and Applications, v.26, n.5/6, pp 707-715, 2012;
13. A. I. Harris et al., "*Design Considerations for Correlation Radiometers*", NRAO Green Bank Telescope memo series No.254, 2007;
14. G. R. Fowles, "*Introduction to modern optics*", 2nd ed. New York: Dover Publication, 1989;
15. H. R. Ahn at al., "*Arbitrary Power Division Branch-line Hybrid Terminated by Arbitrary Impedances*", Electron. Lett., vol.35, no.7, 1999;
16. C. L. Hsu, "*Dual-Band Branch-line Coupler with Large Power Division Ratios*", Asia-Pacific Microw. Conf., Singapore, 2009, pp. 2088-2091;
17. C. L. Hsu et al., "*Miniaturized Dual-Band Hybrid Couplers with Arbitrary Power Division Ratios*", IEEE Trans. Microw. Theory Tech., vol. 57, no. 1, 2009;
18. C. Gwon et al., "*A New Branch-line Hybrid Coupler with Arbitrary Power Division Ratio*", Asia-Pacific Microw. Conf., Bangkok, 2007, pp. 1-4;

19. T. W. Lin et al., "*Distributed and Lumped Element Realizations of Wideband Branch-line Hybrids with Arbitrary Power Division*", Asia-Pacific Microw. Conf., Singapore, 2009, pp. 2112-2115;
20. Ansoft High Frequency Structure Simulator: www.ansoft.com;
21. Trackwise, unit 4B Delta Drive, Tewkesbury Business Park, Tewkesbury, Gloucestershire GL20 8HB, UK;
22. D. M. Pozar, "*Microwave engineering*", 2nd ed., John Wiley & Sons Inc. New York, 1998;
23. J. Blondel, M.Carter et al., "*Dual-Channel SIS Receivers for the IRAM Plateau de Bure Interferometer*", International Journal of Infrared and Millimeter Waves, Vol. 17(12), 2133-2144, 1996;
24. M. Carter, "*Optics for the HDV10 Dual Frequency Band Receiver for the Plateau de Bure Interferometer*", IRAM Receiver Technical Memo, n°3, 1994;
25. F. Biraud and G. Daigne, "*Achromatic Doublets for Gaussian Beams*", IEEE *Trans Antennas Propagat*, Vol.39(4), 559-561, 1991;
26. P. Goldsmith, "*Quasioptical Systems: Gaussian Beam Quasioptical Propagation and Applications*", IEEE Press, New York, 1998;
27. P. J. B. Clarricoats and A. D. Olver, "*Corrugated Horns for Microwave Antennas*", London, IEE, 1984;
28. A. D. Olver, P. B. Clarricoats, et al., "*Microwave Horns and Feeds*", London, lEE, 1994, Chapter 9;
29. C. Granet and G. L. James, "*Design of Corrugated Horns: A Primer*", IEEE Antennas and Propagation Magazine, 47, April 2005, pp. 76-84;
30. M. Abbas-Azimi, F. Mazlumi, and F. Behnia "*Design of Broadband Constant-Beamwidth Conical Corrugated-Horn Antennas*" IEEE Antennas and Prop. Magazine, Vol. 51, No.5, October 2009;
31. A. D. Olver, "*Corrugated Horns*", Journal of Electronics and Communication Engineering, 4, February 1992, pp. 4-10;
32. B. M. Thomas, "*Design of Corrugated Conical Horns*", IEEE Transactions on Antennas and Propagation, AP-26, March 1978, pp.367-372;
33. Y. Beniguel, A. Berthon, et al., "*Design Realization and Measurement of a High Performance Wide-Band Corrugated Horn*", IEEE Transactions on Antennas and Propagation, AP-53, November 2005, pp. 3540-3546;
34. S. B. Cohn, "*Properties of ridged wave guide*", Proceedings of the IRE, vol. 35, Aug. 1947;
35. S. Hopfer, "*The design of ridged waveguides*", IRE Trans. Microw. Theory Tech., vol. 3, Oct.1955;
36. K. L. Walton, V. C. Sundberg, "*Broadband ridged horn design*", Microwave Journal, 1964, pp. 96-101;
37. J. P. Montgomery, "*On the complete eigenvalue solution of ridged waveguide*", IEEE Trans. Microw. Theory Tech., vol. MTT-19, Jun. 1971;

38. M. H. Chen, G. N. Tsandoulas, F. G. Willwerth, "*Modal characteristics of quadruple-ridged circular and square waveguides*", IEEE Trans. Microw. Theory Tech., 1974, 22, (8), pp. 801–804;

39. W. Sun and C. A. Balanis, "*MFIE analysis and design of ridged waveguides*", IEEE Trans.Microw. Theory Tech., vol. 41, pp. 1965-1971, Nov. 1993;

40. W. Sun and C. A. Balanis, "*Analysis and design of quadruple-ridged waveguides*", IEEE Trans. Microw. Theory Tech., 1994, 42, (12), pp. 2201-2207;

41. C. Granet, "*Profile options for feed horn design*", Proceedings of the Asia-Pacific Microwave Conference. Sydney, Australia, December 2000, pp. 1448-1451;

42. A. Akgiray, W. A. Imbriale, C. Beaudoin, "*Circular Quadruple-Ridged Flared Horn Achieving Near-Constant Beamwidth over Multioctave Bandwidth: Design and Measurements*", IEEE Trans. Antennas Propag., 2013, 61, (3), pp. 1099-1108;

43. O. B. Jacobs, J.W. Odendaal and J. Joubert, "*Quad Ridge Horn Antenna with Elliptically Shaped Sidewalls*", IEEE Trans. Antennas Propag., 2013, 61, (6), pp. 2948-2955;

44. A. Dunning, M. Bowen et al., "*An Ultra-Wideband Dielectrically Loaded Quad-Ridged Feed Horn for Radio Astronomy*", Proceedings of the IEEE-APS Topical Conference on Antennas and Propagation in Wireless Communications. Turin, September 2015, pp. 787-79;

45. A. Giacomini et al., "*Quad-ridge Dual Polarized Antenna for Use in the 2-32GHz Band*", Proceedings of the 6th European Conference on Antennas and Propagation (EUCAP). Prague, March 2012, pp. 769-772;

46. Z. Wenliang et al., "*Quad-ridge Dual Polarized Horn Antenna Design and Optimization*", Proceedings of the 3rd Asia-Pacific Conference on Antennas and Propagation, Harbin, July 2014, pp. 643-646;

47. R. Dehdasht-Heydari, H. R. Hassani, and A. R. Mallahzadeh, "*A New 2–18 GHz Quad-ridged Horn Antenna*", Progress In Electromagnetics Research, PIER 81, 183–195, 2008;

48. P.H. van der Merwe, J.W. Odendaal and J. Joubert "*A wide bandwidth compact quad-ridged horn antenna*", Antenna Technology and Applied Electromagnetics (ANTEM), 15th International Symposium on, June 2012;

49. A. Melis, R. Concu, A. Trois: "*An alternative method for accelerating integration of digital backends in the control software of Italian radio telescopes*", Technical Report of Astronomical Observatory of Cagliari, n. 44, 2014;

50. A. Melis, R. Concu, et al.: "*Perspectives for the Sardinia Radio Telescope as a SETI facility*", Technical Report of Astronomical Observatory of Cagliari, n. 50, 2015;

51. P.Bolli et al.: "*Sardinia Radio Telescope: General description, Technical commissioning and First light*" J. Astron. Instrum. 04, January 2016;
52. G. Valente, G. Serra, F. Gaudiomonte, A. Ladu et al., "*A MultiFeed S-Band Cryogenic Receiver for the Sardinia Radio Telescope Primary Focus*", Proceedings of SPIE, Millimeter, Submillimeter, and Far-Infrared Detectors and Instrumentation for Astronomy VII, Vol. 9153, 2014;
53. P. Focardi, "*Large/complex antenna performance validation for spaceborne radar/radiometeric instruments*", Proceedings of the IEEE Antennas and Propagation Society International Symposium. Orlando, FL, July 2013, pp. 2175- 2176;
54. http://www.arscryo.com/index.html

List of figures

List of tables

List of publications related to the thesis

Journal articles

Adelaide Ladu and Giampaolo Pisanu, "*A new broadband microstrip quadrature hybrid with very flat phase response*", Progress In Electromagnetics Research C, Vol.34, 227-237, 2013.

Adelaide Ladu, Giuseppe Valente, Giorgio Montisci and Giuseppe Mazzarella, "*A wideband quadruple-ridged horn antenna for the multifeed S-band receiver of the Sardinia Radio Telescope* ", Submitted to Journal of Electromagnetic Waves and Applications, Manuscript ID TEWA-2016-0073.

Proceedings of international conferences

G. Valente, G. Serra, F. Gaudiomonte, A. Ladu, T. Pisanu, P. Marongiu, A. Corongiu, A. Melis, M. Buttu, D. Perrodin, G. Montisci, G. Mazzarella, E. Egron, N. Iacolina, C. Tiburzi, V. Vacca: "*A MultiFeed S-Band Cryogenic Receiver for the Sardinia Radio Telescope Primary Focus*", Proc. SPIE Millimeter, Submillimeter, and Far-Infrared Detectors and Instrumentation for Astronomy VII, Vol.9153, 91530Q,2014.

A. Ladu, P. Ortu, A. Saba, P. Marongiu, G. Valente, E. Urru, T. Pisanu, A. Navarrini, G.Mazzarella: "*The control system and the new cryogenics of the 3 mm band SIS receiver for the Sardinia Radio Telescope*", Submitted and accepted to Proc. SPIE Millimeter, Submillimeter, and Far-Infrared Detectors and Instrumentation for Astronomy VIII, Paper no. 9914-75.

G.Valente, A.Ladu et al.," *The 7 Beams S-Band Cryogenic Receiver for the Sardinia Radio Telescope: Status of Project*", Submitted and accepted to Proc. SPIE Millimeter, Submillimeter, and Far-Infrared Detectors and Instrumentation for Astronomy VIII, Paper no. 9914-74.